Methods to Improve Bone Marrow Dosimetry in Molecular Radiotherapy

Methoden zur Verbesserung der Knochenmarkdosimetrie in der molekularen Strahlentherapie

Doctoral thesis for a doctoral degree
at the Graduate School of Life Sciences,
Julius-Maximilians-Universität Würzburg,
Section Biomedicine

submitted by

Maikol Salas Ramírez

from

Quesada, Alajuela, Costa Rica

Würzburg, 2020

CC BY SA

Members of the Promotionskomitee

Chairperson:

Primary Supervisor: Prof. Dr. Michael Laßmann

Supervisor (Second): Prof. Dr. Gerhard Glatting

Supervisor (Third): Prof. Dr. Andreas Buck

Date of Public Defence: …….……

Date of Receipt of Certificates: ……..

Submitted on: ……..……..

Office stamp

Table of Contents

List of Tables vi

List of Figures vii

Abbreviations viii

Summary 1

Zusammenfassung 3

Chapter I Introduction 6

Chapter II Background 8

1. Bone Structure 8
   - 1.1. Bone Marrow Structure and Function 8
   - 1.2. Trabecular Bone 9
2. Quantification of the Fat Volume Fraction in Bone Marrow using Magnetic Resonance Imaging 11
   - 2.1. Basics of Magnetic Resonance Imaging 11
   - 2.2. Magnetic Resonance Parameters 13
   - 2.3. Quantification of the Fat Volume Fraction using Magnetic Resonance Spectroscopy (MRS) 14
   - 2.4. Quantification of the Fat Volume Fraction Using Magnetic Resonance Imaging 17
3. Quantification of the Trabecular Bone Volume Fraction using Dual-Energy Computed Tomography 20
   - 3.1. Basics of Computed Tomography 20
   - 3.2. Dual Energy Quantitative Computed Tomography (DEQCT) 22
4. Bone Marrow Dosimetry for Molecular Radiotherapy 24
   - 4.1. Calculation of the Absorbed Dose in Internal Radiation Dosimetry 24
   - 4.2. Elements of a Radiation Transport Model 26
   - 4.3. Bone and Bone Marrow Radiation Transport Models 28

Chapter III Methods 31

1. Quantification of the Fat Volume Fraction in Lumbar Vertebrae 31
   - 1.1. Validation Phantom 31
   - 1.2. Quantification of the Fat Volume Fraction in the Validation Phantom Using MRS and MRI 32

1.3. Quantification of the Fat Volume Fraction in 3 Healthy Volunteers Using MRS and MRI 33
1.4. Retrospective Quantification of the Fat Volume Fraction in 46 Sequentially Scanned Patients Using MRI 34
2. Quantification of the Bone Volume Fraction 36
2.1. DEQCT Method 36
2.2. Phantom 1: Validation Phantom 40
2.3. Phantom 2: European Spine Phantom 41
2.4. Phantom Acquisition Parameters 42
2.5. Analysis of the Validation Phantom 43
2.6. Analysis of the European Spine Phantom 43
2.7. Analysis of a Patient Dataset 44

Chapter IV Results 47
1. Quantification of the Fat Volume Fraction in Lumbar Vertebrae 47
1.1. Quantification of the Fat Volume Fraction in the Validation Phantom Using MRS and MRI 47
1.2. Quantification of the Fat Volume Fraction in 3 Healthy Volunteers Using MRS and MRI 49
1.3. Retrospective Quantification of the Fat Volume Fraction in 46 Sequentially Scanned Patients Using MRI 50
2. Quantification of the Bone Volume Fraction 52
2.1. Quantification of the Hydroxyapatite Volume Fraction in Samples of the Validation Phantom 52
2.2. Quantification of the Fat, Water, and Hydroxyapatite Volume Fraction in Samples of the Validation Phantom 54
2.3. Quantification of the Bone Mineral Content in the European Spine Phantom Using DEXA, DSCT, and SPECT/CT 54
2.4. Quantification of the Hydroxyapatite Volume Fraction in Spongiosa Regions of the European Spine Phantom 57
2.5. Quantification of the Mineral Bone (Hydroxyapatite) Volume Fraction and the Bone Volume Fraction in a Patient Dataset 59

Chapter V Discussion 61
1. Quantification of the Fat Volume Fraction in the Lumbar Vertebrae 61
1.1. Quantification of the Fat Volume Fraction Using Two-point Dixon MRI 61
1.2. Correlation between Fat Volume Fraction and Age 62
1.3. Implications of the Dependency of the Cellularity Volume Fraction with Age and Gender in the Calculation of the Bone Marrow Absorbed Dose in Molecular Radiotherapies 62
1.4. Study Limitations 64

2. Quantification of the Trabecular Bone Volume Fraction 65
2.1. Quantification of Hydroxyapatite Volume Fraction in Samples of the Validation Phantom 65
2.2. Quantification of Bone Mineral Content in the European Spine Phantom Using DEXA, DSCT, and SPECT/CT 66
2.3. Quantification of Hydroxyapatite Volume Fraction in Spongiosa Regions of the European Spine Phantom 67
2.4. Quantification of the Mineral Bone (Hydroxyapatite) Volume Fraction and the Bone Volume Fraction in a Patient Dataset 68
2.5. Implications of the Quantification of the Bone Volume Fraction in the Calculation of the Bone Marrow Absorbed Dose in Molecular Radiotherapies 70
2.6. Study Limitations 71

Chapter VI Conclusion 73

Appendix 1: Fat Volume Fraction – Additional Tables and Figures.....75

Appendix 2: Bone Volume Fraction – Additional Tables and Figures 78

Appendix 3: Bone Volume Fraction – Calculation of Empirical Correction Factors..80

Bibliography 83

Eidesstattliche Erklärung /Affidavit.....94

Curriculum Vitae.....95

Publications 96

Acknowledgments.....98

List of Tables

Table 1. Phantom acquisition parameters for both CT systems.....42
Table 2. Linear fit parameters for each data pair obtained from the validation phantom using MRS and MRI 47
Table 3. Linear fit parameters of the correlation between age and fat volume fraction for females and males. 51
Table 4. Data from the Bland-Altman Analysis of the Quantification of Hydroxyapatite Volume Fraction in the Validation Phantom. 54
Table 5. Data from Bland-Altman Analysis of the Quantification of Bone Mineral Content (Whole Vertebra) in the European Spine Phantom 55
Table 6. Data from a Bland-Altman Analysis of the Quantification of Hydroxyapatite Volume Fraction in Spongiosa Region of the European Spine Phantom 59
Table 7. Values of Mass and Volume Fractions of HA and Bone in lumbar Vertebrae 1 and 2 from a Patient Image Set. 60
Table 8. Linear Fit Parameters of Retrospective Quantification of the Fat Volume Fraction in 46 Sequentially Scanned Patients Using MRI 75
Table 9. Chemical Element Composition of Calibration Samples. 78
Table 10. $Zeff$ and ρeff values of Validation Phantom and CIRS model 062. 78
Table 11. $Zeff$ and ρeff Values of European Spine Phantom. 79

List of Figures

Figure 1. MRI of the validation phantom. 32
Figure 2. Example of the ROI drawn using Fiji (ImageJ) to define: 34
Figure 3. Axial view of the validation phantom. 41
Figure 4. Views of the European Spine Phantom. 42
Figure 5. Segmentation of lumbar vertebrae 1 and 2 on the DSCT image. 45
Figure 6. Segmentation of spongiosa region in lumbar vertebrae 1 and 2 on DSCT image. 45
Figure 7. Linear data fit of the quantification of the fat volume fraction in the validation phantom. 48
Figure 8. Bland-Altman plots of the quantification of the fat volume fraction in the validation phantom for each data pair. 49
Figure 9. Bland-Altman plots of the quantification of the fat volume fraction in volunteers. 50
Figure 10. Linear data fit of the MRI quantification of the fat volume fraction in patient lumbar vertebrae. 51
Figure 11. Bland-Altman plots of each image-based quantification. 53
Figure 12. Bland-Altman plots of each image-based quantification. 56
Figure 13. Relative errors associated with the quantification of the bone mineral content in the whole vertebrae (without transversal processes) of the European spine phantom. 57
Figure 14. Bland-Altman plots of each image-based quantification: 58
Figure 15. Age-dependency of the fat fraction in lumbar vertebrae in females. 76
Figure 16. Age-dependency of the fat fraction in lumbar vertebrae in males. 77

Abbreviations

BMC	Bone Mineral Content
CIRS	Computerized Imaging Reference Systems
CT	Computed Tomography
DECT	Dual Energy Computed Tomography
DEQCT	Dual Energy Quantitative Computed Tomography
DEXA	Dual-Energy X-ray Absorptiometry
DSCT	Dual Source Computed Tomography
ESP	European Spine Phantom
HA	Hydroxyapatite
HU	Hounsfield Unit
ICRP	International Commission of Radiation Protection
ICRU	International Commission of Radiation Units & Measurements
MF	Mass Fraction
MF_B	Bone Mass Fraction
MF_{HA}	Hydroxyapatite Mass Fraction
MIRD	Committee on Medical Internal Radiation Dose
MR	Magnetic Resonance
MRI	Magnetic Resonance Imaging
MRS	Magnetic Resonance Spectroscopy
ppm	parts per million
ROI	Regions of Interest
SPECT/CT	Single Photon Emission Computed Tomography/CT
VF_B	Bone Volume Fraction
VF_F	Fat Volume Fraction
VF_{HA}	Hydroxyapatite Volume Fraction
VF_{TB}	Trabecular Bone Volume Fraction
VOI	Volume of Interest

Summary

Bone marrow dosimetry is a topic of high interest in molecular radiotherapy. Predicting the level of hematological toxicity is one of the most important goals of nuclear medicine radiation dosimetry. To achieve this, it is necessary to quantify the absorbed dose to the active bone marrow, thus aiming at administering the most efficient therapy with a minimum level of adverse effects in the patient. The anatomical complexity of trabecular bone and bone marrow leads to the need of applying non-nuclear medicine imaging methods for determining the spatial distribution of soft tissue, adipose tissue, and bone in spongiosa.

Therefore, the two objectives of this dissertation are: i) to apply magnetic resonance imaging (MRI) for quantification of the fat volume fraction, and ii) to validate a method based on dual-energy quantitative computed tomography (DEQCT) for quantification of the trabecular bone volume fraction.

In a first step, an MRI sequence (two-point Dixon) for fat-water separation was validated in a 3 Tesla system by quantifying the fat volume fraction in a phantom and the lumbar vertebrae of volunteers and comparing with magnetic resonance spectroscopy (MRS). After successful validation, the fat volume fraction was retrospectively measured in the five lumbar vertebrae of 44 patient images acquired in the clinical routine. The two-point Dixon showed a good quantification of the fat volume fraction in the phantom experiment (-9.8% maximum relative error with respect to the nominal values). In the volunteers, a non-significant difference between MRI and MRS was found for the quantification of the fat volume fraction in volumes-of-interest with similar dimensions and position in both quantification methodologies (MRI and MRS). In the study with patient data, the marrow conversion (red → yellow marrow) was found to be age-dependent, and slower in males (0.3% per year) than in females (0.5% per year). Also, considerable variability of the fat volume fraction in patients of similar ages and the same gender was observed.

These results enable the use of two-point Dixon MRI in the quantification of the fat volume fraction in the bone marrow. Additionally, the constant marrow conversion during adulthood suggests that a patient-specific approach should replace the assumption of a constant cellularity volume fraction of 0.7 (reference man) (*1,2*) as proposed by the International Commission on Radiological Protection (ICRP).

In a second step, a quantification method based on DEQCT was validated in two CT systems: i) a clinical CT integrated into a SPECT/CT and ii) a dual-source computed tomography (DSCT) system. The method was applied in two phantoms: the first was used to

validate the DEQCT method by the quantification of the hydroxyapatite volume fraction in three vials of 50 ml each and three different hydroxyapatite concentrations (100 mg/cm^3, 200 mg/cm^3, 300 mg/cm^3). The second phantom was the European spine phantom (ESP), an anthropomorphic spine phantom. It was used to quantify the bone mineral content (BMC) on the whole vertebra and the hydroxyapatite volume fraction (VF_{HA}) in the spongiosa region of each vertebra of the phantom. Lastly, the BMC of lumbar vertebrae 1 (LV1) and 2 (LV2) was measured in a patient using DEQCT and dual-energy X-ray absorptiometry (DEXA). Furthermore, the hydroxyapatite volume fraction (VF_{HA}) and the bone volume fraction (VF_B) was calculated for both the whole vertebrae and the spongiosa region of LV1 and LV2.

The measured and nominal hydroxyapatite volume fraction in the vial phantom showed a good correlation (maximum relative error: 14.2%). The quantification of the BMC on the whole vertebra and the VF_{HA} on the spongiosa region showed larger relative errors than in the validation phantom. The quantification of BMC on LV1 and LV2 showed relative errors between DEXA and DSCT equal to 7.6% (LV1) and −8.4% (LV2). Also, the values of the VF_{HA} (mineral bone) were smaller than the VF_B. This result is consistent with the bone composition (mineral bone plus organic material).

The DEQCT method enables the quantification of hydroxyapatite (mineral bone) and bone (mineral bone plus organic material) in a clinical setting. However, the method showed an overestimation of the quantified mineral bone volume fraction. This overestimation might be related to the lack of detailed information on the CT X-ray spectra and detector sensitivity. Also, the DEQCT method showed a dependency on the CT reconstruction kernel and the chemical description of the materials to be quantified.

Based on the results of this work, the feasibility for quantifying the fat volume fraction and the bone volume fraction in the spongiosa in a clinical setting has been demonstrated/proven. Furthermore, the differences in fat volume fraction in females and males, as well as the variability of the fat volume fraction in subjects of similar ages, questions the approximation of the cellularity volume fraction by only a single ICRP reference value in bone marrow dosimetry for molecular radiotherapy. Lastly, this study presents the first approach for non-invasive quantification of the bone volume fraction (mineral bone plus organic material) for improved bone marrow dosimetry.

Zusammenfassung

Die Knochenmarkdosimetrie ist von großem Interesse für die Radionuklidtherapie. Die Vorhersage des Grades der hämatologischen Toxizität ist eines der wichtigsten Ziele der nuklearmedizinischen Dosimetrie. Um dieses Ziel zu erreichen, ist es erforderlich, die Energiedosis des aktiven Knochenmarks zu quantifizieren, um dem Patienten so eine möglichst effiziente Therapie mit einem minimalen Maß an unerwünschten Nebenwirkungen verabreichen zu können. Die anatomische Komplexität von Knochentrabekel und Knochenmark macht es erforderlich, nicht-nuklearmedizinische bildgebende Verfahren anzuwenden, um die räumliche Verteilung von Weichgewebe, Fettgewebe und Knochen in der Spongiosa zu bestimmen.

Daher sind die zwei Ziele dieser Dissertation: i) die Anwendung der Magnetresonanztomographie (MRT) zur Quantifizierung des Fettvolumenanteils und ii) die Validierung einer auf der quantitativen Dual-Energy Computertomographie (engl. Dual-energy quantitative computed tomography, DEQCT) basierenden Methode zur Quantifizierung des Knochentrabekelvolumenanteils.

In einem ersten Schritt wurde eine Zweipunkt-Dixon-Sequenz der MRT zur Fett-Wasser-Trennung in einem 3 Tesla-System validiert, indem der Fettvolumenanteil in einem Phantom und in den Lendenwirbeln von Probanden quantifiziert und mit mittels der Magnetresonanzspektroskopie (MRS) ermittelten Werten verglichen wurde. Nach erfolgreicher Validierung wurde der Fettvolumenanteil retrospektiv an den fünf Lendenwirbeln von 44 in der im klinischen Routine aufgenommenen Patientendatensätzen gemessen. Die Zweipunkt-Dixon-Methode zeigte eine gute Quantifizierung des Fettvolumenanteils im Phantomexperiment (−9,8% maximaler relativer Fehler in Bezug auf die Nennwerte). Bei den Probanden wurde ein nicht signifikanter Unterschied zwischen MRT und MRS für die Quantifizierung des Fettvolumenanteils in einem Zielvolumen mit ähnlichen Dimensionen und ähnlicher Orientierung festgestellt. In der Patientenstudie wurde festgestellt, dass die Umwandlung des Knochenmarks (rotes Knochenmark → gelbes Knochenmark) altersabhängig und bei Männern (0,3% pro Jahr) langsamer als bei Frauen (0,5% pro Jahr) voranschreitet. Es wurde allerdings auch eine beträchtliche Variabilität des Fettvolumenanteils bei Patienten ähnlichen Alters und gleichen Geschlechts beobachtet.

Diese Ergebnisse ermöglichen die Verwendung der Zweipunkt-Dixon-MRT zur Quantifizierung des Fettvolumenanteils im Knochenmark. Darüber hinaus legt die konstante Umwandlung des Knochenmarks im Erwachsenenalter nahe, dass der von der Internationalen Strahlenschutzkommission (engl. International Commission on Radiological Protection, ICRP)

vorgeschlagene konstante Zellvolumenanteil von 0,7 (Referenzwert für einen männlichen Erwachsenen) (*1,2*) durch einen patientenspezifischen Ansatz ersetzt werden sollte.
In einem zweiten Schritt wurde eine auf DEQCT basierende Quantifizierungsmethode in zwei CT-Systemen validiert: i) ein in ein SPECT/CT integriertes klinisches CT und ii) ein Dual-Source-Computertomographie-System (DSCT). Die Methode wurde an zwei Phantomen erprobt: Das erste diente zur Validierung der DEQCT-Methode, wobei der Hydroxylapatit-Volumenanteil in drei 50-Milliter-Phiolen mit drei verschiedenen Hydroxylapatit-Konzentrationen (100 mg/cm^3, 200 mg/cm^3, 300 mg/cm^3) quantifiziert wurde. Das zweite Phantom war das European Spine Phantom (ESP), ein anthropomorphes Wirbelsäulenphantom. Es wurde verwendet, um den Knochenmineralgehalt (engl. Bone Mineral Content, BMC) des gesamten Wirbels und den Hydroxylapatit-Volumenanteil (VF_{HA}) in der Spongiosa-Region jedes Phantomwirbels zu quantifizieren. Schließlich wurde der BMC der Lendenwirbel 1 (LV_1) und 2 (LV_2) bei einem Patienten unter Verwendung von DEQCT und Dual-Röntgen-Absorptiometrie (engl. dual-energy X-ray absorptiometry, DEXA) gemessen. Darüber hinaus wurden der Hydroxylapatit-Volumenanteil (VF_{HA}) und der Knochenvolumenanteil (V_{FB}) sowohl für die gesamten Wirbel als auch für die Spongiosa-Region von LV_1 und LV_2 berechnet.

Der gemessene und der nominelle Hydroxylapatit-Volumenanteil in den Phiolen zeigten eine gute Korrelation (maximaler relativer Fehler: 14,2%). Die Quantifizierung des BMC im gesamten Wirbel und des VF_{HA} in der Spongiosa-Region zeigten größere relative Fehler als im Validierungsphantom: Die BMC-Quantifizierung für LV_1 und LV_2 ergaben relative Fehler zwischen DEXA und DSCT in Höhe von 7,6% (LV_1) und −8,4% (LV_2). Auch die Werte des VF_{HA} (mineralischer Knochen) waren kleiner als die des VF_B. Dieses Ergebnis steht im Einklang mit der Knochenzusammensetzung (Knochenmineral plus organisches Material).
Die DEQCT-Methode ermöglicht die Quantifizierung von Hydroxylapatit (mineralischer Knochen) und Knochen (mineralischer Knochen plus organisches Material) in einem klinischen Umfeld. Die Methode zeigte jedoch eine Überschätzung des quantifizierten mineralischen Knochenvolumenanteils. Diese Überschätzung könnte mit dem Mangel an detaillierten Informationen über die CT-Röntgenspektren und die Detektorempfindlichkeit zusammenhängen. Auch die DEQCT-Methode zeigte eine Abhängigkeit vom verwendeten CT-Rekonstruktionsalgorithmus und der chemischen Beschreibung der zu quantifizierenden Materialien.

Die Ergebnisse dieser Dissertation zeigen die Machbarkeit einer Quantifizierung des Fettvolumenteils und des Knochenvolumenteils in der Spongiosa in einem klinischen Kontext. Darüber hinaus geben die Unterschiede im Fettvolumenanteil von Frauen und Männern sowie die Variabilität des Fettvolumenanteils bei Individuen ähnlichen Alters Grund zur kritischen Auseinandersetzung mit der Näherung des Zellvolumenanteils durch nur einen einzelnen

ICRP-Referenzwert in der Knochenmarkdosimetrie bei Radionuklidtherapien. Zusätzlich wird in dieser Arbeit der erste Ansatz für eine nicht-invasive Quantifizierung des Volumenanteils des Knochens (Knochenmineral plus organisches Material) für eine verbesserte Dosimetrie des Knochenmarks vorgestellt.

Chapter I
Introduction

Molecular radiotherapy is the treatment of oncological diseases, such as neuroendocrine tumors, thyroid cancer, bone pain palliation, and others, administrating a radionuclide or a pharmaceutical labeled with a radionuclide. The use of ionizing radiation for treatment is linked to a treatment planning procedure that permits to optimize the activity to be administered to the patient.

Treatment planning for molecular radiotherapy is based on the calculation of absorbed doses to target and risk organs or tissues, and tumor(s) (*3*). The absorbed dose $D(r_T)$ is defined "as the energy imparted to a target tissue (or region) r_T per unit tissue mass" (*4*). Therefore, the treatment planning is carried out to administer to the patient a safe amount of radioactivity, and at the same time, achieve the best possible tumor volume control (*3,5*).

Bone marrow, specifically, is considered an organ-at-risk and dose-limiting tissue in many molecular radiotherapy procedures (*6,7*). Bone marrow is a highly cellular tissue located inside bone cavities, and it is spread throughout the skeleton (*1,2*). Furthermore, it is a complex tissue composed of active marrow and inactive marrow. Active marrow is haematopoietically active and produces all the blood cells (*1,2*). Therefore it is the most radiosensitive tissue in the body (*6*). Inactive marrow is mainly composed of fat cells, and it is haematopoietically inactive (*1,2*). Furthermore, the inner part of the bones is occupied by the bone marrow and the trabecular bone. The trabecular bone is a bone latticework, and it is located at the interior of flat bones and the ends of long bones (*1,2*).

The complex spatial distribution of each tissue (active marrow, inactive marrow, and trabecular bone) represents an important challenge for carrying out bone marrow dosimetry. The dependency between the spatial distribution of each tissue and the absorbed dose to each tissue is defined by the distribution of the radionuclide (or a radiolabeled pharmaceutical) and the absorbed dose rate per unit radioactivity (or S value). Therefore, the main goal for determining the spatial distribution of the trabecular bone and bone marrow is to use patient-specific S values for bone marrow dosimetry.

The spatial distribution of the trabecular bone and bone marrow can be determined by the quantification of macroscopic parameters such as the volume fractions of active marrow, inactive marrow, and trabecular bone. The volume fraction of each tissue undergoes continuous changes throughout life (*1,2*) and is gender dependent (*8,9*). Therefore, the use of reference values for treatment planning could lead to important errors in the calculation of the absorbed dose to the bone marrow. For a clinically achievable assessment, the definition of

volume fraction of active marrow and inactive marrow should be substituted by cellularity volume fraction (marrow space not occupied by adipocytes) and fat volume fraction (*10,11*). This generalization is necessary as in clinical settings; it is difficult to measure the volume occupied by non-hematopoietic cells and structures located in the active marrow (e.g., marrow support cells, vascular structures, marrow stromal cells, and other cells). Therefore, the volume occupied by these non-hematopoietic cells and structures is considered as negligible (*11,12*). Bolch *et al.* (*11*) proposed the use of magnetic resonance imaging (MRI) to quantify the cellularity volume fraction, which is related to the fat volume fraction by the following equation (*11*):

$$(Cellularity\ Volume\ Fraction) \approx 1 - (Fat\ Volume\ Fraction) \qquad \text{equation 1}$$

The use of MRI to quantify fat volume fraction has been validated in experiments with phantoms (*13-15*) and in correlation with biopsy samples in humans (*16,17*), as well by histology analysis of animal bone marrow (*18*).

Quantification of the trabecular bone volume fraction corresponds to a second step in the determination of the volume fractions of trabecular bone and bone marrow space. Some studies (*16,19,20*) point to the use of dual-energy computed tomography (DECT) to quantify the trabecular bone volume fraction. Goodsitt *et al.* (*20,21*) proposed a quantification method, which they validated in a phantom. This method depends on the use of calibration samples attached externally to the patient on the anatomical region, where the bone site of interest is located. Liu *et al.* (*22*) proposed a phantom-less quantification method, which depends on the X-ray beam spectra and the detector sensitivity function.

This work presents the implementation and validation of a methodology to quantify the fat volume fraction in bone marrow using MRI in a clinical setting. Also, it presents the implementation and validation of a methodology to quantify the bone volume fraction (VF_B) in spongiosa (or trabecular bone volume fraction; VF_{TB}) using dual-energy quantitative computed tomography (DEQCT). The methodologies and data described in this work aim at improving the calculation of the absorbed dose in bone marrow dosimetry of patients undergoing molecular radiotherapies.

Chapter II
Background

1. Bone Structure

The adult human skeleton is composed of 75-85% cortical bone, and the remainder is trabecular bone (*2*). Cortical bone is the hard and dense structure that forms the outer wall of all bones (*2*). Trabecular bone is a porous structure composed of a meshwork of bone and is located in the interior of flat bones and the end of long bones (*2*). The ratio of cortical to trabecular bone depends on the bone site. In vertebrae, this ratio is approximately 25:75, while it is 50:50 in the femoral head, and 95:5 in the radial diaphysis (*23*).

Bone is composed of inorganic matter embedded in an organic matrix. The inorganic matter of bone (mineral bone) consists mostly of submicroscopic deposits of calcium phosphate, hydroxyapatite [$Ca_{10}(PO_4)_6(OH)_2$] being the predominant constituent (*2,23*). The organic matrix is composed mainly of collagen and other proteins, carbohydrates, and lipids (*2,21,24*). Approximately 50 to 70% of bone corresponds to the mineral bone, 20 to 40% to the organic matrix, 5 to 10% to water, and <3% to lipids (*23*). Osteogenic cells (osteoblasts) are in charge of the bone formation; they synthesize the organic matrix (osteoid) forming a pre-osseous tissue, then this tissue is undergoing mineralization. Bone remodeling is carried out by osteoclasts, which are capable of resorbing bone (*2,23*).

Two connective tissues form part of the skeleton: i) the periosteum, which is the fibrous connective tissue that covers the surfaces of cortical bone (*23*). ii) The endosteum, which is a layer of endosteal cells that covers the inner surface of cortical and trabecular bone, and also is in contact with the bone marrow space, blood vessel canal, and osteogenic cells (*23*).
The most radiosensitive cells in the human skeleton are i) hematopoietic cells located in the bone marrow, ii) endosteal cells, and iii) epithelial cells located in the bone surfaces in the air sinuses of the skull (*2,25*). The two first groups of cells are dosimetrically important regions in three-dimensional bone marrow dosimetry models (*25*).

1.1. Bone Marrow Structure and Function

The bone marrow, together with the trabecular bone, occupies the central cavities of the long bone, vertebrae, ribs, sternum, flat bones of the cranium, and pelvis (*2,26*). It is a highly cellular tissue that consists of hematopoietic tissue, adipose cells (adipocytes), and non-hematopoietic cells and structures located in the active marrow (e.g., marrow support cells, vascular structures, marrow stromal cells, and other cells) (*2,11,26*).

The hematopoietic tissue is also called red marrow (active marrow). It produces all blood cells: erythrocytes (red blood cells), granulocytes, and monocytes (white blood cells), platelets, and an important portion of lymphocytes (*2,26*). Adipocytes in the bone marrow form the yellow marrow (inactive marrow), which is hematopoietically inactive (*2,26*). Adipocytes tend to form clusters, and the size of the clusters is proportional to the volume fraction of adipocytes (fat) in the bone cavity (*27*).

During human life, a continuing marrow conversion occurs (red marrow turns into yellow marrow). For fetus and newborn, the mass of yellow marrow is almost zero (*10*). The conversion of red marrow into yellow marrow begins during childhood. Dependent on the bone type, the marrow conversion occurs at a different rate. During adulthood, the largest percentage of active bone marrow is located in the axial skeleton (*2,10*).

1.2. Trabecular Bone

Trabecular bone, in comparison with cortical bone, is more metabolically active (*23*). Therefore the remodeling process in trabecular bone is faster than in cortical bone. The estimated average rates for remodeling of compact bone and trabecular bone in adult humans are 3% per year and 18% per year, respectively (*2*).

Bone remodeling is carried out between two key steps: bone resorption and bone formation (*28,29*). During bone resorption, part of the bone matrix is resorbed by osteoclasts, creating a defect (cavity) in the bone surface (*28,29*). Then, this defect is filled with osteoblasts, which initiate the formation of a new organic matrix (collagenous) and mineralization (*28,29*). The difference between the formation of new bone and the resorption of old bone during bone remodeling is called bone balance (*2,23*). During adulthood, the bone balance of trabecular bone is negative (*23*); it means that the resorption of old bone exceeds the formation of new bone (*29*). Therefore, after the skeleton has matured, there is a continual deterioration of the bone network and mass loss of the trabecular bone (*2,9,30,31*).

Gong *et al.* (*32*) found that cortical bone has a higher density (1.99 g/cm^3) than trabecular bone (1.92 g/cm^3). They associate this difference to high mineral content in cortical bone, and the constant resorption and deposit for mineral in the trabecular bone. This observation is consistent with the fact that the more recently formed bone has lower mineralization than older bone (*33*). The chemical composition and density documented by the International Commission on Radiation Units and Measurements (ICRU) in Report 44 (*34*) is used for radiation dosimetry purposes and bone quantification. Previous studies assumed that cortical and trabecular bone has the same chemical elements composition and density (*21,35,36*).

The X-ray micro computed tomography (micro-CT) and magnetic resonance imaging microscopy (micro-MRI) are the two methodologies used for obtaining both two-dimensional histomorphometric data and three-dimensional connectivity of the trabecular bone microstructure (*37*).

2. Quantification of the Fat Volume Fraction in Bone Marrow using Magnetic Resonance Imaging

In clinical routine, the histological analysis of the bone marrow is performed by a bone marrow exam, which is composed of bone marrow aspiration and bone marrow biopsy (*38*). MRI is a non-invasive technique that complements bone marrow aspiration and biopsy (*39*). In contrast to biopsy, MRI is not bound to a specific bone site (*40*). The main role of MRI in bone marrow examinations is the diagnosis and staging of bone marrow diseases, as well as the determination of the right place to obtain a bone marrow biopsy (*39,40*).

The features that MRI adds to the toolset available bone marrow examinations are the high soft-tissue contrast and the possibility to separate adipose tissue from water equivalent tissue (*41*). Furthermore, MRI is a non-ionizing technique; therefore, for radiation protection reasons, MRI provides an attractive option in cross-sectional or longitudinal studies involving humans (*41*).

In the clinical setting, the bone marrow cellularity volume fraction (or only cellularity volume fraction) and the bone marrow fat volume fraction (or only fat volume fraction) are the two concepts used in MRI to refer to the active marrow and inactive marrow (*11,42*). This convention assumes that the volume occupied by non-hematopoietic cells and structures located in the active marrow (e.g., marrow support cells, vascular structures, marrow stromal cells, and other cells) is negligible (*11*). The cellularity volume fraction is the fraction of bone marrow volume occupied by hematopoietic cells (*11*). The fat volume fraction corresponds to the bone marrow volume occupied by adipocytes (*11*). Both concepts are related as given by equation 1.

2.1. Basics of Magnetic Resonance Imaging

The parameters that characterize tissue in magnetic resonance imaging or spectroscopy are T1 relaxation time, T2 relaxation time, T2* relaxation time, and proton density ρ (*43*). In bone marrow images, the proton density contributes very little to the image appearance, as the proton densities of the tissues that compose the bone marrow differ very little (*39*). Therefore, by exploiting the differences in relaxation time of each tissue and by applying the right sequence of magnetic field gradients and radiofrequency (RF) pulses, it is possible to differentiate adipose tissue and water equivalent tissue in the bone marrow.

The chemical element composition of each tissue plays an important role in the formation of the magnetic resonance signal. Atom nuclei composed of an odd number of protons or neutrons, such as the hydrogen nucleus ^{1}H or the phosphorous nucleus ^{31}P, present a net spin (*43,44*). A nucleus with spin has a magnetic moment, which produces a local

magnetic field with opposites poles (dipole) (*44*). As hydrogen exhibits this property and is an abundant element in human tissues with a high gyromagnetic ratio, it is the basis of magnetic resonance imaging and spectroscopy (*43,44*).

In human tissue without an applied magnetic field, the individual nuclear spins of hydrogen atoms are randomly oriented in space, resulting in a zero net nuclear spin moment (*43*). Applying a strong external magnetic field B_0, a fraction of the nuclear spins will orient parallel to B_0 (creating a net magnetic nuclear moment M_0), and also, they will precess (rotate) around B_0 (*44*). The frequency at which the nuclear spins precess is proportional to the magnetic field, and it is described by the Larmor equation:

$$\nu = \frac{\gamma}{2\pi} B_0 \qquad \text{equation 2}$$

Here, ν is the resonance frequency of the nuclear spins, γ is the gyromagnetic ratio, and B_0 is the magnetic field. The gyromagnetic ratio is a constant inherent to the nucleus (*44*). For hydrogen, $\gamma/2\pi$ is equal to 42.58 MHz/T (*43*).

The application of a radiofrequency (RF) magnetic field B_1 (applied perpendicular to B_0), on the tissue or sample under B_0, generates a reorientation of individual magnetic moments in space (*43,44*). This reorientation results in a displacement of the net magnetic nuclear moment (M_0) by an angle α from the z-axis (axis parallel to B_0) that produces a decomposition of M_0 into a z-axis component (M_Z) and a xy-plane component (M_{XY}) (*43*). No net change in the orientation of the magnetic moments occurs if B_1 does not match the resonance frequency of M_0 (*43*).

Part of the energy introduced by the RF pulse is absorbed by the nucleus and subsequently emitted (*44*). This emitted energy induces a voltage that can be detected by a suitably tuned receiver coil (*44*). This process of absorption and emission from the nucleus can also be explained by the dynamic of the vector components M_Z and M_{XY}. Immediately after the application of B_1, the nuclear moments begin to re-align with B_0. It means that the component M_Z increases, and M_{XY} decreases (*43*). This reduction in M_{XY} produces a free induction decay (FID) curve (*43,44*). M_Z will restore its original magnitude (M_0) in the absence of new RF pulses. Therefore, these relaxation processes will bring the system back to thermal equilibrium (*44*).

The formation of the magnetic resonance images or spectra is carried out through the application of multiple RF pulses to generate multiple FIDs, which are then averaged: First, to obtain a signal-averaged FID, and second, to improve the signal-to-noise ratio (SNR) (*44*). The signal-averaged FID is a time-domain signal; therefore, it requires the application of a Fourier transform to form an image or a frequency spectrum (*44*).

2.2. *Magnetic Resonance Parameters*

2.2.1. *T1 Relaxation Time*

The T1 relaxation time is also called the spin-lattice relaxation time. Spin-lattice relaxation corresponds to the exponential recovery of M_Z, and it depends on the interaction of nuclear spins with the lattice (the molecular arrangement and structure) (*43,45*). The T1 relaxation time constant is the time required by the nuclear spins to achieve 63% of the longitudinal magnetization M_Z, after a 90-degree pulse (when $M_Z = 0$) (*43,45*). Mathematically, it can be described by the following equation:

$$M_Z(t) = M_0 \cdot (1 - e^{-t/T_1}) \qquad \text{equation 3}$$

In equation 3, $M_Z(T_1) = 0.63\, M_0$.

The T1 relaxation depends on the efficiency with which the energy absorbed by nuclear spins is transferred to the surrounding molecular lattice (*45*). Fat has a shorter T1 relaxation time than water (*46*). This difference is due to the medium size of fat molecules, which form a more structured lattice with a vibrational frequency distribution that permits a better energy transfer between spins and lattice (*45*).

2.2.2. *T2 Relaxation Time*

The T2 relaxation time is also called the spin-spin relaxation time. It corresponds to the time required by the nuclear spins to decay to 37% of the transversal magnetization M_{XY} after a 90-degrees pulse (when $M_Z = 0$) (*43,45*). Mathematically, it is described by the following equation:

$$M_{XY}(t) = M_0 e^{-t/T_2} \qquad \text{equation 4}$$

In equation 4, $M_Z(T_2) = 0.37\, M_0$.

After a 90-degree pulse, the nuclear spins are phase-coherent, but field inhomogeneities in the sample and differences in the speed at which the nuclear spins precess (some faster than others) result in dephasing process which reduces M_{XY} and produces the FID (*43,45*) (see chapter 2.1).

When inhomogeneities from the main magnetic field B_0 are considered, T2 is called T2* (*43*), which is typically shorter than T2.

2.2.3. T1 and T2 of Fat and Water

Stanisz *et al.* (*47*) measured the T1 relaxation time in the human liver, muscle, optic nerve, spinal cord, heart, kidney, white and gray matter, cartilage, and blood in a 3 T MR. They documented T1 values of 1932 ± 85 ms for blood, which is a tissue with a high concentration of water (*48*), and 812 ± 64 ms for the liver, which has a considerable concentration of fat (*46,49*). The T2 relaxation times at the same field strength documented by Stanisz *et al.* (*47*) of 275 ± 50 ms for blood and 42 ± 3 ms for the liver. These values correspond to the maximum and minimum measured value.

Small molecules such as water exhibit long T1 and T2, while molecules of intermediate molecules size as fat have short T1 and T2 (*45-47*).

2.3. Quantification of the Fat Volume Fraction using Magnetic Resonance Spectroscopy (MRS)

MRS is typically used to explore and quantify the biochemical composition of human tissue or fluid (*46,50*). As presented earlier, only atoms with an odd mass number (e.g., ^{1}H, ^{31}P, ^{13}C) possess net magnetic moment and behave as dipoles under the influence of a magnetic field (*44,50*). In a magnetized sample, the resonance absorption by ^{1}H nuclei will occur only when they are exposed to an electromagnetic signal at their Larmor precession frequency (*44,46,50*) (equation 2). The resonance frequency for ^{1}H nuclei is 63.87 MHz at B_0 = 1.5 T and 127.87 MHz at B_0 = 3 T. The resonance absorption by ^{1}H nuclei is possible thanks to the transition between its two energy levels ($2l + 1$; parallel and antiparallel magnetic moment orientation) product of a nuclear spin quantum number $l = 1/2$ (*50*). The energy between the two levels (ΔE) is:

$$\Delta E = \hbar \gamma B_0 \qquad \text{equation 5}$$

Here, $\hbar$ is the Planck's constant (divided by 2π), γ is the gyromagnetic ratio, and B_0 is the magnetic field.

An MRS acquisition starts with the acquisition of magnetic resonance images of the anatomical region of interest (the so-called localizers). Then, single-voxel spectroscopy (SVS) is carried out by positioning a single voxel in the tissue under investigation (*51*). Previous to performing the spectroscopy, ^{1}H MRS requires a uniform magnetic field to achieve a high SNR. This optimization process of the magnetic field in the voxel is called shimming (*46,51*). Then, a set of RF pulses are applied. Immediately, during relaxation, radiofrequency signals are generated, creating an FID, which consists of a superposition of all resonance from the sample (*50*). Finally, the FID is decoded using the Fourier transformation method (*50*).

2.3.1. The Chemical Shift in MRS

The use of a broad-bandwidth RF pulse to stimulate the tissue in the voxel and the reception of multiple resonance frequencies is necessary to measure the chemical shift. The resonance frequency of ^{1}H nuclei depends on the chemical structure of the molecule (mainly the movement of the closest electrons) in which they reside (*50*). The chemical shift corresponds to the difference in the resonance frequency of ^{1}H due to the electronic environment, which shields the ^{1}H nuclei, creating variations in the local magnetic field (*52*). Therefore, the chemical shift is a molecule-specific value. equation 2 can be redefined to consider the shielding effect:

$$\nu = \frac{\gamma}{2\pi} B_0 (1 - \sigma) \qquad \text{equation 6}$$

Here σ is the shielding constant. $B_0\sigma$ can be considered as an induction magnetic field B_{ind}, which is caused by the circulating electrons around the nucleus.
Mathematically the chemical shift δ_{sample} is defined as (*52*):

$$\delta_{\,^1H,sample} = \left(\frac{\nu_{\,^1H,sample} - \nu_{\,^1H,reference}}{\nu_{\,^1H,reference}} \right) \times 10^6 \qquad \text{equation 7}$$

Here, ν_{sample} is the frequency of the sample under investigation, and $\nu_{reference}$ is the frequency of a reference compound. Tetramethylsilane (TMS) was the first reference compound selected by consensus for ^{1}H MRS (*52*). The chemical shift can be reported as *ppm* (parts per million) by removing the term $\times 10^6$ in equation 7. Therefore the chemical shift value of TMS is 0.0 ppm. In case of water, the chemical shift is 4.7 ppm, while the human liver fats (lipids) present multiple peaks 0.9 ppm, 1.3 ppm, 2.1 ppm, 2.75 ppm, 4.2 ppm, and 5.3 ppm (*53*).

2.3.2. Single Voxel Spectroscopy

In ^{1}H MRS, the most common single voxel spectroscopy techniques are STEAM (stimulated-echo acquisition mode) and PRESS (point-resolved spectroscopy) (*46,51*). STEAM and PRESS are MR pulse sequences. A pulse sequence is a set of RF (and/or gradient) magnetic field pulses with specific timing and order of repetition (*43,54*). The time between the beginning of the pulse sequence and the beginning of the succeeding pulse sequence is called repetition time TR (*54*). The time between the center of the RF pulse and the center of the spin-echo (refocusing of spin) is called echo time TE (*54*).

In STEAM, the acquisition is performed after three 90° excitation pulses, while in PRESS, it is performed after one 90° excitation pulse and two 180° excitation pulses (*51,55*). Both sequences are accompanied by X, Y, and Z gradients used to select the slice in the corresponding direction (*51,55*).

2.3.3. MRS for Fat Volume Fraction Quantification

In the spectra obtained from MRS, the area under the peak represents the concentration of the chemical compound (*46,50*). Therefore the reported values correspond to ratios or fractions (area of a specific peak divided by the sum of all quantified peak areas). Mathematically, the fat volume fraction (VF_F) is defined as:

$$VF_F = \frac{F}{F + W} \qquad \text{equation 8}$$

Here, F and W represent the areas under all fat (lipid) peaks and the water peak, respectively.

Ballon *et al.* (*56*) measured the marrow cellularity volume fraction ($1 - VF_F$) in iliac crests by biopsy and MRS (using a 1.5 T MR system and a STEAM sequence). They found that the quantification of cellularity by MRS showed a good correlation with a biopsy analysis ($r = 0.94$, $p < 0.001$). However the linear fit parameters (slope = 0.94 ± 0.04, intercept = 8.1 ± 2.9) show that MRS overestimated the cellularity approximately 8.1%.

Posterior studies by Shick et al. (*57*), Pansini et al. (*58,59*), Li *et al.* (*60*), and Schellinger *et al.* (*61*) used MRS to quantify the fat volume fraction in multiple bone sites. These studies explore the influence of age and sex on fat volume fraction, as well as the feasibility of using the fat volume fraction as a biomarker in subjects with leukemia.

Ren *et al.* (*62*) measured the composition of bone marrow fat by MRS (using a 7 T MR system and STEAM sequence). They identified seven chemical groups with the respective chemical shift: $-CH_3$ (0.90 ppm), $-(CH_2)_n-$ (1.30 ppm), $-CH_2-CH_2-COO$ (1.59 ppm), $-CH_2-CH=CH-CH_2-$ (2.03 ppm), $-CH_2-COO$ (2.25 ppm), $=CH-CH_2-CH=$ (2.77 ppm) and $-CH=CH-$ (5.31 ppm). Hamilton *et al.* (*53*) measured the chemical shift of water and fats in the liver. For water, they documented a chemical shift equal to 4.70 ppm. Therefore, the chemical shifts of water and olefinic molecules (-CH=CH-) are close. Thus, in clinical MR systems (magnetic field of 1.5 T or 3 T), it is possible that these two peaks cannot be resolved, resulting in an underestimation of the measured fat volume fraction when the fat volume fraction in the sample increases. Some studies (*58-60*) quantified the fat volume fraction using only the area under methylene [$-(CH_2)_n-$] and water peak.

2.4. Quantification of the Fat Volume Fraction Using Magnetic Resonance Imaging

Fat volume fraction quantification using MRI is based on water/fat separation by chemical shift imaging. Two imaging techniques make use of the difference in chemical shift between water and lipids (fat) to create separate images: i) chemical shift-selective (CHESS) MRI and ii) chemical shift-encoded (CSE) MRI (*63*). CSE provides a more uniform fat/water separation than CHESS in large fields of view, such as the abdomen, spine, and pelvis (*63,64*). In this work, chemical shift-encoded MRI, specifically the two-point Dixon Method, was applied.

2.4.1. Two-Point Dixon Method

Dixon (*65*) proposed the first chemical shift-encoded imaging method to separate water and fat. Dixon's method takes advantage of the difference between the frequency precession of spins in water and fat (manly methylene). This difference is associated with the chemical shift difference between water and fat: *4.70 ppm (water) minus 1.30 ppm (methylene) equals 3.4 ppm* (*53*). The frequency difference associated with this chemical shift difference is defined by:

$$\Delta\nu = \frac{\gamma}{2\pi} \times B_0 \times \Delta\delta\,{}^{1}{}_{H} \qquad \text{equation 9}$$

For an MR system of 1.5 T, equation 9 results in:

$$\Delta\nu = 1.5T \times 42.58\frac{MHz}{T} \times 3.4ppm \approx 217\ Hz$$

In a 3 T MR system, $\Delta\nu \approx 434\ Hz$. Both values are approximations to illustrate the range of $\Delta\nu$; they are based on chemical shift values reported by Hamilton *et al.* (*53*).

After an RF pulse, both vectors (fat and water) point in the same direction or in-phase (maximum magnetization). Subsequently, their magnetization vectors rotate with a different frequency until they are out of phase (minimum magnetization) (*64,65*). The time between each state in an MR system of 1.5 T is:

$$t = \frac{1}{2 \times \Delta\nu} = a \qquad \text{equation 10}$$

For an MR system of 1.5 T, equation 10 results in:

$$t = \frac{1}{2 \times 217\ Hz} \approx 2.30\ ms$$

In a 3 T MR system, $a \approx 1.15\ ms$. Both values are approximations to illustrate the range of Δv; they are based on chemical shift values reported by Hamilton *et al.* (*53*).

In the two-point Dixon method, two images are acquired: one out-of-phase ($t = a$) and a second in-phase ($t = 2a$) image (*64,65*). Thus, more out-of-phase images can be acquired as in impair multiples of a ($t = 3a, 5a, ...$), while in-phase images can be acquired as even multiples of a ($t = 4a, 6a, ...$), each time with a lower amplitude. This characteristic is used in multi-point Dixon sequences (*66*).

A pure water image is obtained by the sum of the signals of out-of-phase, SOP, and in-phase images, SIP (*64,67*):

$$W = \frac{|SIP + SOP|}{2} \qquad \text{equation 11}$$

A pure fat image is obtained by the subtraction of the signals of out-of-phase from the in-phase images (*64,67*):

$$F = \frac{|SIP - SOP|}{2} \qquad \text{equation 12}$$

A perfect quantification of water and fat would be achieved if the water and fat signal were perfectly aligned in-phase and out-phase. In practice, B_0 inhomogeneities (local variations in the field strength) produce local variations of the signal phase, which results in incomplete separation of water and fat (*64,67,68*). This incomplete separation causes that part of the water and fat signals could be detected in the opposite regime.

The three-point Dixon method was introduced later by Kim *et al.* (*69*) and extended by Lodes *et al.* (*70*) and Glover and Schneider (*71*). This method added a third image to correct the phase errors caused by B_0 inhomogeneities (*64*). Other implemented corrections to Dixon's method are the simultaneous estimation of T_2^* during relaxation (*72,73*), the modeling of multiple fat resonances (*74,75*), multi-point sequences (*66*), and asymmetrically acquired echoes (iterative decomposition of water and fat with echo asymmetry and least-squares estimation) (*76*). Some of these modifications to the Dixon method are still not fully

implemented in commercial MRI (*66,77*). A complete description of these modifications to the original Dixon method is beyond the scope of this study.

2.4.2. MRI Fat Volume Fraction Quantification

MRI-based fat volume fraction quantification using MRI is based on obtaining two images; one corresponds to the fat signal, the second corresponds to the water signal. By applying equation 8 on a voxel-by-voxel basis, it is possible to calculate the fat volume fraction in MRI (*8,78,79*):

$$VF_{F,i} = \frac{F_i}{(W_i + F_i)} \qquad \text{equation 13}$$

Here, $VF_{F,i}$ corresponds to the fat volume fraction value, W_i for the *i*-th voxel of the water image, and F_i the *i*-th voxel of the fat image. By segmenting a volume of interest (VOI), it is possible to obtain a mean value of the VF_F in the VOI.

In non-invasive studies that quantify the fat volume fraction, MRS is often used as a reference standard for MRI (*80*). Publications by Longo *et al.* (*81*), Thomsen *et al.* (*82*), and Syczepaniak *et al.* (*83*) provided proof to accept the use of MRS as a reference standard in the liver fat assessment. Following this approach, studies as Pichardo *et al.* (*18*) and Li *et al.* (*84*) quantified the fat volume fraction in bone marrow by using MRS as a reference standard for MRI. They documented a good agreement between both techniques. Recently Le Ster *et al.* (*73*), Baum *et al.* (*85*), and Karampinos *et al.* (*86*) showed that quantification of the fat volume fraction in vertebral bone marrow is feasible and proposed the implementation of T_2^* correction by multi-point chemical shift-encoding based water/fat separation (Dixon-based) MRI.

3. Quantification of the Trabecular Bone Volume Fraction using Dual-Energy Computed Tomography

Computed tomography (CT) provides complementary information in the study of the spatial composition of bone and bone marrow. While MRI provides better soft-tissue contrast and the possibility to separate fat and water in bone marrow, CT provides superior delineation of fine bony detail and the possibility to quantify the mineral bone density (*87-89*).
Quantification of the trabecular bone volume fraction (VF_{TB}) is a second step after the determination of fat and cellularity volume fractions. Some studies (*16,19,20*) point to the use of dual-energy computed tomography (DECT) to quantify the VF_{TB}.

3.1. Basics of Computed Tomography

3.1.1. Computed Tomography Image Formation

CT images are based on the transmission of X-rays through the patient along a line of finite-thickness to generate transmission profiles from different angles around the patient (*45,90*). The X-ray tube and a detector array are the two main components of a CT-scanner; the patient or sample under investigation is placed in the center of both components. The X-ray tube is used to irradiate the patient and to create transmission profiles, which are acquired by the detector array on the opposite side of the tube (*91*).

Around 1000 view angles are acquired to generate a sinogram ($I(x,\theta)$), where x corresponds to the position in the detector array and θ to the tube angle position (*91*):

$$I(x,\theta) = I_0 e^{-\mu_{eff} t(x,\theta)} \qquad \text{equation 14}$$

Here, μ_{eff} is the effective X-ray linear attenuation coefficient of the tissue in the patient or sample, t is the thickness of the patient or sample along the ray path through the patient defined by the geometrical parameters x and θ. I_0 is the unattenuated intensity measured for a reference detector when there is no anatomy in the beam path (*45,91*).

Equation 14 can be re-expressed as:

$$P(x,\theta) = ln\left[\frac{I_0}{I(x,\theta)}\right] = \mu_{eff} t(x,\theta) \qquad \text{equation 15}$$

Here, $P(x,\theta)$ is the projection function, and it is used by image-reconstruction algorithms to create the CT image. The reconstructed image is formed with the value of the attenuation coefficient ($\mu_{x,y,z}$) of each voxel (*45,91*).

Lastly, the attenuation coefficient image is normalized to the linear attenuation coefficient of water (μ_w) (*91*):

$$HU_{x,y,z} = 1000\left(\frac{\mu_{x,y,z} - \mu_w}{\mu_w}\right) \qquad \text{equation 16}$$

Here, $HU_{x,y,z}$ is the Hounsfield Unit or CT number for a voxel located at position (x,y,z).

3.1.2. Parameters Affecting Image Quality

CT image quality is affected by many parameters, the most relevant for this study are: X-ray-tube potential (*V*, generally in units of kV), tube current (*J*, generally in units of mA), exposure time (*t*, generally in unit of s), pitch (p), reconstruction kernel and slice thickness (*45,91*). The X-ray-tube potential used in CT stays between 70 kV and 150 kV (*91*) (*92*). The use of low X-ray-tube potential (70 kV to 80 kV) improves the soft-tissue contrast, and it is more useful in thin, non-obese patients or children (*92*). However, it is more likely that the image shows beam-hardening artifacts (attenuation of lower energy photons), even in small children (*91*). High X-ray-tube potential (130 kV to 140 kV) is mainly used in CT imaging of adult patients (*91*).

The tube current-exposure time product (mAs) corresponds to the product of tube current (*J*) and exposure time (*t*) (*91*). This parameter influences the number of X-ray photons used to generate the CT image (*45*). Therefore it is related to the signal-to-noise ratio (SNR) and contrast resolution in CT images (*45,91*).

In helical CT scanners (modern CT systems), the ratio between the table movement (mm) per 360˚ rotation of the X-ray tube (b) and the collimator width (mm) at isocenter (T) is defined as the collimator pitch (*45,91*):

$$p = \frac{b}{T} \qquad \text{equation 17}$$

In multiple detector CT (MDCT) systems with n detector arrays equation 17 is redefined as:

$$p = \frac{b}{nT} \qquad \text{equation 18}$$

The pitch affects the spatial resolution (a high pitch value reduces the resolution), and also the image noise increases as the pitch increases (*45,91*).

A reconstruction algorithm is typically used to transform the raw image data into a tomographic image (*91*). As one of the most important reconstruction parameters, the kernel refers to the shape of the filter function in the spatial domain (*45*) and impacts the spatial and contrast resolution (*91*). They are designed to optimize the visualization of different tissue types. Bone filters have the best spatial resolution but a low contrast resolution (*45*). In contrast, the soft tissue filters have a low spatial resolution at a high contrast resolution (*45*).

The slice thickness is the thickness of a CT image measured at the isocenter (*91*). Slice thicknesses values between 0.5 mm and 10 mm are achievable in modern CT systems (*91*). The spatial resolution is reducing for large slice thickness. Statistically thicker slices collect more signal than thin slices, leading to a better SNR.

3.2. Dual Energy Quantitative Computed Tomography (DEQCT)

DECT is an imaging procedure based on the acquisition of two image datasets using two different X-ray-tube potential (energy spectra) (*93*). DEQCT is the use of a material decomposition algorithm in combination with the DECT image datasets to characterize different materials based on their chemical element composition (*88,93*).

In CT image formation, the main X-ray interactions with matter are the photoelectric effect, Compton scattering and Rayleigh scattering (small contribution) (*94*). The relative importance of these interactions depends on the photon energy and the atomic number Z of the interaction medium (*95*). In the energy range of diagnostic X-rays, the value of the attenuation coefficient (μ) or mass attenuation coefficient (μ/ρ) (ρ corresponds to the density of the interaction medium) is defined by the contribution of the Compton effect (σ/ρ) and photoelectric effect (τ/ρ). The fundamental principle of dual-energy imaging is the fact that each material has an associated mass attenuation coefficient when interacting with X-rays (*22*). Thus, material decomposition (ability to decompose a material into its constituent sub-materials) using DECT data is based on the energy- and element-dependent nature of X-ray attenuation (*88*).

Liu *et al.* (*22*) summarized and classified the dual-energy CT material decomposition algorithms previously studied as: i) spectral basis (ρZ methods) pre-reconstruction (*96*) and post-reconstruction (*94*), and ii) basis material (two material) pre-reconstruction (*97,98*). Also, Liu *et al.* (*22*) introduced a basis material (three material) post-reconstruction algorithm.
Pre-reconstruction material decomposition algorithms have the advantage that they can correct for beam hardening by preprocessing of raw data (*22,88*). However, post-

reconstruction algorithms are relatively easy to implement and execute and, therefore, more practical in clinical situations (*22,88*).

The basis material algorithms can determine the mass fraction, while ρZ methods provide only the effective density (ρ) and the effective atomic number (Z) (*22*). Therefore, the basis material algorithms are more useful for clinical applications.

Material decomposition algorithms have the advantage of being phantom independent. It means that they do not require additional calibration phantoms next to the patient during image acquisition. In contrast, another DEQCT method was introduced by Goodsitt *et al.* (*20,21*). It requires the use of a set of calibration standards located externally to the patient.

In this work, the method proposed by Liu *et al.* (*22*) was implemented. A detailed description of this method is presented in chapter III (methods) - section 2.1.

4. Bone Marrow Dosimetry for Molecular Radiotherapy

The importance of bone marrow dosimetry lies in the need to predict the level of bone marrow toxicity in molecular radiotherapies. Bone marrow dosimetry is part of a more integral procedure called treatment planning, which involves the determination of the amount of administered activity that maximizes tumor control probability and does not exceed the dose limit of risk organs or tissues.

Glatting *et al.* (*3*) summarized the patient-based treatment planning in molecular radiotherapy as:

- the quantification of patient-specific pharmacokinetics,
- the calculation of the absorbed dose in target and risk organs or tissues (e.g., bone marrow),
- the prediction of deterministic biological effects (e.g., bone marrow toxicity),
- the determination of the amount of activity to be administered.

This work is focused on the quantification of the volume fraction of fat, cellularity, and trabecular to improve the calculation of the absorbed dose in bone marrow dosimetry. Therefore, only theory and antecedents related to the second step (calculation of the absorbed dose) are going to be explained in the next sections.

4.1. Calculation of the Absorbed Dose in Internal Radiation Dosimetry

Internal radiation dosimetry is the calculation of the radiation energy deposition in tissue by radionuclides administered in the body (*25*). The main concept of internal radiation dosimetry is the absorbed dose (*D*), which is defined by the international commission on radiation units and measurements (ICRU) (*99*) as the quotient of $d\bar{\varepsilon}$ by dm, where $d\bar{\varepsilon}$ is the mean energy imparted by ionizing radiation to a matter of mass dm, thus:

$$D = \frac{d\bar{\varepsilon}}{dm} \qquad \text{equation 19}$$

The units are J kg^{-1}, the specific unit for absorbed dose is the Gray (Gy).

For a better understanding of the absorbed dose concept, it is important to clarify the concept of the mean energy imparted ($\bar{\varepsilon}$). The ICRU (*99*) defines the mean energy imparted to the matter in a given volume as the mean radiant energy, R_{in}, of all charged and uncharged ionizing particles that enter the volume minus the mean radiant energy, R_{out}, of all charged and uncharged ionizing particles that leave the volume, plus the mean sum, $\sum Q$, of all changes

of the rest energy of nuclei and elementary particles that occur in the volume ($Q > 0$: decrease of rest energy; $Q < 0$: increase of rest energy); thus:

$$\bar{\varepsilon} = R_{in} - R_{out} + \sum Q \qquad \text{equation 20}$$

In medicine, a widely accepted approach for internal radiation dosimetry was developed by the Medical Internal Radiation Dose (MIRD) Committee of the Society of Nuclear Medicine (SNM), and it is referred to as the "MIRD formalism" (*25*).

The MIRD pamphlet No. 21 (*4*) describes the absorbed dose $D(r_T)$ as the mean energy imparted to a target tissue (or region) r_T per unit tissue mass. Also, it defines the mean absorbed dose rate $\dot{D}(r_T)$ as the time-dependent rate at which the absorbed dose is delivered to a target tissue r_T within a patient from a radioactive material distributed uniformly within source r_S at time t after administration:

$$\dot{D}(r_T) = \sum_{r_S} A(r_S, t) S(r_T \leftarrow r_S, t) \qquad \text{equation 21}$$

Here, $A(r_S, t)$ is the time-dependent activity of the radiopharmaceutical in source tissue r_S, and $S(r_T \leftarrow r_S, t)$ is a radionuclide-specific quantity representing the mean absorbed dose rate to a target tissue r_T at time *t* after administration per unit activity present in source tissue r_S (*4*).

The spatial and temporal distribution of activity in the source tissue, r_S, and target tissue, r_T, can be determined by processing images correctly calibrated and obtained from single-photon emission computed tomography (SPECT) or positron emission tomography (PET) (*4*). In the specific case of blood, the activity is quantified by blood sampling (*6*).

The quantity $S(r_T \leftarrow r_S, t)$ is a central concept in this work. The MIRD pamphlet No. 21 (*4*) describes $S(r_T \leftarrow r_S, t)$ as the absorbed dose rate per unit radioactivity. This quantity is specified for the radionuclide as well as the age and sex of the anatomic model chosen to represent the patient or tissue of interest. Then, to calculate the value of S, it is necessary to create a computational phantom of the whole-body, organ, or structure which represents reference individuals of a given age, sex-, total-body mass, and height (*4*). The computational models are based on the segmentation of CT, micro-CT or MR images, or analysis of histological images (*4,18,100*). S can be decomposed as (*4*):

$$S(r_T \leftarrow r_S, t) = \frac{1}{M(r_T, t)} \sum_i E_i Y_i \phi\,(r_T \leftarrow r_S, E_i, t) \qquad \text{equation 22}$$

Here, E_i is the mean (or individual) energy of the *i*-th nuclear transition, Y_i is the number of *i*-th nuclear transitions per nuclear transformation, $\phi(r_T \leftarrow r_S, E_i, t)$ is the absorbed fraction (defined as the fraction of radiation energy E_i emitted within the source tissue r_S at time t that is absorbed in the target tissue r_T), and $M(r_T, t)$ is the time-dependent mass of the target tissue r_T in the reference individual (*4*).

A time-independent formulation of equation 21 can be obtained by integration over the dis-integration period T_D (commonly set to be infinity) after administration of the radioactive material to the subject (*4*):

$$D(r_T, T_D) = \int_0^{T_D} \dot{D}(r_T)dt = \sum_{r_S} \int_0^{T_D} A(r_S, t) S(r_T \leftarrow r_S, t)dt \qquad \text{equation 23}$$

$$= \sum_{r_S} \tilde{A}(r_{S,T_D}) S(r_T \leftarrow r_S) \qquad \text{equation 24}$$

Here, $\tilde{A}(r_{S,T_D})$ is the time-integrated activity (or the total number of nuclear transformations) in source tissue r_S over the dose-integration period T_D. The determination of $\tilde{A}(r_{S,T_D})$ comprises the estimation of pharmacokinetic parameters by the mathematical fit of the time and activity data (biokinetic data) obtained from the quantification of the spatial and temporal distribution of activity in the source tissues, r_S, and the target tissues, r_T. In equation 23, it is assumed that the time dependence of S is neglected when the source and target masses remain constant throughout irradiation (*4*).

The calculation of appropriate S values has been an important task since Spiers and collaborators (*101-105*) at the University of Leeds proposed the first model of bone and bone marrow for radiation transport in 1976. The next sections are dedicated to explaining the role of the radiation transport model in the determination of S values for bone marrow dosimetry.

4.2. Elements of a Radiation Transport Model

A radiation transport model is a computational representation, which reproduces the geometry and material composition of the human body, an organ, or a specific tissue. By using a Monte Carlo simulation code, it is possible to (*106*):

- generate charged and uncharged ionizing particles,
- simulate the physical interactions of particles with the phantom,
- track all interactions of each particle with the phantom, and
- store information about all interactions (e.g., particle type, positions, energy depositions, generation of new particles).

From the stored information about particle interactions, it is then possible to quantify the absorbed fraction ($\phi(r_T \leftarrow r_S, E_i, t)$) for source and target organs or tissues. Subsequently, the S values can be calculated from the absorbed fraction (see equation 22).

4.2.1. The Computational Phantom in Radiation Transport Simulation

A computational phantom is a geometrical representation of the human body, an organ, or a specific tissue of interest. In radiation transport simulations, the main role of computational phantoms is to provide a medium for the Monte Carlo simulation in which the simulated particles can interact as in the real tissue (*25*). Therefore, information related to the material composition of the organ or tissue of interest is required, as well as the spatial distribution of the radioactive source (radionuclide).

The increase in the detail level of computational phantoms has been linked to the increases in the size and speed of computers. Early designs were arrangements of simple forms such as spheres, cylinders, or discs, with a simplistic material description (mainly water) (*25*). The current computational phantoms are based on three-dimensional imaging techniques such as CT, micro-CT or MRI, or analysis of histological images (*25,100*). This approach leads to the development of voxel-based phantoms (*25,107*). One step forward from voxel-based phantom are the boundary representation (BREP) phantoms, which are based on voxel geometry, but their stepped surfaces have been replaced by polygon meshes (PM) and/or non-uniform rational B-splines (NURBS) (*108*). These phantoms permit organ motion (e.g., cardiac or respiratory motion) (*109*), a better description of microstructures such as trabecular bone and adipocytes distribution in bone marrow (*19,100,110,111*), and lower voxel effects (overestimation of the surface area of a structure) when transporting particles within three-dimensional images of trabecular bone samples (*112*).

4.2.2. The Monte Carlo Method in Radiation Transport Simulation

The main role of the Monte Carlo methods for radiation transport is to simulate the interactions of the ionizing particles with the phantom (matter) based on known probabilities of occurrence, which are calculated by the random sampling of probability density functions (PDFs) (*25*).

The fundamental components of a Monte Carlo simulation method are the PDF and the random number generator.

A PDF describes a physical system and defines for a given step in the simulation the range of possibilities (e.g., particle interaction) and the relative probability of those possibilities (e.g., cross-section) (*25,113*)

To reproduce the random nature of radioactive decay and particle interaction, the generation of random numbers is fundamental in any Monte Carlo radiation method. A random number generator is a source of random numbers uniformly distributed on a unit interval (*25*).

4.3. Bone and Bone Marrow Radiation Transport Models

The first bone and bone marrow models for radiation transport were presented by Spiers and collaborators (*101-105*) at the University of Leeds. They described the three-dimensional structure of trabecular bone by measuring the linear path length though trabecular and marrow cavities. From the measured linear path length, they created a chord length distribution of bone and marrow space (*25*). This data was used in posterior models such as by Snyder *et al.* (*114*), ICRP publication 30 (*115*), Eckerman *et al.* (*116,117*), and Bouchet *et al.* (*118,119*).

More sophisticated image-based three-dimensional models were developed later at the University of Florida, by using micro-MR images of trabecular bone samples (*120,121*) and later micro-CT images (*35*). Lastly, Hough *et al.* (*111*) and O'Reilly *et al.* (*110*) developed a skeletal dosimetry model for the ICRP-defined reference adult male and female (Publication 110) (*122*), respectively, based on Shah *et al.* (*35*). The last part of this section is a description of more recent advances carried out using image-based models.

4.3.1. Image-based Models

Multiple models and improvements in the field of bone and bone marrow dosimetry have been presented by Bolch and collaborators at the University of Florida since 1999 (*18,19,35,36,100,110-112,118-121,123-128*).

Jokisch *et al.* (*120,121*) presented a voxel-based transport simulation by using MRI microscopy. In these studies, four vertebral bodies were extracted from the thoracic section of a 52-year-old male cadaver, and imaging was performed in a 14.1 T micro-MR system. To perform the radiation transport simulation in the voxel-based model, the infinite trabecular region transport model was introduced, which reintroduces the particles (electrons) that leave the trabecular bone space (trabecular bone sample size: 8.26 mm $\times$ 7.80 mm $\times$ 8.26 mm). Also, they developed a macrostructural transport model to simulate the interaction with the cortical bone. In this model, the particles are allowed to leave the trabecular bone region after traveling a respective distance (inside of the infinite trabecular region transport model) until they reach a cortical bone boundary, from which they cannot escape (total energy deposit).

Later, Patton *et al.* (*123*) expanded Jokisch's model by introducing a larger trabecular bone sample size 2 cm $\times$ 2 cm $\times$ 4 cm (imaging was performed in a 20 cm wide bore 4.7 T micro-MR system) and cortical bone structures obtained from CT images. The Patton model

differs from Jokisch model in: i) the geometrical description of cortical bone, ii) particle radiation transport in cortical bone, which permits particles to cross the cortical bone and also backscatter from the medium (muscle) around cortical bone, and iii) reintroduction of particles is not required due to the large size of trabecular the bone sample.

One step forward was presented by Bolch *et al.* (*11*), who used the Jokisch's model and explicitly introduced the spatial distributions of adipose tissue into the radiation transport model. The Bolch model simulates the presence of adipocyte cell clusters by random voxel selection of voxels from the marrow space (not occupied by trabecular bone). Then, they created images with the same trabecular bone structure (image-based) plus different percentages of occupancy of adipocyte-voxel-based cell clusters (fat volume fraction), specifically 0%, 20%, 50% and 90% fat volume fraction.

Shah *et al.* (*35,129*) used Jokisch's model (*120,121*), including improvements by Patton *et al.* (*123*) and Bolch *et al.* (*11*). Also, in a previous publication, Shah *et al. (100)* studied the adipocyte spatial distribution in bone marrow, giving place to a more realistic model of adipose tissue based on the analysis of histological samples. The results of this study were included in publication by Shah *et al.* (*35*). Shah's model considers three source tissues: active marrow (AM), trabecular bone surfaces (TBS) defined as a 0.1 μm tissue layer on the marrow side of the bone-to-marrow space interface, and trabecular bone volume (TBV). It considers as target tissues the AM and the trabecular bone endosteum (TBE), defined as a 10 μm tissue layer from the bone-to-marrow space interface. Also, other tissues with which the particle interacts, such as cortical bone volume (CBV), inactive marrow (IM), and surrounding tissues (muscle, soft tissue, or vertebral disks).

The Shah model was used by Pafundi *et al.* (*130*) to create an image-based skeletal dosimetry model for the ICRP reference newborn (based on an autopsy of two newborn females with ages of 4 days and 5 days) implemented in the Monte Carlo code EGSnrc (*131*). Also, Hough *et al.* (*111*) created an image-based skeletal dosimetry model for the ICRP reference adult male (based on a 40 years-old male cadaver) implemented in the Monte Carlo code EGSnrc (*131*). Lastly, O'Reilly *et al.* (*110*) created an image-based skeletal dosimetry model for the ICRP reference adult female (based on a 45 years-old female cadaver) implemented in the Monte Carlo code MCNPX v2.7 (*132*). These publications used Shah's model, including improvements developed by Hurtado *et al.* (*133*) and Lee *et al.* (*128*), who introduced non-uniform rational B-spline (NURBS) surface and polygon mesh models for organs and tissues. Also, trabecular bone images were acquired with micro-CT, which provides a better image resolution than micro-MRI. Pafundi's model is composed of 20 skeletal sites, Hough's model of 38 skeletal sites, and O'Reilly's model of 37 skeletal sites. In these models, the thickness of endosteum (or shallow marrow) was redefined as 50 μm based on

the recommendations of ICRP publication 110 (*122*). Also, these models were restricted to electron sources.

Chapter III
Methods

1. Quantification of the Fat Volume Fraction in Lumbar Vertebrae

This section is dedicated to describing the validation and implementation of a method to quantify the volume fraction of fat in lumbar vertebrae using a commercially available MRI technique. The first step was the preparation of a validation phantom and, subsequently, the measurement of the fat volume fraction using MRS and MRI. The second step was the measurement of the fat volume fraction in three healthy volunteers using MRS and MRI. The last step was a retrospective study, which consisted of the quantification of the fat volume fraction in a group of 46 sequentially scanned patients.

A 3T MRI clinical scanner (MAGNETOM Prisma, Siemens Healthineers) with a 32-channel coil array for signal reception was used to perform all MRI and MRS acquisitions presented in this study (*8*).

The image processing package Fiji (version ImageJ 1.51g) (*134,135*) was used for analyzing the MRI data. The software package AMARES (jMRUI version 5.2) (*136,137*) was used for processing and analyzing the MRS data. Lastly, the software R (Version 3.3.2) (*138*) was used to perform statistical computations (*8*). All plots were made in R (version 3.6.1).

All volunteers and patients gave written informed consent for the recording and anonymized analysis of their data. The local ethics committee waived the need for further approval.

1.1. Validation Phantom

Following the methodology proposed by Hines et al. (*139*), a phantom was constructed to test the accuracy of the MRI and MRS techniques. The phantom was composed of eleven vials of 50 ml each. They were filled with different proportions of agar (water equivalent medium) and peanut oil (fat medium), to obtain homogeneous mixtures with fat volume fraction between 0.0 and 1.0, with increments of 0.1 of the fat volume fraction. Agar and peanut oil were selected because they present a comparable proton nuclear magnetic resonance spectrum to human soft tissue and adipose tissue (*140*). All mixtures except one filled with only distilled water were doped with 0.49mM of gadolinium (Gadobutrol, Bayer Schering Pharma, Germany) to shift the relaxation time of agar into the range of human soft tissue. For peanut oil, a density of 0.91 g/cm^3 was assumed for calculating the nominal fat volume fraction. In comparison to the work of Hines *et al.* (*139*), we did not dope the solution with iron, which was

used by Hines *et al.* to simulate iron overload in the human liver. Lastly, all the vials were submerged in a water tank and submitted to MRS and MRI techniques (*8*).

1.2. Quantification of the Fat Volume Fraction in the Validation Phantom Using MRS and MRI

MRS was performed by using a PRESS pulse sequence. This single voxel spectroscopy technique was performed in each vial with the following parameter: Excited volume: 15 mm × 15 mm × 15 mm, TR = 5000 ms, TE = 33 ms, 10 averages, flip angle: 90°, no water suppression, bandwidth 1200 Hz. The MRS (PRESS sequence) was considered the gold standard for the quantification of the fat volume fraction (*8*).

Immediately after the MRS, the MRI scan was performed using a clinical two-point Dixon sequence in combination with a 3D gradient echo based sequence (VIBE: volumetric interpolated breath-hold examination) with parallel imaging acceleration (CAIPIRINHA: controlled aliasing in parallel imaging results in higher acceleration). The acquisition parameters were: TR = 5.36 ms, TE = 2.46 ms, flip angle: 9°, voxel size: 1.25 mm × 1.25 mm × 2 mm, volume: 325 mm × 400 mm × 240 mm, total acquisition time: 20.1 s (*8*). Figure 1 shows the three images obtained with the Dixon sequence: A) fat, B) water, and C) fat volume fraction. Also, it shows the arrangement of the calibration samples.

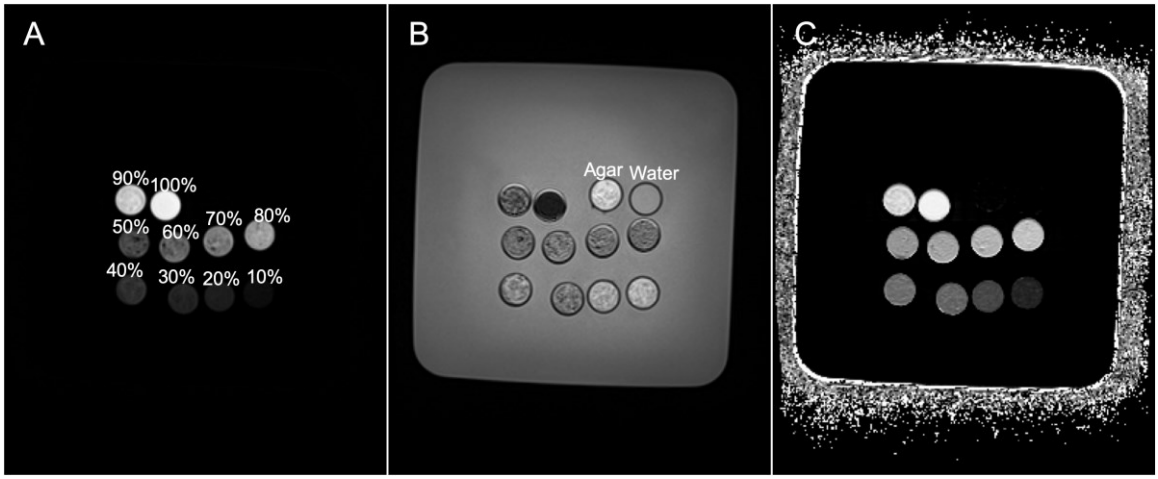

Figure 1. MRI of the validation phantom.
A: Fat image. B: Water image. C: Fat volume fraction image. Figure modified from (*8*).

The fat volume fraction was calculated for each vial and each magnetic resonance technique (MRI and MRS) by applying equation 13. In case of MRI, 20 regions-of-interest (ROIs) in adjacent slices located in the center of each vial were selected. Lastly, an average value with its respective standard deviation was calculated for each vial. The spectra obtained with the PRESS pulse sequence were analyzed using a two-peak approach (only the area

under the methylene [-$(CH_2)_n$-] and the water peak were quantified). Then, equation 8 was applied. Furthermore, for vials with 0.8 and 0.9 fat volume fraction, it was necessary to segment the olefinic fats (-HC=CH-) peak. Therefore, only for these two vials, the water and olefinic fats (-HC=CH-) peaks were separated (*8*).

The values of the nominal fat volume fraction of the phantom (VF_{F_0}), the MRS-based fat volume fraction (VF_{F_MRS}), and the MRI-based fat volume fraction (VF_{F_MRI}) were analyzed in pairs by linear regression and Bland-Altman plots (*8*).

1.3. Quantification of the Fat Volume Fraction in 3 Healthy Volunteers Using MRS and MRI

The accuracy of the MRI-based quantification was tested in 3 healthy volunteers (volunteer 1: 60 year-old male, volunteer 2: 31 years-old male, volunteer 3: 28 years-old female). In this section, the MRS (PRESS sequence) was considered the gold standard for the quantification of the fat volume fraction (*8*).

Following the same approach as for the quantification of the fat volume fraction in the validation phantom, the PRESS sequence was applied separately in each lumbar vertebra by placing a single voxel (excited MRS volume) in the center of each vertebra. Then, an MRI acquisition in sagittal orientation was performed in the anatomical region covering all lumbar vertebrae. Two-point Dixon and PRESS sequence parameters were chosen according to the phantom study. In volunteer 3, due to a suboptimal coil positioning, both MRS and MRI were applied between thoracic vertebra 12 and lumbar vertebra 4. The excited MRS volume in volunteers 1 and 2 was 15 mm × 15 mm × 15 mm. Volunteer 3 presented smaller vertebral bodies than volunteers 1 and 2. Therefore, the excited MRS volume was reduced to 10 mm × 10 mm × 10 mm (*8*).

The excited MRS volumes were reproduced in MRI to compare MRS and MRI. In the first step, the reconstruction orientation of all images was changed from sagittal to axial orientation. The second step, cubic volumes-of-interest (VOI_{Cube}) with a size close or equal to the excited MRS volume, were placed in the center of each vertebral body. Due to the MRI voxel size (1.25 mm × 1.25 mm × 2.00 mm) in volunteers 1 and 2, the VOI_{Cube} was fixed with a size of 15 mm × 15 mm × 16 mm. In volunteer 3, the size was fixed as in the MRS (10 mm × 10 mm × 10 mm) (*8*).

The last step was performed to determine the difference between a single voxel quantification (MRS) and a whole vertebral body quantification of the fat volume fraction. For this purpose, a volume-of-interest was drawn, which includes the whole vertebral body ($VOI_{Contour}$) (*8*). Figure 2 exemplifies the axial ROIs that define VOI_{Cube} and $VOI_{Contour}$.

The data pairs (VF_{F_MRI} and FVF_{F_MRS}) of 15 vertebrae were analyzed statistically by using the Shapiro-Wilk test (test of normality), followed by Wilcoxon-Pratt signed-rank test (paired difference test for not normally distributed data). Lastly, the differences between both methodologies were evaluated by Bland-Altman plots (*8*).

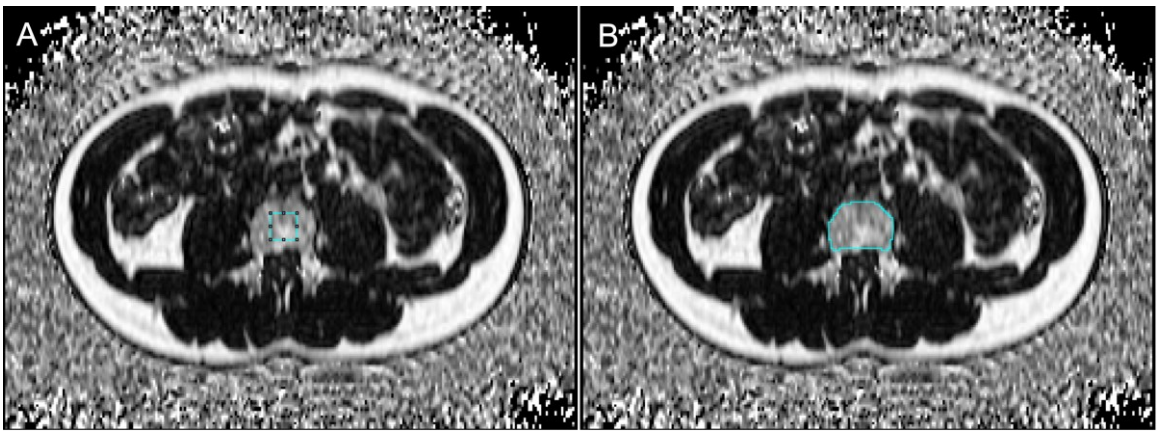

Figure 2. Example of the ROI drawn using Fiji (ImageJ) to define:
A: VOI_{Cube}. B: $VOI_{Contour}$.
Both images show lumbar vertebra 3 in volunteer 2. Figure 2B modified from (*8*).

1.4. Retrospective Quantification of the Fat Volume Fraction in 46 Sequentially Scanned Patients Using MRI

For the selection of MRI, patient data, three inclusion criteria were defined (*8*):

i) Images were acquired in the same MR system used in the previous sections of this study.

ii) All lumbar vertebrae were included in the imaging volume.

iii) No medical record of external radiation therapy applied in the lumbar vertebrae region.

The imaging volumes and voxel sizes were adjusted to each patient's dimensions, in concordance with the clinical protocol (*8*).

All volumes-of-interest were drawn considering only the vertebral body, as was described in the volunteer study. Figure 2B exemplifies the axial VOI segmentation. For each patient vertebra, an average fat volume fraction with the corresponding standard deviation was calculated. Also, five lumbar vertebrae average fat volume fractions and the corresponding standard deviation were calculated. In both cases, the quantified fat volume fraction was separated into two groups (males and females). Then, each group data was correlated with age and analyzed by linear regression. Furthermore, the predictive power of both linear models was tested by calculating the predicted R-squared values. Lastly, the data were binned into

age spans of ten years and analyzed statistically by a paired t-test applied to each bin to compare both groups (males and females) (*8*).

2. Quantification of the Bone Volume Fraction

This section is dedicated to describing the validation and implementation of a method to quantify the bone volume fraction in lumbar vertebrae using a SPECT/CT system. The first step was the preparation of a validation phantom and subsequently the measurement of the mineral bone volume fraction using a DEQCT method (*22*) implemented for a SPECT/CT and a dual-source CT (DSCT). The second step was a set of measurements in an anthropomorphic phantom, specifically the European spine phantom (ESP), using dual-energy X-ray absorptiometry (DEXA) and the previously validated DEQCT method. The last step was the quantification of the bone mineral volume fraction and total bone volume fraction in a patient dataset. The patient gave written informed consent for the recording and anonymized analysis of their data. The local ethics committee waived the need for further approval.

A DEQCT method (*22*) was implemented for two CT systems: i) the CT of a SPECT/CT system (Symbia Intevo Bold, Siemens Healthineers) with three available CT voltages (80 kV, 110 kV, and 130 kV), and ii) a dedicated DSCT system (SOMATOM Force, Siemens Healthineers). All CT images used in this section were acquired with one of these two systems. DEXA images were acquired with a Lunar Prodigy Advance DEXA system (GE Healthcare) (*12*).

For quantifying CT images, the image processing package Fiji (version ImageJ 1.51g) (*134,135*) was used. The Segment Editor Tool of 3D Slicer (version 4.8.1) (*141,142*) was used to process the CT images of the Model 062M electron density phantom (computerized imaging reference systems, CIRS) and the European Spine Phantom (*143*). All statistical calculations were performed in R (version 3.5.1) (*12,138*). All plots were made in R (version 3.6.1).

2.1. DEQCT Method

The DEQCT method used in this study was proposed by Liu *et al.* (*22*). This method is a material decomposition method based on spectral X-ray attenuation. It requires as primary input the X-ray tube spectra (high and low energy), the detector sensitivity function, and two CT images (high and low voltage). The method provides the mass fraction of the components of a composition of (two or three materials) (*12*).

To implement this method in both CT system, the manufacturer provides the following information (*12*):

- SPECT/CT:
    - Filter arrangement of the X-ray source.
    - Bowtie filter attenuation profiles for 80 kV, 100 kV, and 130 kV.

- DSCT:
    - Isocenter X-ray tube spectra for 80 kV, 120 kV, and 150 kV (with and without Sn filter).

Based on this information, the X-ray spectra for the SPECT/CT system (80kV and 130 kV) were generated using the Siemens online tool for the simulation of X-ray spectra (*144*). For the DSCT, the 90 kV spectrum was not provided. Therefore, it was generated by selecting filter thicknesses of titanium and aluminum that provided 80 kV and 120 kV spectra with the smallest difference (*12*).

Due to the lack of the specific detector sensitivity function of each CT system, they had to be extracted from Liu *et al.* (*22*). This decision was made based on the fact that both CT systems use GdOS (Gadolinium Oxysulfide) scintillator detectors. The lack of this specific information was compensated by the introduction of an empirical constant (K) (*12*).

CT imaging is based on the use of continuous X-ray sources (multiple energy photons). Therefore, it is necessary to calculate for each energy spectrum (low and high X-ray potential):

- The effective attenuation coefficients of the materials to be quantified.
- The effective mass attenuation coefficients of the elements with an atomic number between 1 and 30.

Based on this information and the quantification of the mean (HU) of the material to be decomposed, it is possible to create lookup tables to determine:

- The effective atomic number of the material to be decomposed.
- The effective density of the material to be decomposed.
- The mass fraction of the components of the material to be decomposed.

The necessary steps to implement Liu *et al*. (*22*) DEQCT method are presented below:

1. Calculation of a weighting function for both energy spectra (low and high energy) (*12,94*):

$$w_{E_{1,2}}(E) = \frac{S(E)D(E)}{\int_{E=\,0\,keV}^{E=E_{1,2}} S(E)D(E)dE} \qquad \text{equation 25}$$

   Here, $S(E)$ is the X-ray tube spectrum, $D(E)$ is the detector sensitivity function, and $E_{1,2}$ are the low and high acquisition energies of the CT system.

2. Calculation of the effective mass attenuation coefficient, $\mu_{m,E_{1,2},X}(Z_{eff})$, of the three materials to be quantified for each energy spectrum (*12,94*):

$$\mu_{m,eff,E_{1,2},X}(Z_{eff}) = \int_{E=\,0\,keV}^{E=E_{1,2}} w_{E_{1,2}}(E)\mu_{m,X}(E, Z_{eff,X})dE \qquad \text{equation 26}$$

Here, $\mu_{m,X}(E,Z)$ is the mass attenuation coefficient of the material (X) to be quantified with atomic number, $Z_{eff,X}$, and energy, E. The material to be quantified are i) in a patient: soft tissue, adipose tissue, and cortical bone. The chemical element composition of these materials was obtained from Report 44 of the International Commission on Radiation Units and Measurements (ICRU) (*34*). ii) In phantom samples: water, adipose tissue (as in ICRU Report 44), and hydroxyapatite, the chemical element composition of water and hydroxyapatite can be found in Table 9 of Appendix 2: Bone Volume Fraction – Additional Tables and Figures. The values of $\mu_{m,X}(E,Z)$ were obtained from the program XMuDat (version 1.0.1) (*145*) using the chemical element composition described in ICRU Report 44 (*34*) and Table 9 of Appendix 2: Bone Volume Fraction – Additional Tables and Figures.

3. The function $f_{E_{1,2}}(Z)$ is calculated for elements with an atomic number between 1 and 30. $f_{E_{1,2}}(Z)$ is mathematically equivalent to the effective mass attenuation coefficient (as in equation 26) for each element and both energy spectra (*12,22,94*):

$$f_{E_{1,2}}(Z) = \int_{E=0\ keV}^{E=E_{1,2}} w_{E_{1,2}}(E)\mu_m(E,Z)dE = \mu_{m,E_{1,2}} \qquad \text{equation 27}$$

From this step, a table that links Z (from 1 to 30) to $f_{E_1}(Z)$ (or $f_{E_2}(Z)$) is created.

4. Construction of a lookup table which links the atomic number of each element with the fraction of its effective attenuation coefficients (*12,22,94*):

$$F(Z) = \frac{\mu_{m,E_1}}{\mu_{m,E_2}} = \frac{f_{E_1}(Z)}{f_{E_2}(Z)} \rightarrow Z = F^{-1}\left(\frac{\mu_{m,E_1}}{\mu_{m,E_2}}\right) \qquad \text{equation 28}$$

From this step, a table that links Z (from 1 to 30) to $F(Z)$ is created.

5. In the CT images (low and high voltage), the average HU of each material to be decomposed is obtained in a volume-of-interest (VOI) analysis. These HU are transformed into $\mu_{eff,E_{1,2}}$ by using the effective mass attenuation coefficient of water, $\mu_{m,E_{1,2},Water}$, obtained from equation 26, assuming a water density equal to 1 g/cm^3 (*12*):

$$\mu_{eff,E_{1,2}} = \frac{\mu_{E_{1,2},Water} \cdot HU}{1000} + \mu_{E_{1,2},Water} \qquad \text{equation 29}$$

6. Then, the function $F(Z)$ for the material to be decomposed is calculated for $\mu_{eff,E_{1,2}}$ (*12,22,94*):

$$F(Z) = \frac{\mu_{eff,E_1}}{\mu_{eff,E_2}} \qquad \text{equation 30}$$

7. From the value of $F(Z)$ in equation 30 and by interpolation of the values of the lookup table from step 4, it is possible to obtain the effective atomic number (Z_{eff}) in the VOI (material to be decomposed):

$$Z_{eff} = F^{-1}\left(\frac{\mu_{eff,E_1}}{\mu_{eff,E_2}}\right) \qquad \text{equation 31}$$

8. The value of $f_{E_1}(Z_{eff})$ is calculated by interpolation of the values in the lookup table of step 3. Then, the lookup-table effective density, $\rho_{eff,lookup-table}$, of the material to be decomposed is determined (*12,22,94*):

$$\rho_{eff,lookup-table} = \frac{\mu_{eff,E_1}}{f_{E_1}(Z_{eff})} \qquad \text{equation 32}$$

9. By using the effective density, atomic effective number, and the effective attenuation coefficients of the three materials to be quantified and following the methodology proposed by Liu *et al*. (*22*), it is possible to obtain the mass fractions (MF) of each quantified material by solving the following equation system (*12,22*):

$$\mu_{eff,E_1} = C^2 \cdot K \cdot \rho_{eff,lookup-table} \int_{E=0\ keV}^{E=E_1} w_{E_1}(E)[MF_1 \cdot \mu_{m,E_1,1}(E) + MF_2 \cdot \mu_{m,E_1,2}(E) + (1 - MF_1 - MF_2) \cdot \mu_{m,E_1,3}(E)]\, dE \qquad \text{equation 33}$$

$$\mu_{eff,E_2} = C^2 \cdot K \cdot \rho_{eff,lookup-table} \int_{E=0\ keV}^{E=E_2} w_{E_2}(E)[MF_1 \cdot \mu_{m,E_2,1}(E) + MF_2 \cdot \mu_{m,E_2,2}(E) + (1 - MF_1 - MF_2) \cdot \mu_{m,E_2,3}(E)]\, dE \qquad \text{equation 34}$$

$$1 = MF_1 + MF_2 + MF_3 \qquad \text{equation 35}$$

Here, MF_1, MF_2, and MF_3 are the mass fractions of the quantified materials (e.g., hydroxyapatite, fat or adipose tissue, and water or soft tissue). C is an empirical correction factor documented by Liu *et al.* (*22*) and Azevedo et al. (*146*) to correct the effective density based on the effective atomic number. The constant K corrects for the lack of specific information on the X-ray tube spectrum or detector sensitivity function. An example for the determination of C and K can be found in Appendix 3: Bone Volume Fraction – Calculation of Empirical Correction Factors.

10. The volume fraction of the decomposed material is quantified by the conversion of the mass fraction (MF) values into volume fraction (VF_{HA}) using the following equation (*12*):

$$VF_X = \frac{\rho_{eff} \cdot MF_X}{\rho_X} = \frac{C \cdot K \cdot \rho_{eff,lookup-table} \cdot MF_X}{\rho_X} \qquad \text{equation 36}$$

Here, ρ_X corresponds to the density of material (X) to be quantified.

2.2. Phantom 1: Validation Phantom

The accuracy of the DEQCT method (*22*) implemented in this study was validated in a custom-made phantom. The phantom was composed of eight vials of 50ml each. Three of them were filled with a mixture of 50% water and 50% Poly(2-hydroxyethyl methacrylate) (pHEMA) plus hydroxyapatite at three different concentrations (100 mg/cm^3, 200 mg/cm^3, 300 mg/cm^3). The formation of hydroxyapatite in a water-pHEMA medium is produced by hydrolysis in situ of the alpha-tricalcium phosphate (α-TCP) (*147*). The α-TCP preparation was performed, according to Christel *et al.* (*147*). The hydroxyapatite volume fraction (VF_{HA}) in the three vials was 0.033, 0.067, and 0.100 based on a hydroxyapatite density equal to 3,000 mg/cm^3 (*12*).

Two more vials were filled with the same mixture of agar, paraffin, and hydroxyapatite. The respective volume fractions were 0.05 hydroxyapatite, 0.475 fat, and 0.475 water. In the first step, a 50% agar and 50% paraffin (viscous) mixture was prepared following the methodology proposed by Hines *et al.* (*139*). Then, this mixture was, in turn, mixed with a 150 mg/cm^3 concentration of hydroxyapatite (calcium phosphate tribasic, Thermo Fisher GmbH). Our preparation methodology differs from Hines *et al.* (*139*) in that i) paraffin was used instead of peanut oil, and ii) no gadolinium or iron had to be added (*12*).

The last three vials were filled with distilled water, pure paraffin, and pure agar. All vials were attached to a 3D-printed insert, which was placed inside of a water-filled NEMA phantom

to simulate the soft-tissue attenuation. Figure 3 shows an axial view of the distribution of vials inside the NEMA phantom (*12*).

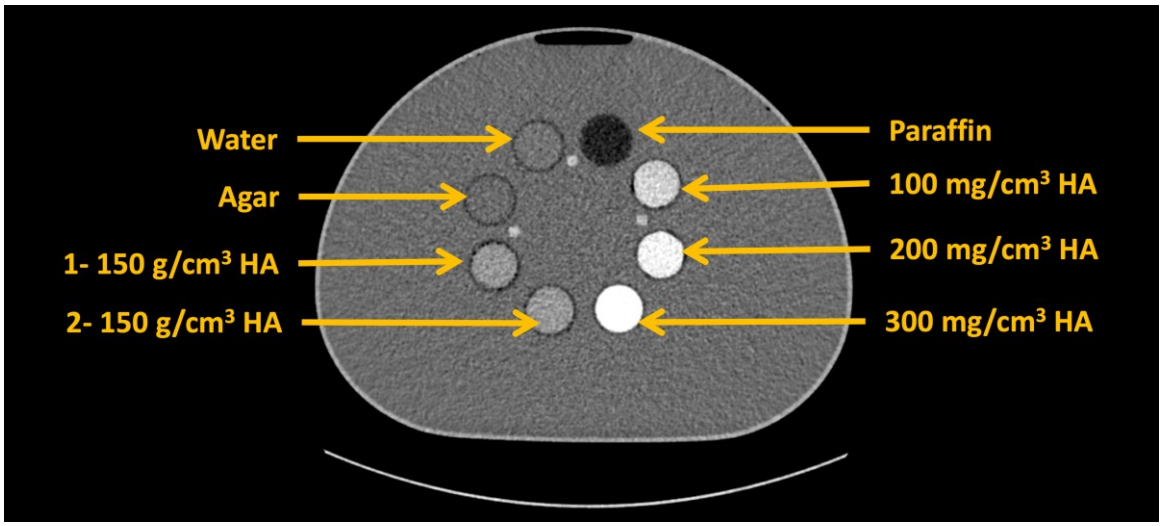

Figure 3. Axial view of the validation phantom.
Set of vials submerged in a water-filled NEMA phantom. Figure modified from (*12*).
Acquisition parameters are specified in table 1.

2.3. Phantom 2: European Spine Phantom

The European Spine Phantom (ESP) (*143*) provides an anthropomorphic geometry of three lumbar vertebrae. The dimensions of the ESP are 25 cm lateral, 18 cm anterior-posterior, and 12 cm axial (*143*). The ESP simulates the lumbar region of a patient torso. Also, it consists of three vertebrae, each one with a different distribution of hydroxyapatite (mineral bone) in each of its three compartments: i) spongiosa, ii) wall and endplate, and iii) arch and processes (see Figure 4A) (*143*). The bone mineral content (BMC_{ESP}) excluding the vertebral processes in a projected area of 900 mm^2 (see red box in Figure 4A) is documented for each vertebra as 4.5 g, 9.0 g, and 13.5 g of hydroxyapatite (HA) (*143*). Due to the lack of information related to the volume of the whole vertebra, it was not possible to calculate the nominal values of the bone mineral volume fraction for the whole vertebrae. Therefore, the experiment performed in this study was to determine the bone mineral content experimentally and compare these values with the nominal bone mineral content (12). Section 2.6.1 explains in detail the procedure related to the quantification of the bone mineral content.

Additionally, the bone mineral density (BMD_{ESP}) in the spongiosa region of the ESP is documented for each vertebra as 50 mg/cm^3, 100 mg/cm^3, and 200 mg/cm^3 of HA (*143*). Therefore, for the spongiosa region, it is possible to calculate the hydroxyapatite volume fraction by dividing the bone mineral density by the hydroxyapatite density (3000 mg/cm^3).

Then, the hydroxyapatite volume fraction (VF_{HA}) in the spongiosa region of the vertebrae is 0.017, 0.033, and 0.067.

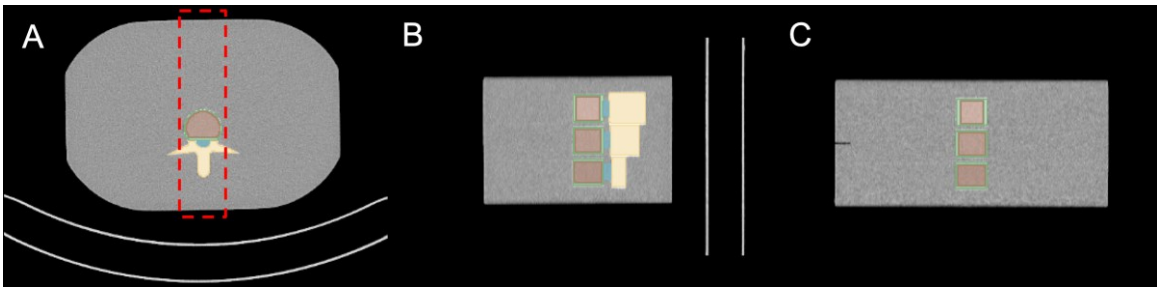

Figure 4. Views of the European Spine Phantom.
A: Axial. B: Sagittal. C: Coronal.
Compartments: i) spongiosa (red), ii) wall and endplate (green), and iii) arch and processes (yellow).

2.4. Phantom Acquisition Parameters

All phantom images were acquired as follows: In case of the DSCT, low and high voltage CT datasets were acquired simultaneously following the clinical protocol for multiple myeloma. Subsequently, image sets were reconstructed separately from both datasets using two kernels (Qr40 and Br59) based on the clinical protocol for multiple myeloma (*12*). The acquisition parameters are specified in Table 1.

In case of the SPECT/CT, low and high voltage CT datasets were acquired separately (one after the other) using an abdominal imaging protocol. They were both reconstructed using the I41s kernel (*12*). The acquisition parameters are specified in Table 1

Table 1. Phantom acquisition parameters for both CT systems

CT System	Voltage (kV)	Tube Current-Exposure Time Product (mAs)	Collimation (mm)	Pitch	Slice thickness (mm)	$CTDI_{vol}$ (mGy)[a]
DSCT	80	158	64 x 0.6	0.6	1	3.23
	150	90				2.79
	90	130	64 x 0.6	0.6	1	4
	150	90				2.82
SPECT/CT	80	70	16 x 0.6	0.6	1	2.39
	130	53				6.39

[a] From the validation phantom
Table modified from (*12*)

2.5. Analysis of the Validation Phantom

In this section, the procedure for quantifying the hydroxyapatite volume fraction in the vials of the validation phantom by using the DEQCT method (see section 2.1, Chapter III) is presented. Each vial of the validation phantom was segmented by defining a circular ROI with a 14.1 mm diameter for the SPECT/CT datasets (15.2 mm for the DSCT datasets). Then, a mean HU was quantified as average over 34 slices analyzed in the SPECT/CT datasets (29 slices for the DSCT datasets). Next, the hydroxyapatite mass fraction was calculated using the DEQCT method. Subsequently, the hydroxyapatite volume fraction was calculated using equation 36 to obtain VF_{HA_DSCT} (or $VF_{HA_SPECT/CT}$).

In all the measurements performed on the ESP, a material composition of hydroxyapatite, water, and adipose tissue was assumed (*12*). Also, considering that the water-pHEMA vials are composed only of hydroxyapatite and a water equivalent material, the fat mass fraction was fixed at zero in equation 35 (*12*). Furthermore, the obtained values of VF_{HA_DSCT} (or $VF_{HA_SPECT/CT}$) were compared with the nominal values (VF_{HA_0}). Lastly, the hydroxyapatite volume fraction in the two samples composed of hydroxyapatite, paraffin, and agar was quantified following the same procedure (*12*). All data on the quantification of the VF_{HA} are displayed in *Figure 11* as Bland-Altman plots.

2.6. Analysis of the European Spine Phantom

2.6.1. Quantification of the Bone Mineral Content using DEXA, DSCT and SPECT/CT in the Whole Vertebra of the European Spine Phantom

Quantification with DEXA (*12*)*:* Ten measurements of the ESP (*143*) were performed in an anterior-posterior position using the clinical protocol for lumbar vertebrae. This protocol performs an automatic selection of the quantification area (DEXA-ROI). Subsequently, the bone mineral area densities (BMD_{DEXA}) were extracted from the DEXA report. Lastly, BMC_{DEXA} was calculated by multiplying the BMD_{DEXA} with the area of the DEXA-ROI.

Quantification with CT (*12*)*:* This section describes the procedure to quantify the bone mineral content in the ESP by using the DEQCT method (see section 2.1, Chapter III). In the first step, images of the ESP (*143*) were acquired in both CT systems (SPECT/CT and DSCT). Each vertebra was segmented by defining a VOI, which excluded the transverse processes to adjust the quantification volume to the DEXA automatic quantification area selection. Then, a mean HU was quantified for each segmented volume. Next, the hydroxyapatite mass fraction was calculated using the DEQCT method. Subsequently, the hydroxyapatite volume fraction was calculated using equation 36 to obtain VF_{HA_DSCT} (or $VF_{HA_SPECT/CT}$), and the result was multiplied with the nominal hydroxyapatite density (3,000 mg/cm^3) to obtain BMD_{DSCT} (or

$BMD_{SPECT/CT}$). Lastly, to obtain BMC_{DSCT} (or $BMC_{SPECT/CT}$), the BMD_{DSCT} (or $BMD_{SPECT/CT}$) was multiplied with the volume of the VOI (*12*). In all the measurements performed on the ESP, a material composition of hydroxyapatite, water, and adipose tissue was assumed. Also, considering that the vertebrae are composed only of hydroxyapatite and a water equivalent material, the fat mass fraction was fixed at zero in equation 35.

For all imaging systems, the quantified BMC values (BMC_{DEXA}, BMC_{DSCT}, and $BMC_{SPECT/CT}$) were compared with the nominal values of the ESP (BMC_{ESP}) by calculating the relative error considering BMC_{ESP} as reference values. Also, Bland-Altman plots were prepared between BMC_{DSCT} (or $BMC_{SPECT/CT}$) and BMC_{ESP} (*12*).

2.6.2. Quantification of the Hydroxyapatite Volume Fraction using DSCT and SPECT/CT in the Spongiosa Region of the European Spine Phantom

In this section, the procedure to quantify the hydroxyapatite volume fraction in the spongiosa region of the ESP by using the DEQCT method (see section 2.1, Chapter III) is presented. In a first step, the spongiosa region of each vertebra of the ESP (*143*) was segmented in each of the acquired images by defining a VOI. Subsequently, the mean HU in each VOI was measured. Then, the DEQCT method was applied, and the hydroxyapatite mass fraction was calculated. Subsequently, the hydroxyapatite volume fraction was calculated using equation 36 to obtain VF_{HA_DSCT} (or $VF_{HA_SPECT/CT}$). In all the measurements performed on the ESP, a material composition of hydroxyapatite, water, and adipose tissue was assumed. Also, considering that the spongiosa regions of the ESP are composed only of hydroxyapatite and a water equivalent material, the fat mass fraction was fixed at zero in equation 35 (*12*).

For both imaging systems, the quantified VF_{HA} (VF_{HA_DSCT} and $VF_{HA_SPECT/CT}$) were compared with the nominal values of the ESP (VF_{HA_ESP}) by calculating the relative error considering VF_{HA_ESP} as reference value. Also, Bland-Altman plots were prepared between VF_{HA_DSCT} (or $VF_{HA_SPECT/CT}$) and VF_{HA_ESP}.

2.7. Analysis of a Patient Dataset

The DEQCT method depends on the chemical element composition of the material to be quantified. In all phantom experiments, the mineral bone volume fraction or the hydroxyapatite volume fraction were quantified. Considering that human bone is composed of mineral bone and organic material (*1*), two methodologies to quantify the bone volume fraction are presented in this section (*12*).

First, a patient for which a DEXA as well as a DSCT study had been previously performed in our institution was retrospectively selected. The difference in time between DEXA and DSCT imaging was one week without any invasive procedure being performed in between;

therefore, no anatomical changes were expected. The DEXA study corresponded to a lumbar vertebrae (1 to 4) study. The patient was referred to a DSCT scan for the diagnostics of acute pulmonary embolism. The DSCT images covered the thorax region, including lumbar vertebrae 1 and 2. Images were acquired at 90 kV/150 kV (with Sn filter) with the following parameters (*12*): exposure: 120/63 mAs, collimation: 96×0.6 mm, slice thickness: 1.5 mm, pitch: 0.55, and reconstruction kernel: Qr40. The $CTDI_{vol}$ for the images was 3.50 mGy (90 kV) and 1.85 mGy (150 kV). Two volumes were segmented in each vertebra: i) the whole vertebra (excluding transverse processes) (see Figure 5) to compare the DEXA and DSCT quantification of the BMC. ii) The spongiosa region (see Figure 6) to quantify the bone mineral volume fraction (in the trabecular bone) and the trabecular bone volume fraction (*12*).

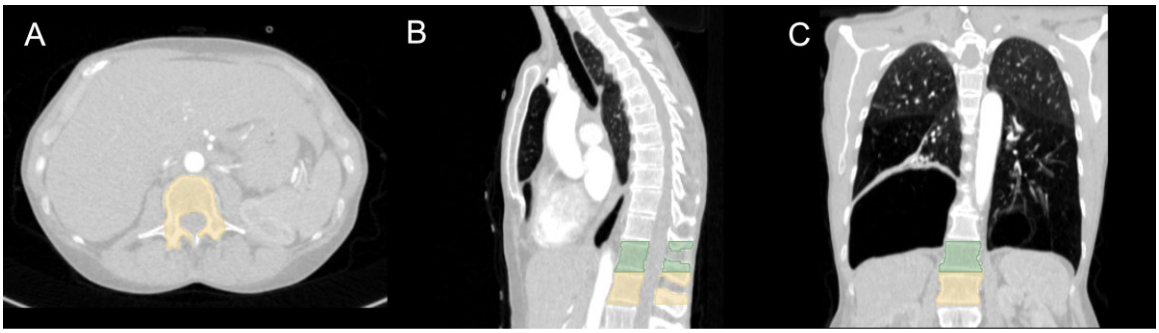

Figure 5. Segmentation of lumbar vertebrae 1 and 2 on the DSCT image.
A: Axial view. B: Sagittal view. C: Coronal view.
Reconstruction kernel: Qr40, energy: 150 kV (using Sn filter). Figure modified from (*12*).

Next, the mean HU was measured in each VOI. Subsequently, the DEQCT method was applied considering hydroxyapatite, soft tissue (*34*), and adipose tissue (*34*) as material composition. Therefore, the hydroxyapatite mass fraction, hydroxyapatite volume fraction, and bone mineral content were quantified for each VOI (*12*).

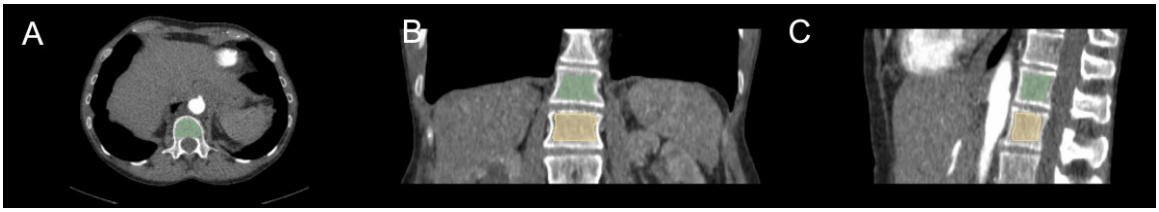

Figure 6. Segmentation of spongiosa region in lumbar vertebrae 1 and 2 on DSCT image.
A: Axial view. B: Coronal view. C: Sagittal view.
Reconstruction kernel: Qr40, energy: 150 kV (using Sn filter). Figure modified from (*12*).

Lastly, two approaches were proposed and applied to quantify the bone volume fraction (volume fraction of mineral bone plus organic material). They are explained in the following section (*12*):

2.7.1. Reference Ratio of Mineral Bone Mass Fraction to Total Bone Mass Fraction

This approach permits to calculate the bone volume fraction from the mineral bone mass fraction by using a reference ratio of the mineral bone mass fraction to the total bone mass fraction ($R_{HA/B} = MF_{HA}/MF_B$). Mathematically the bone volume fraction (VF_B) can be defined as (*12*):

$$VF_B = \frac{\rho_{eff} \times MF_B}{\rho_B} = \frac{\rho_{eff}}{\rho_B}\frac{MF_{HA}}{R_{HA/B}} \qquad \text{equation 37}$$

Here, ρ_B is the cortical bone density (1.92 g/cm^3) (*34*).

$R_{HA/B}$ can be measured experimentally by quantifying the percentages of the mass of mineral bone and organic material in bone samples. Quelch *et al.* (*148*) reported a percentage of 66.3% of mineral bone in an adult lumbar vertebrae. By using this value as reference value for $R_{HA/B}$, equation 37 takes the following form (*12*):

$$VF_B = \frac{\rho_{eff}}{\rho_B}\frac{MF_{HA}}{0.663} \qquad \text{equation 38}$$

2.7.2. Quantification Based on the Chemical Element Composition of Cortical Bone

This method is based on the use of the chemical element composition of cortical bone (*34*) instead of using the chemical element composition of hydroxyapatite to quantify the bone volume fraction (*12*). It implies that the DEQCT method is applied considering cortical bone, soft tissue, and adipose tissue as material composition, based on the element description documented by the ICRU Report 44 (*34*). The quantification of the trabecular bone volume fraction is carried out by assuming that the trabecular bone and cortical bone have the same chemical element composition (*149*).

By applying both approaches (sections 2.7.1. and 2.7.2.), the bone mass fraction and the bone volume fraction were quantified on each vertebral VOI. Also, the ratio of the mineral bone mass fraction to total bone mass fraction ($R_{HA/B} = MF_{HA}/MF_B$) was calculated for each vertebral VOI (*12*).

Chapter IV
Results

1. Quantification of the Fat Volume Fraction in Lumbar Vertebrae

1.1. Quantification of the Fat Volume Fraction in the Validation Phantom Using MRS and MRI

The linear regression analysis of the three data paired (i) VF_{F_0} and VF_{F_MRS}, ii) VF_{F_0} and VF_{F_MRI}, and iii) VF_{F_MRS} and VF_{F_MRI}) showed, in all cases, a significant positive correlation. Table 2 contains all results of the linear regression analysis. Figure 7 shows the respective plot for each data pair. The error bars in Figure 7B and Figure 7C correspond to the standard deviation of the 20 ROIs measured in each vial (*8*). An analysis of the data distribution with the Shapiro–Wilk normality test showed that the data are normally distributed. Therefore, in Table 2, the correlation coefficient was determined using Pearson's product-moment correlation test (*8*).

Table 2. Linear fit parameters for each data pair obtained from the validation phantom using MRS and MRI

Data Pair	Slope (VF_{F_Y}/ VF_{F_X})	Slope Standard Error (VF_{F_Y}/ VF_{F_X})	Intercept (VF_{F_Y})	Intercept Standard Error (VF_{F_Y})	Correlation Coefficient (r)	p-value
i	1.002	0.019	−0.004	0.011	0.998†	< 0.001
ii	0.879	0.039	0.075	0.023	0.991†	< 0.001
iii	0.877	0.035	0.079	0.020	0.993†	< 0.001

† Pearson's product-moment correlation test
VF_F = fat volume fraction
X and Y are the data sources (MRI, MRS or nominal values) of the respective data pair
Table modified from (*8*)

The Bland-Altman plots for each data pair are illustrated in Figure 8. Figure 8D shows the Bland-Altman plot parameters for each data pair (i) VF_{F_0} and VF_{F_MRS}, ii) VF_{F_0} and VF_{F_MRI}, and iii) VF_{F_MRS} and VF_{F_MRI}). Based on the Bland-Altman plot parameters, it is possible to see that the three data pairs present a small bias, being the data pair 1, which presents a better agreement (the smallest interval of confidence) (*8*).

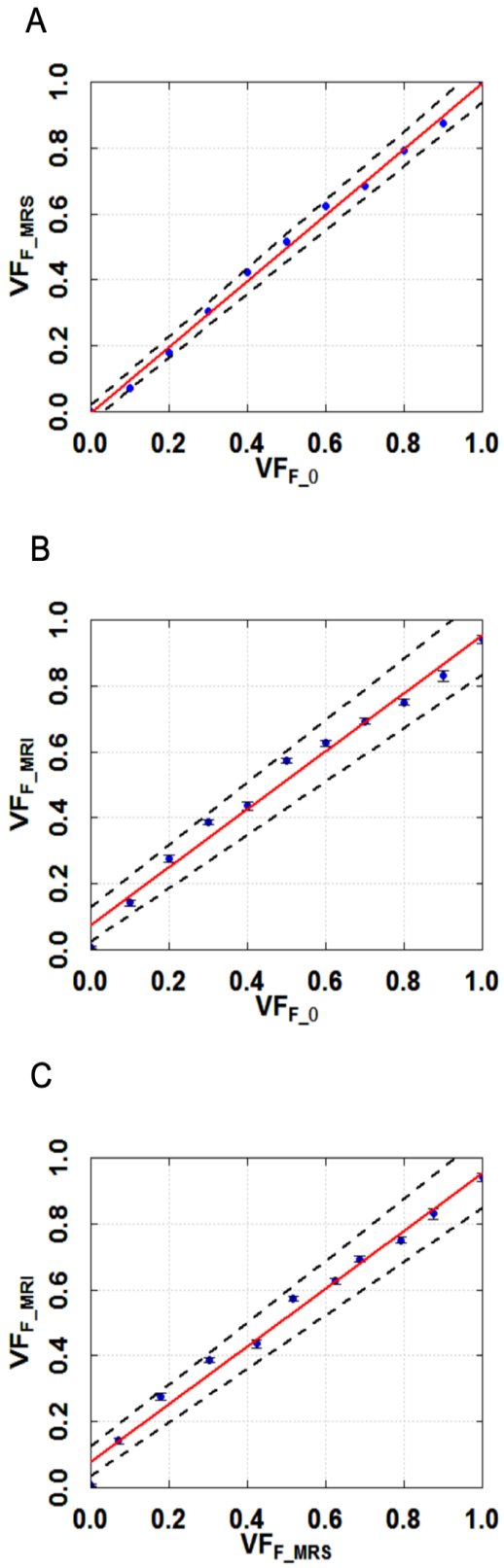

Figure 7. Linear data fit of the quantification of the fat volume fraction in the validation phantom. A: VF_{F_0} and VF_{F_MRS}. B: VF_{F_0} and VF_{F_MRI}. C: VF_{F_MRS} and F_{MRI}. Redline: linear fit. Dashed lines: 95% confidence intervals. Figure modified from (*8*).

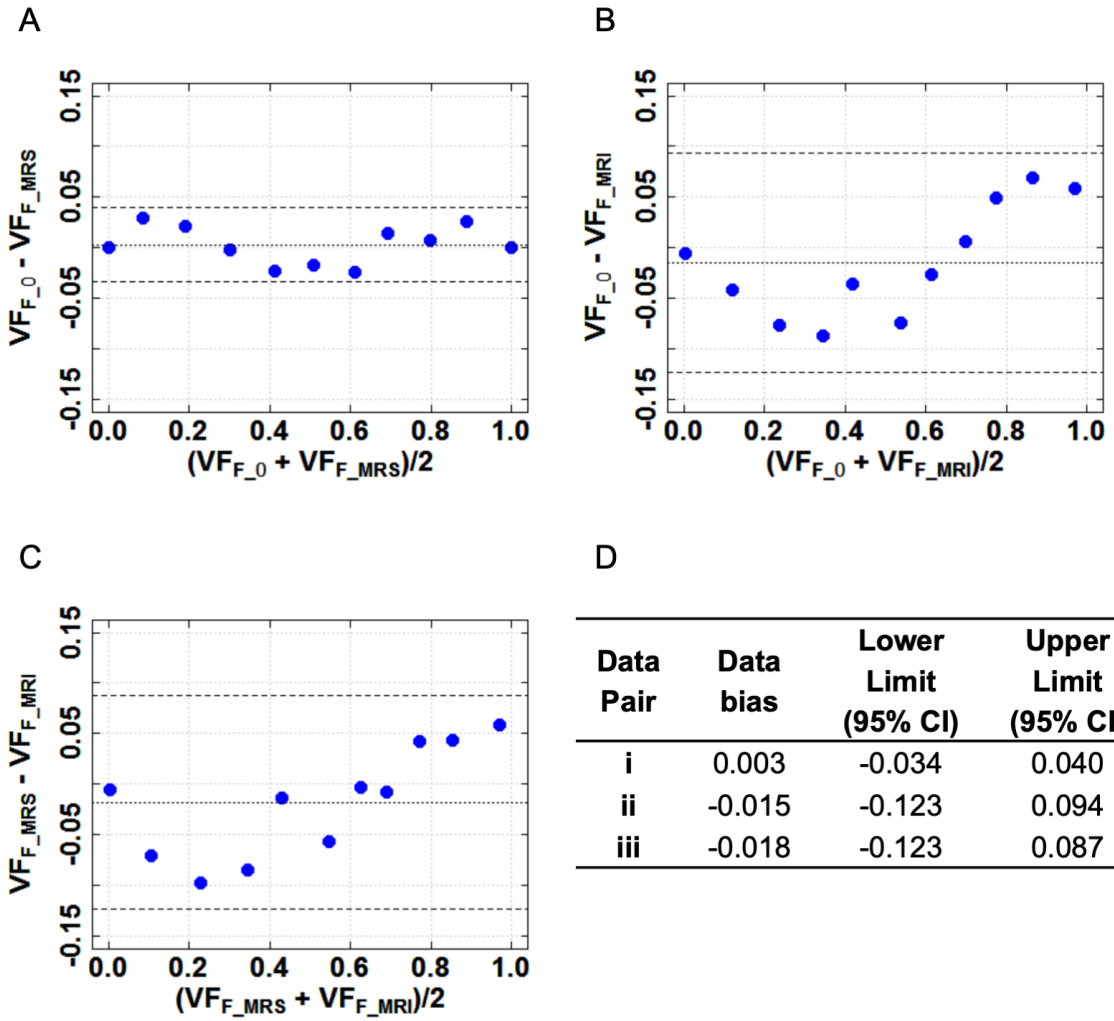

Data Pair	Data bias	Lower Limit (95% CI)	Upper Limit (95% CI)
i	0.003	-0.034	0.040
ii	-0.015	-0.123	0.094
iii	-0.018	-0.123	0.087

Figure 8. Bland-Altman plots of the quantification of the fat volume fraction in the validation phantom for each data pair.
A: VF_{F_0} and VF_{F_MRS}. B: VF_{F_0} and VF_{F_MRI}. C: VF_{F_MRS} and VF_{F_MRI}. D: Bland-Altman plot parameters. Dotted line: Data bias. Dashed lines: 95% confidence intervals. Figure modified from (*8*).

1.2. Quantification of the Fat Volume Fraction in 3 Healthy Volunteers Using MRS and MRI

Figure 9 shows the Bland-Altman plots of the MRI-based quantification and MRS-based quantification for all analyzed vertebrae (15 in total) and both VOIs (VOI_{Cube} and $VOI_{Contour}$) (*8*).

A Shapiro-Wilk test was applied to the whole dataset. As a result, the data were found to be not normally distributed. Therefore, a Wilcoxon-Pratt signed-rank test was applied. As a result, no significant difference between MRI-based and MRS-based quantification for VOI_{Cube}

(p = 0.19) was found. However, a significant difference was observed for $VOI_{Contour}$ ($p < 0.05$) (*8*).

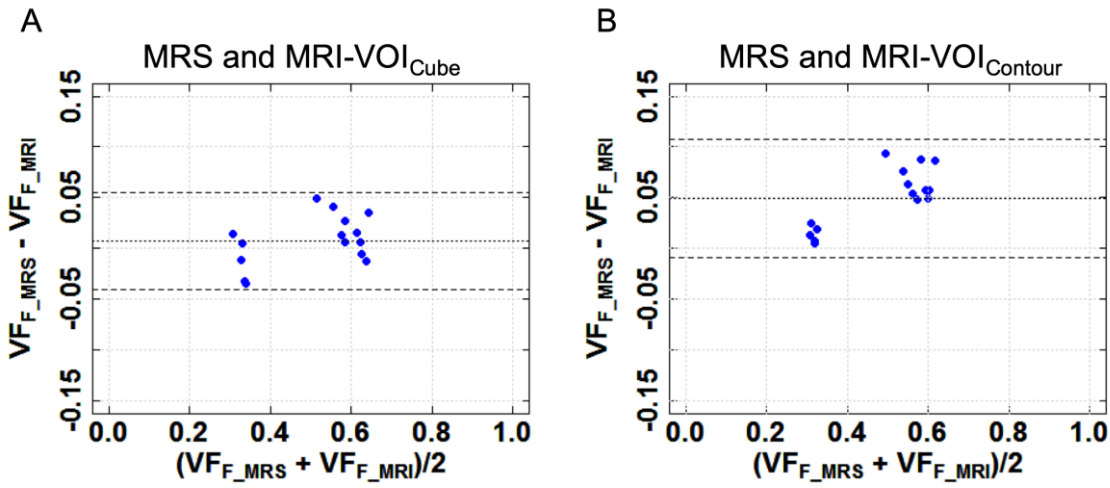

C

Data Pair	Data bias	Lower Limit (95% CI)	Upper Limit (95% CI)
MRS and MRI-VOI$_{Cube}$	0.008	-0.040	0.056
MRS and MRI-VOI$_{Contour}$	0.050	-0.009	0.108

Figure 9. Bland-Altman plots of the quantification of the fat volume fraction in volunteers. A: MRS and VOI_{Cube}-based MRI quantification. B: MRS and $VOI_{Contour}$-based MRI quantification. C: Bland-Altman plot parameters. Dotted line: Data bias. Dashed lines: 95% confidence intervals. Figure modified from (*8*).

1.3. Retrospective Quantification of the Fat Volume Fraction in 46 Sequentially Scanned Patients Using MRI

Over the course of the image analysis of the 46 patient datasets, two patient datasets had to be rejected due to poor image quality. Therefore, the retrospective study was performed in 44 patient datasets (21 female and 23 male). The age range for females was between 19 and 87 years, for males was between 23 and 85 years. The average age reported with one standard deviation for females was 54.6 ± 19.1 years, while it was 57.2 ± 19.4 years for males (*8*).

Figure 10A (females) and Figure 10B (males) show the correlation between age and fat fraction volume. Table 3 summarizes the parameters obtained from the linear regression. Based on the linear regression, a slightly higher slope (or marrow conversion rate) was

observed for females (0.5% per year) than for males (0.3% per year), and a smaller intercept for females than for males. Statistical data analysis (Shapiro-Wilk normality test) showed that the female data are normally distributed, while the male data are non-normally distributed. Therefore, the correlation for females was calculated using Pearson's product-moment correlation test, while Spearman's rank correlation rho test was applied for males (*8*).

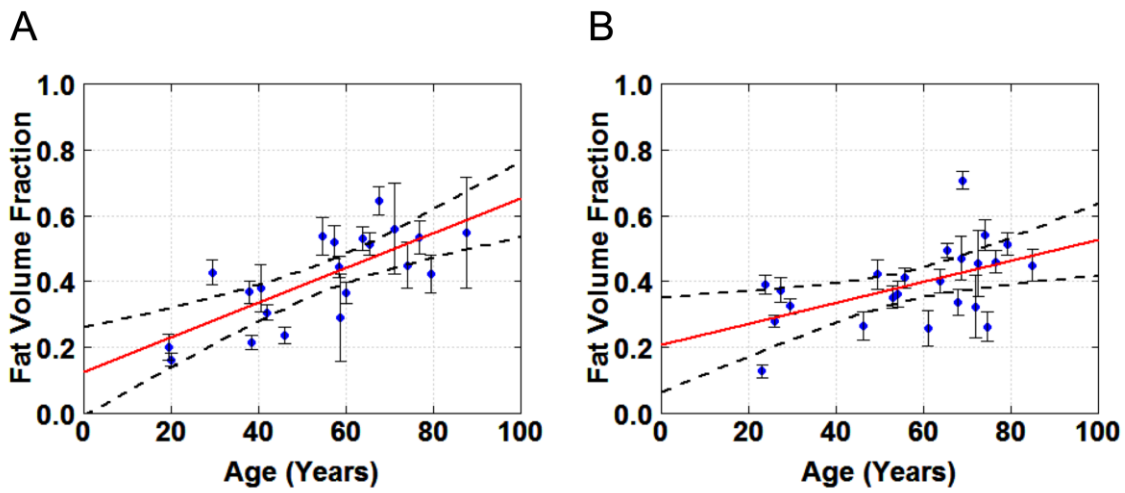

Figure 10. Linear data fit of the MRI quantification of the fat volume fraction in patient lumbar vertebrae.
A: Females. B: Males. Redline: Linear fit. Top and bottom lines (dashes) correspond to 95% confidence interval. Figure modified from (*8*).

Table 3. Linear fit parameters of the correlation between age and fat volume fraction for females and males.

Data	Slope (VF_F/ year)	Slope Standard Error (VF_F/year)	Intercept (VF_F)	Intercept Standard Error (VF_F)	Correlation Coefficient (r)	p-value
Female	0.005	0.001	0.125	0.064	0.736†	< 0.001
Male	0.003	0.001	0.207	0.069	0.529*	0.011

† Pearson's product-moment correlation test
* Spearman's rank correlation rho test
VF_F = fat volume fraction
Data were taken from (*8*)

Lastly, a paired t-test only in the age span of 40-49 years showed no significant difference ($p = 0.139$) between males and females. In other age spans, the differences were significant ($p < 0.001$). Furthermore, the analysis of the predictive power of both linear models provided predicted R-squared values of 0.12 (females) and 0.45 (males) (*8*).

Table 8 of Appendix 1: Fat Volume Fraction – Additional Tables and Figures illustrates all data and their linear regression for each lumbar vertebra individually.

2. Quantification of the Bone Volume Fraction

Five sets of images were used to quantify the bone mineral volume fraction (VF_{HA}). Four corresponded to DSCT acquisitions (combinations of two reconstruction kernels Br59 and Qr40, and two voltage arrangements 80/150 kV and 90/150 kV): Br59-80/150 kV, Qr40-80/150 kV, Br59-90/150 kV, and Qr40-90/150 kV. The fifth image set corresponded to the SPECT/CT with only one reconstruction kernel (I41s) and one voltage arrangement (80/130 kV): I41s-80/130 kV.

2.1. Quantification of the Hydroxyapatite Volume Fraction in Samples of the Validation Phantom

Figure 11 shows Bland-Altman plots, which illustrate the agreement between the nominal values of the hydroxyapatite volume fraction (VF_{HA_0}) and the image-based quantification of the hydroxyapatite volume fraction for all five CT image sets (VF_{HA_DSCT} and $VF_{HA_SPECT/CT}$). Figure 11B and Figure 11D, both corresponding to the reconstruction kernel Qr40, show the smallest interval of confidence (see Table 4). Concerning the bias, all image-based quantification show negatives values (between -0.003 VF_{HA} and -0.007 VF_{HA} see Table 4). This result indicates that the DEQCT method overestimates the hydroxyapatite volume fraction (*12*). Furthermore, it is possible to see in Figure 11A-E that the bias between the nominal value and the image-based quantification is proportional to the bone mineral content. Only the sample with a concentration of 200 mg/cm^3 of hydroxyapatite (0.067 VF_{HA}) does not follow this tendency.

Furthermore, Figure 11F shows the relative errors associated with each image-based quantification. The maximum relative error was found to be 14.15% (sample 150 mg/cm^3 of hydroxyapatite in image Br59–90/150 kV). Of all image-based quantifications, the sample with a concentration of 200 mg/cm^3 of hydroxyapatite (0.067 VF_{HA}) shows a smaller relative error than the other samples (*12*).

Lastly, the effective density (ρ_{eff}) and the effective atomic number (Z_{eff}) were calculated for each sample. All values of ρ_{eff} and Z_{eff} are listed in Table 10 of Appendix 2: Bone Volume Fraction – Additional Tables and Figures. The values obtained from the image-based quantification I41s-80/130 kV showed the best agreement with their nominal values (*12*).

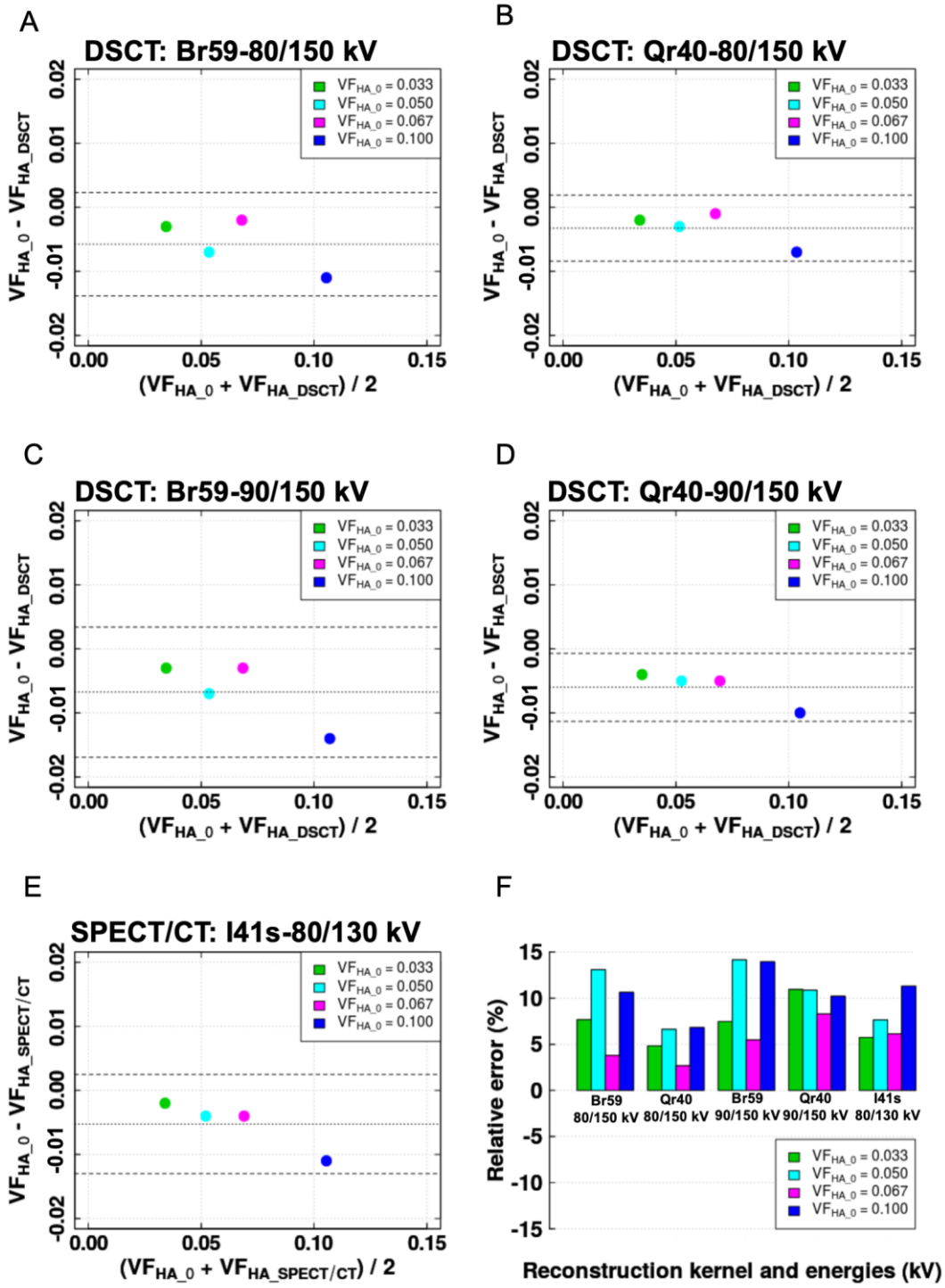

Figure 11. Bland-Altman plots of each image-based quantification.
A: Br59-80/150 kV. B: Qr40-80/150 kV. C: Br59-90/150 kV. D: Qr40-90/150 kV. E: I41s-80/130 kV. F: Relative error associated with the quantification of the hydroxyapatite volume fraction. Dotted line: mean of the differences (bias). Dashed lines: 95% confidence interval. Figure modified from (*12*).

Table 4. Data from the Bland-Altman Analysis of the Quantification of Hydroxyapatite Volume Fraction in the Validation Phantom.

Data Pair	Image-based Quantification	Bias (VF_{HA})	Lower Limit (VF_{HA})	Upper Limit (VF_{HA})
VF_{HA_0} and VF_{DSCT}	Br59-80/150 kV	−0.006	−0.014	0.002
	Qr40-80/150 kV	−0.003	−0.008	0.002
	Br59-90/150 kV	−0.007	−0.017	0.003
	Qr40-90/150 kV	−0.006	−0.011	−0.001
VF_{HA_0} and $VF_{SPECT/CT}$	I41s-80/130 kV	−0.005	−0.013	0.003

VF_{HA}: hydroxyapatite volume fraction.
Table modified from (*12*).

2.2. Quantification of the Fat, Water, and Hydroxyapatite Volume Fraction in Samples of the Validation Phantom

The quantification of fat, water, and hydroxyapatite volume fraction was not possible due to the high similarity of the calculated mass attenuation coefficient of fat and water ($\mu_{m,Fat}$ and $\mu_{m,Water}$). Therefore, the methodology does not decompose both materials (fat and water) (*12*). In all posterior quantifications, the equation system (equation 33, equation 34, and equation 35) is resolved by considering the mass fraction of fat in equation 35 as equal to zero. Consequently, the material was only decomposed into water equivalent medium (including fat) and bone (mineral or total) for the volume fraction determination in this study.

2.3. Quantification of the Bone Mineral Content in the European Spine Phantom Using DEXA, DSCT, and SPECT/CT

The same analysis applied to the validation phantom was performed for the data obtained from the quantification of the bone mineral content in the European spine phantom. Figure 12 shows Bland-Altman plots, showing the agreement between the nominal mineral bone content values of the ESP (BMC_{ESP}) and the image-based quantification of the mineral bone content for each CT image set (BMC_{DSCT} and $BMC_{SPECT/CT}$) and DEXA (BMC_{DEXA}) (*12*).

The results obtained from the Bland-Altman analysis are presented in Table 5. The Br59 DSCT images show the largest standard deviations. Figure 12B and Figure 12D, corresponding to reconstruction kernel Qr40 (DSCT), show the smallest confidence interval and bias (see Table 5). Similar results were achieved using the image-based quantification I41s-80/130 kV (SPECT/CT). Regarding the bias, all image-based quantifications show negative values (between −0.277 g of hydroxyapatite and −1.956 g of hydroxyapatite) (see Table 5). This result indicates that the quantification method overestimates the hydroxyapatite

volume fraction and, therefore, the bone mineral content. Furthermore, in Figure 12A-E, the bias is proportional to the nominal bone mineral content (*12*).

Figure 13 shows the relative errors for all image-based quantifications. For Qr40-80/150 kV, Qr40-90/150 kV, and I41s-80/130 kV, the relative errors are below 7.7%. This is smaller than for the values obtained with DEXA (between 7.9% and 14.5%). Also, the measured mean value of the BMC_{DEXA} and the respective standard deviation over ten measurements for each vertebra was (4.9±0.3) g, (10.3±0.3) g, and (15.0±0.3) g of hydroxyapatite (HA) for vertebrae 1, 2 and 3, respectively (*12*).

Lastly, the effective density (ρ_{eff}) and the effective atomic number (Z_{eff}) for each vertebra of the ESP were calculated. All values of ρ_{eff} and Z_{eff} are listed in Table 11 of Appendix 2: Bone Volume Fraction – Additional Tables and Figures (*12*). This data is mainly reported for future comparison studies.

Table 5. Data from Bland-Altman Analysis of the Quantification of Bone Mineral Content (Whole Vertebra) in the European Spine Phantom

Data Pair	**Image-based Quantification**	**Bias (g HA)**	**Lower Limit (g HA)**	**Upper Limit (g HA)**
BMC_{ESP} and BMC_{DSCT}	Br59-80/150 kV	−1.687	−3.592	0.219
	Qr40-80/150 kV	−0.277	−0.799	0.245
	Br59-90/150 kV	−1.956	−4.085	0.172
	Qr40-90/150 kV	−0.640	−1.372	0.092
BMC_{ESP} and $BMC_{SPECT/CT}$	I41s-80/130 kV	−0.567	−1.540	0.407
BMC_{ESP} and BMC_{DEXA}	DEXA	−1.037	−2.213	0.139

HA: hydroxyapatite.
Table modified from (*12*).

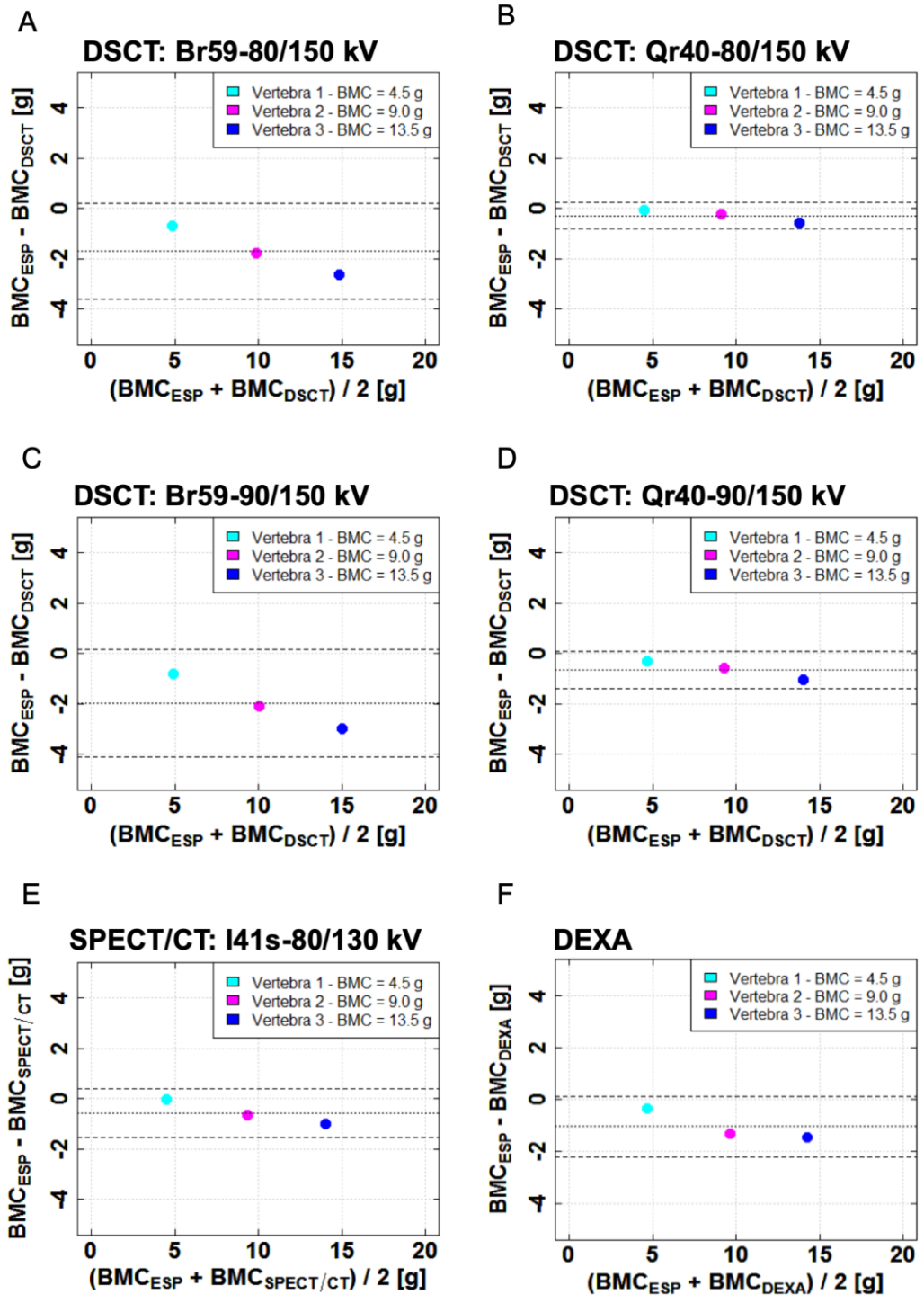

Figure 12. Bland-Altman plots of each image-based quantification.
A: Br59-80/150 kV. B: Qr40-80/150 kV. C: Br59-90/150 kV. D: Qr40-90/150 kV. E: I41s-80/130 kV. F: DEXA. Dotted line: mean of the differences (bias). Dashed lines: 95% confidence interval. Figure modified from (*12*).

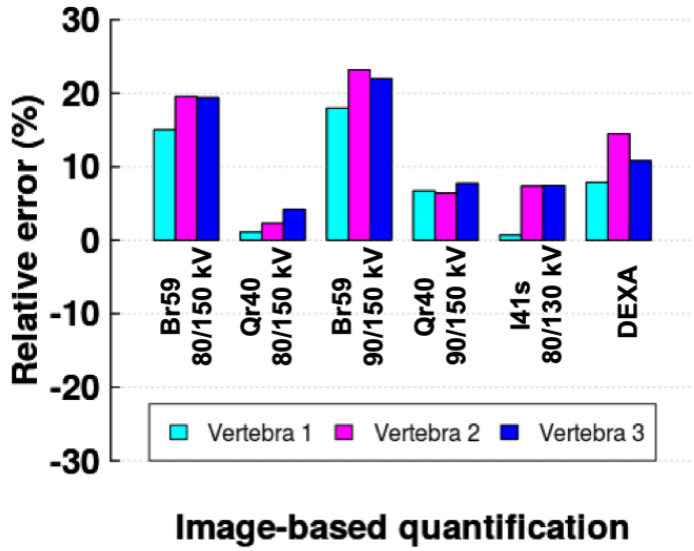

Figure 13. Relative errors associated with the quantification of the bone mineral content in the whole vertebrae (without transversal processes) of the European spine phantom.
Figure modified from (*12*).

2.4. Quantification of the Hydroxyapatite Volume Fraction in Spongiosa Regions of the European Spine Phantom

Following the analysis methodology used in the previous sections, Bland-Altman plots were generated to evaluate the agreement between the nominal values of the hydroxyapatite volume fraction in the spongiosa regions of the ESP (VF_{HA_ESP}) and the image-based quantification of the hydroxyapatite volume fraction for each CT image set (VF_{HA_DSCT} and $VF_{HA_SPECT/CT}$).

Figure 14 presents the Bland-Altman plots. The results agree with previous phantom measurements of this study. Figure 14B and Figure 14D, corresponding to the reconstruction kernel Qr40 (DSCT), show the smallest confidence interval and bias (see Table 6). Similar results were achieved by the image-based quantification I41s-80/130 kV (SPECT/CT). Concerning the bias, all image-based quantifications show negative values (between −0.28 VF_{HA} of hydroxyapatite and −1.96 VF_{HA} of hydroxyapatite) (see Table 6). This result indicates that the quantification method overestimates the hydroxyapatite volume fraction (*12*). Furthermore, Figure 14B, Figure 14D, and Figure 14E show that the bias tends to decrease with increasing bone mineral density. This tendency is contrary to the one observed in Figure 14A, and Figure 14C (DSCT and Br59 reconstruction kernel) as well as in Figure 11 and Figure 12.

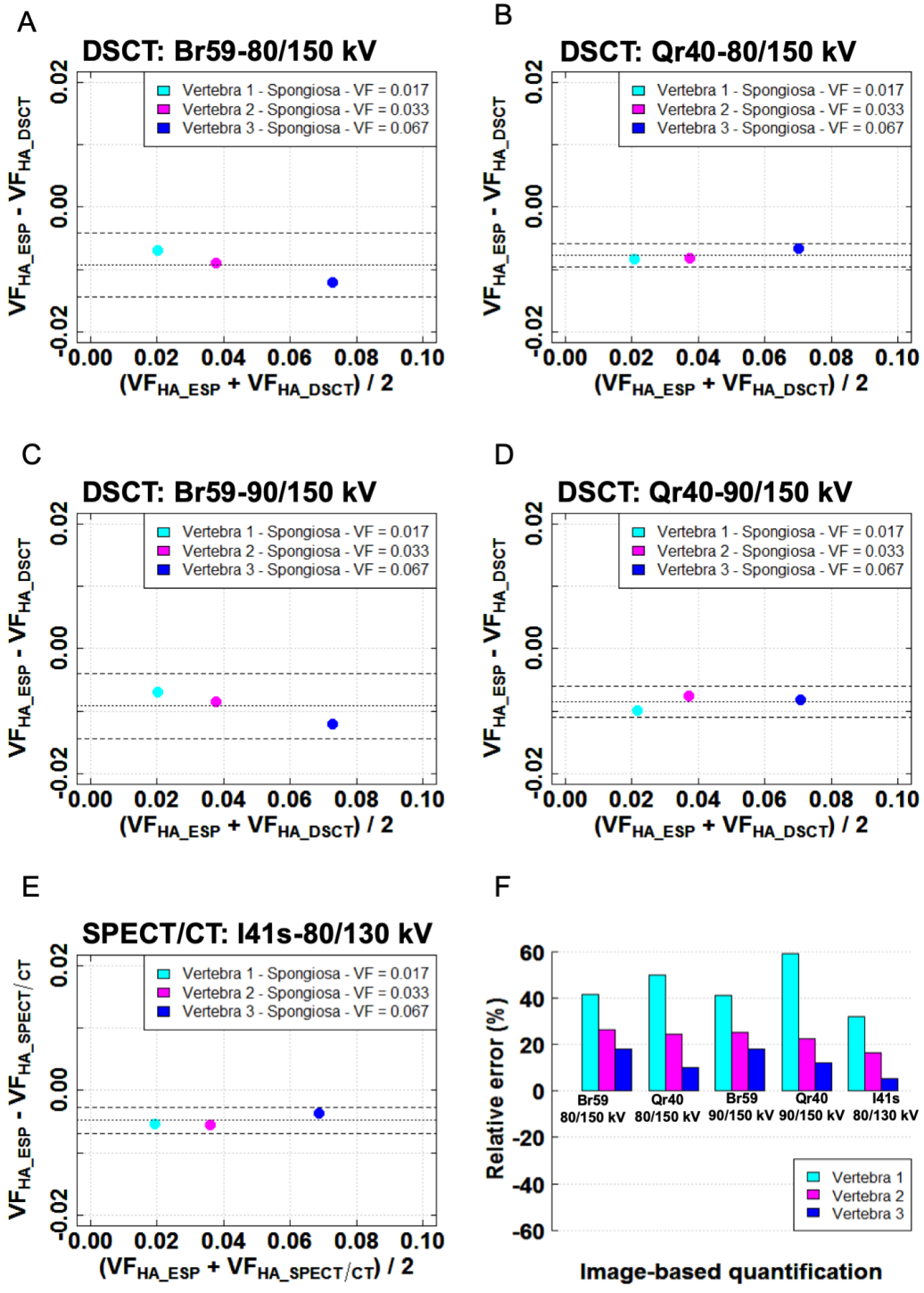

Figure 14. Bland-Altman plots of each image-based quantification:
A: Br59-80/150 kV. B: Qr40-80/150 kV. C: Br59-90/150 kV. D: Qr40-90/150 kV. E: I41s-80/130 kV. F: The relative error associated with the quantification of the hydroxyapatite volume fraction. Dotted line: mean of the differences (bias). Dashed lines: 95% confidence interval. Figure modified from (*12*).

Table 6. Data from a Bland-Altman Analysis of the Quantification of Hydroxyapatite Volume Fraction in Spongiosa Region of the European Spine Phantom

Data Pair	Image-based Quantification	Bias (VF_{HA})	Lower Limit (VF_{HA})	Upper Limit (VF_{HA})
VF_{HA_ESP} and VF_{HA_DSCT}	Br59-80/150 kV	−0.009	−0.014	−0.004
	Qr40-80/150 kV	−0.008	−0.010	−0.006
	Br59-90/150 kV	−0.009	−0.014	−0.004
	Qr40-90/150 kV	−0.009	−0.011	−0.006
VF_{HA_ESP} and $VF_{HA_SPECT/CT}$	I41s-80/130 kV	−0.005	−0.007	−0.003

HA: hydroxyapatite.
Table modified from (*12*).

Figure 14F shows that the relative errors tend to decrease with increasing the hydroxyapatite volume fraction. The relative error for each image-based quantification stays between: 18.1 % to 41.3 % (Br59-80/150 kV), 9.9 % to 49.7 % (Qr40-80/150 kV), 18.1 % to 41.3 % (Br59-90/150 kV), 12.1 % to 59.3 % (Qr40-90/150 kV), and 5.4 % to 31.7 % (I41s-80/130 kV) (*12*).

The image-based quantification I41s-80/130 kV shows the best agreement (Figure 14E) and the lowest relative errors (Figure 14F) between the measured values and the nominal values (*12*).

2.5. Quantification of the Mineral Bone (Hydroxyapatite) Volume Fraction and the Bone Volume Fraction in a Patient Dataset

In this section, a patient dataset (49.5 years old female) with a diagnosis of osteopenia in the limit to osteoporosis was studied retrospectively. Based on the DEXA study, the bone mineral content for lumbar vertebrae 1 and 2 was 8.0 g and 10.9 g. The relative error obtained from these values in comparison with the BMC_{DSCT} quantification were 7.6% and −8.4% in lumbar vertebrae 1 and 2, respectively (*12*).

Table 7 summarizes the values corresponding to the mineral bone mass fraction, bone mass fraction, the mineral bone volume fraction, and the bone volume fraction in lumbar vertebrae 1 and 2. Furthermore, the ratio of mineral bone mass fraction and a total bone mass fraction ($R_{HA/B} = MF_{HA}/MF_B$) is reported in Table 7 for each vertebra and each qualified VOI (*12*).

Table 7. Values of Mass and Volume Fractions of HA and Bone in lumbar Vertebrae 1 and 2 from a Patient Image Set.

Region		**Parameters**					
		MF_{HA}	VF_{HA}	VF_B[b]	MF_B	VF_B[c]	$R_{HA/B}$
Whole Vertebra[a]	Lumbar Vertebra 1	0.14	0.05	0.12	0.25	0.15	0.55
	Lumbar Vertebra 2	0.16	0.06	0.13	0.26	0.16	0.56
Spongiosa	Lumbar Vertebra 1	0.11	0.04	0.09	0.20	0.11	0.56
	Lumbar Vertebra 2	0.12	0.04	0.10	0.21	0.11	0.56

MF_{HA}: hydroxyapatite mass fraction
VF_{HA}: hydroxyapatite volume fraction
MF_B: bone mass fraction
VF_B: bone volume fraction
[a] Excluding transverse processes
[b] First volume fraction calculation method
[c] Second volume fraction calculation method
Table modified from (*150*)

Chapter V
Discussion

1. Quantification of the Fat Volume Fraction in the Lumbar Vertebrae

1.1. Quantification of the Fat Volume Fraction Using Two-point Dixon MRI

The quantification of the fat volume fraction using the validation phantom showed a good agreement between the nominal values of the fat volume fraction (VF_{F_0}) and the MRS-based quantification (VF_{F_MRS}) (Figure 7A and Figure 8A). This result validates the initial assumption, which considers the two-peak MRS approach as the gold standard for MR-based quantification of the fat volume fraction. Also, this result justifies the validation of the MRI-based quantification of the fat volume fraction by using a two-peak MRS approach (*8*).

The linear fit (Figure 7B) as well as the Bland-Altman plot (Figure 8B), corresponding to data pair 2 (VF_{F_0} and VF_{F_MRI}), showed that the MRI-based quantification of the fat volume fraction by using the two-point Dixon sequence overestimates the fat volume fraction for low values while underestimates it for high values. This observation is in agreement with previous findings (*8,13*).

The Bland-Altman plot of data pair 2 (Figure 8B) showed a larger confidence interval than data pair 1 (VF_{F_0} and VF_{F_MRS}, figure 8A). Therefore the agreement between the fat volume fraction nominal values (VF_{F_0}) and the MRI-based quantification (VF_{F_MRI}) is lower than that obtained with the MRS-based quantification (VF_{F_MRS}). Moreover, the maximum registered relative error between the fat volume fraction nominal values (VF_{F_0}) and the MRI-based quantification (VF_{F_MRI}) stayed below 10% (*8*).

The quantification of the fat volume fraction in volunteers permitted to validate the MRI-based quantification (VF_{F_MRI}) in the lumbar vertebrae. Also, it permitted to evaluate the MRI-based quantification (VF_{F_MRI}) in a heterogeneous medium (a mixture of adipose tissue, soft tissue, and trabecular bone, surrounded by cortical bone) (*8*). The Bland-Altman plot between MRI-based quantification (VF_{F_MRI}) by using the VOI_{Cube} and MRS-based quantification (VF_{F_MRS}) (Figure 9A) shows a small bias. Also, no significant difference was found between VF_{F_MRS} and VF_{F_MRI}. Therefore, despite the possible inhomogeneities in the static magnetic field B_0 that the heterogeneity of the bone marrow plus bone could create (*151*), a good agreement was found between VF_{F_MRS} and VF_{F_MRI} (*8*).

The Bland-Altman plot between MRI-based quantification (VF_{F_MRI}) by using $VOI_{Contour}$ and MRS-based quantification (VF_{F_MRS}) (Figure 9B) shows a larger bias than the one obtained with VOI_{Cube}. Also, a significant difference was found between VF_{F_MRS} and VF_{F_MRI}. This result

suggests that the fat volume fraction in the lumbar vertebrae is not homogeneously distributed (*8*). Therefore, an MRS-based quantification of the fat fraction is not representative of the fat volume fraction in the whole vertebral body. Thus, MRI-based quantification provides more detailed information about the spatial distribution and the mean value of the fat volume fraction in the whole vertebral body (*8*).

1.2. Correlation between Fat Volume Fraction and Age

The correlation between fat volume fraction and age has been evaluated in previous studies based on MRS quantification (*152,153*), MRI quantification, and histological analysis of samples extracted from cadavers (*154,155*). These studies documented an increase in fat volume fraction with age (*8*).

The analysis (Figure 10 and Table 3) performed in this study delivered a similar result, coupled with a slower bone marrow conversion rate in males (0.3% per year) than in females (0.5% per year). Furthermore, the fat volume fractions in males aged below 40 years were higher than in females in the same age group. In the age span between 40 and 49, this tendency is inverted due to the difference in the marrow conversion. Ishijima *et al.* (*156*) reported a similar result in lumbar vertebral bodies L1 to L3. They documented that the fat volume fraction in females is smaller than in males below 45 years and increases rapidly after this age (*8*).

1.3. Implications of the Dependency of the Cellularity Volume Fraction with Age and Gender in the Calculation of the Bone Marrow Absorbed Dose in Molecular Radiotherapies

In this section, the discussion is continued with respect to the cellularity volume fraction ($1 - Fat\ Volume\ Fraction$) to compare the data to reference values and literature related to absorbed dose calculations (*8*).

Cristy (*10*) proposed the first method to estimate the bone marrow distribution as a function of age in humans to be used for absorbed dose calculations. Based on Cristy's methodology, the cellularity volume fraction was fixed at 1 (0 fat volume fraction) for newborns. Subsequently, a progressive, age-dependent decrease of the cellularity volume fraction with values of 0.95 (1 year), 0.85 (5 years), 0.80 (10 years), 0.75 (15 years), 0.72 (25 years), and 0.70 (40 years) was defined. This data shows a fast decrease in the cellularity volume fraction in the first 25 years and an almost constant value during adulthood (25 years to 40 years). The ICRP Publications 70 and 89 (*1,2*) proposed a cellularity volume fraction of 0.7 for the reference man.

In relation to the linear model obtained in this study for males and females (Figure 10 and Table 3), two observations are highlighted:

i) The intercept of the linear model shows a different value to 0 at birth (Figure 10). As only data from adult patients were analyzed in this study; however, the information provided by the linear model between 0 years and 25 years should be discarded. More data would be necessary to make a justified statement (*8*).

ii) The cellularity volume fraction stayed in a range of [0.36, 0.84] for females with a mean of 0.59 ± 0.14 (k=1), and [0.29, 0.87] for males with a mean of 0.61 ± 0.12 (k=1) (*8*). This data variability combined with the result of the analysis of the predictive power of both linear models (predicted R-squared), which indicated a poor predictive power of the fat volume fraction as function of the age for females and males, led to the conclusion that the use of a reference value of the cellularity volume fraction (or fat volume fraction) is not representative for all adults (*8*). Furthermore, a closer look at the data of this work shows that, in patients with similar age, different cellularity volume fractions were found, for example: i) Two females (58 years and 59 years) with cellularity volume fractions of 0.48 and 0.71. ii) Two males (74 years and 75 years) with cellularity volume fractions of 0.46 and 0.74 (*8*).

The association of these observations with the calculation of the bone marrow absorbed dose supports the conclusion documented by Bolch (*11*), who proposes that simple mass scaling of the reference man radionuclide S value is not sufficient for achieving an adequate assessment of the bone marrow absorbed dose for patient-specific dosimetry (*8*). Therefore, the cellularity volume fraction in bone marrow should be considered as patient-specific in the assignment of radionuclide S values for bone marrow absorbed dose calculations (*8*).

The impact of the quantification of the cellularity volume fraction on the calculation of the absorbed dose in bone marrow dosimetry is defined by the accuracy of the two-point Dixon sequence. The relative errors obtained in the phantom experiment stayed below 10% (*8*). As a first consideration, it should be stated that, currently, there is no individualized and non-invasive procedure, implemented for patient-specific internal dosimetry, which quantifies the cellularity volume fraction. A second consideration comes from the dependency of the S values on the changes in the cellularity volume fraction. Recently, Geyer *et al.* (*19*) used O'Reilly's model of the reference adult female (*110*) to apply changes to the cellularity volume fraction of a 3-dimensional radiation transport model of bone and bone marrow of three different bone sites (ribs, lumbar vertebra three and parietal bone). They calculated the value of $S(AM \leftarrow AM)$ (active marrow self-irradiation) for six radionuclides (^{45}Ca, ^{153}Sm, ^{90}Y, ^{223}Ra, ^{219}Rn, and ^{215}Po), in combination with changes of the cellularity volume fraction in the order of 10% to 100% in intervals of 20%. They also calculated the S values for the ICRP reference cellularity volume

fraction (*1,2*) for ribs and lumbar vertebrae (0.7), and parietal bone (0.38). These S values were set as reference S values. From the Monte Carlo simulation, Geyer *et al.* (*19*) found changes to the reference S value that were larger than 10% for all radionuclides. A similar result can be calculated from Shah's (*129*) published S values for ^{177}Lu and ^{131}I of lumbar vertebrae. Geyer *et al.* (*19*) concluded that changes to the reference S value due to active marrow self-irradiation are greater than for other $r_T \leftarrow r_S$ geometries (e.g., trabecular bone volume to active marrow, or trabecular bone surface to active marrow). Therefore a relative error below 10% in the quantification of the cellularity volume fraction might be acceptable for molecular radiotherapies (*8*).

1.4. Study Limitations

This study analyzed only lumbar vertebrae. For a comprehensive assessment of the average absorbed dose on the active bone marrow, an analysis of the entire skeleton would be required to obtain the cellularity volume fractions in multiple bone sites (*8*).

This study was limited to the use of a two-point Dixon sequence available in the clinical MRI system (MAGNETOM Prisma, Siemens Healthineers). The purpose was the test/validation and not the optimization of the MRI technique. Therefore, modifications to the available clinical Dixon sequence are beyond the scope of this study.

The segmentation of all the quantified VOI's was performed by the same person (MSR) with the same software and technique. This approach reduced the inter-observer variability. However, intra-observer variability cannot be excluded (*8*).

2. Quantification of the Trabecular Bone Volume Fraction

2.1. Quantification of Hydroxyapatite Volume Fraction in Samples of the Validation Phantom

Thomsen et al. (*9*), by using micro-CT quantified, the mineralized bone volume per total bone (BV/TV) in lumbar vertebra 2 (the BV/TV is equivalent to the hydroxyapatite volume fraction). They analyzed bone samples of 41 women and 39 men and documented linear fit parameters for females and males. By using these linear fit parameters, it is possible to calculate an expected range of BV/TV in adults. Therefore, for females with 20 years, 50 years, and 80 years of age, the expected BV/TV is 0.07, 0.11, and 0.15, respectively (*12*). In males, these values are 0.08, 0.12, and 0.15 for the same ages (*12*). The hydroxyapatite volume fraction in samples of the validation phantom was 0.033, 0.067, and 0.10. Therefore, the hydroxyapatite volume fraction in the samples covers a representative range of the mineral bone volume fraction in humans (*12*).

Furthermore, the technique used in this study to prepare the samples permits to create a material in which the hydroxyapatite (α-TCP) particles achieve a mean size of 9.34 µm and in which they are homogeneously distributed (*147*). The trabecular bone thickness is in the range of 100 µm to 200 µm (*9*). Therefore, considering that the volume of a CT voxel is in the order of 1 mm^3 to some tens of cubic millimeters, it is expected that the distribution and size of the hydroxyapatite particle accomplishes a good representation of the trabecular bone spatial distribution (*12*). The use of hydroxyapatite in solution or as a polymer as in this study is the standard form to reproduce the physical characteristics of mineral bone in CT experiments (*12,20-22,143*).

The DEQCT method proposed by Liu *et al.* (*22*) is based on the mass-conservation of the materials which make up the mixture. The main advantage of this quantification algorithm is that mass is conserved during a chemical reaction (*22*). In this work, the volume-conservation of the material that makes up the mixture was assumed. This assumption is based on the fact that hydroxyapatite, fat, and water are immiscible materials (*12*). The quantification of the hydroxyapatite volume fraction in the samples of the validation phantom confirmed this assumption.

The result obtained from the quantification of the hydroxyapatite volume fraction in the samples shows a good agreement with the nominal values. For all image-based quantification (Figure 11), an overestimation of the hydroxyapatite volume fraction was observed, and the maximum relative error was below 14.2%. This observation indicates that the DEQCT method overestimates the quantified hydroxyapatite mass fraction and, therefore, the hydroxyapatite volume fraction. The proportionality between the difference $\left(VF_{HA_0} - VF_{HA_DSCT}\right)$

or $(VF_{HA_0} - VF_{HA_SPECT/CT})$, and the mean values $\left((VF_{HA_0} + VF_{HA_DSCT})/2\right)$ or $\left((VF_{HA_0} + VF_{HA_SPECT/CT})/2\right)$ (Figure 11A-E), can be interpreted as an increase in the overestimation of the quantified hydroxyapatite volume fraction as a function of the nominal hydroxyapatite volume fraction. This tendency cannot be attributed to the sample preparation because it also occurs in the quantification of the bone mineral content in the European spine phantom (Figure 12A-E). A possible source of error is the determination of the empirical constant C and K used in equations 39 and 40. These constant were included to correct for beam hardening (proportional to the atomic number) and the lack of information about the X-ray spectra and the detector sensitivity. Also, the fact that the sample and spongiosa region of ESP with a concentration of 200 mg/cm^3 of hydroxyapatite (HA) present a smaller relative error and a slightly different data tendency in the Bland-Altman plots (Figure 11A-E) might be associated with the determination of the empirical constant C, which was obtained by correction of the quantified hydroxyapatite volume fraction in the reference bone samples (200 mg/cm^3 HA, 800 mg/cm^3 HA and 1250 mg/cm^3 HA) of the CIRS Model 062M phantom. The main objective of the empirical constant C is to improve the quantification of materials with a relatively high effective atomic number and effective density by the correction of the beam hardening effect (*22*).

Lastly, another source of error is the disagreement between the real chemical element composition of each quantified material and the chemical element composition used in the DEQCT method. However, this error source might not be the most important one (at least for material with a low atomic number). For example, the quantification of the samples with a HA concentration of 150 mg/cm^3 in an inhomogeneous medium (47.5 % volume of fat and 47.5 % volume of agar) showed that, despite the inclusion of fat in the sample, the result of the hydroxyapatite volume fraction quantification follows the tendency of 100 mg/cm^3 HA and 300 mg/cm^3 HA samples (*12*).

2.2. Quantification of Bone Mineral Content in the European Spine Phantom Using DEXA, DSCT, and SPECT/CT

The quantification of the bone mineral content shows a similar data tendency (proportionality between the differences and the means of the hydroxyapatite volume fractions (Figure 12A-E)) as the quantification of the hydroxyapatite volume fraction in the validation phantom. The image-based quantifications Qr40-80/150 kV, Qr40-90/150 kV, and I41s-80/130 kV show a good agreement between the measured and the nominal values of the bone mineral content (Figure 12B, Figure 12D and Figure 12E) (*12*). Also, they show a smaller bias and confidence interval than DEXA-based quantification (*12*). Figure 13 shows that the relative errors for these image-based quantifications are below the relative errors obtained with the

DEXA. These results also show that the quantification of BMC in the whole vertebra using DEQCT is feasible (*12*). The better quantification of the BMC by using image-based quantifications Qr40-80/150 kV, Qr40-90/150 kV, and I41s-80/130 kV, might be related to differences in the definition of the quantification area or volume. In case of DEXA, an automatic threshold selection of the region of interest is used (*12*). In the case of DEQCT, a three-dimensional selection of the volume of interest (whole vertebra without transverse processes) is used (*12*).

The image-based quantifications Br59-80/150 kV and Br59-90/150 kV present a larger bias, confidence interval, and relative error than other image-based quantifications (*12*). This result might be related to the reconstruction kernel Br59, which is dedicated to bone imaging, and it might enhance the bone signal (*12*).

2.3. Quantification of Hydroxyapatite Volume Fraction in Spongiosa Regions of the European Spine Phantom

This section is of particular interest as the objective of this study is to evaluate the feasibility of measuring the bone volume fraction in the spongiosa (or trabecular bone volume fraction). Therefore, the spongiosa regions of the European spine phantom provide an optimal geometry for this evaluation (*12*).

Based on Figures 14E and 14F, the image-based quantification I41s-80/130 kV (SPECT/CT) provides the lowest relative errors (*12*): 32.0% for 0.017 VF_{HA} (mineral bone volume fraction), 16.5% for 0.033 VF_{HA}, and 5.4% for 0.067 VF_{HA}. Also, a better agreement was found based on the Bland-Altman plots. Liu et al. (*22*), for the same mineral bone volume fraction (or hydroxyapatite concentrations of 50 mg/cm^3, 100 mg/cm^3, and 200 mg/cm^3, respectively) used a second-generation DSCT (SOMATOM Definition DS, Siemens Healthineers), and found relative errors equal to −20%, −11% and −18% in the hydroxyapatite mass fraction (equivalent to the hydroxyapatite volume fraction by using equation 36). The authors used samples with cylindrical geometry, which might play an important role especially for the spongiosa region due to beam hardening caused by the cortical wall of the vertebral bodies, the spinous process, and the transverse processes (*12*). Comparing the 0.033 VF_{HA} sample of the validation phantom and the 0.033 VF_{HA} spongiosa region of the ESP, the relative errors of all image-based quantifications were smaller in the validation phantom (cylindrical geometry sample) than in the ESP phantom. For example: 4.83% vs. 24.6% (Qr40-80/150 kV), 10.9% vs .22.5% (Qr40-90/150 kV), and 5.7% vs. 16.5% (I41s-80/130 kV). In case of the 0.067 VF_{HA} sample and spongiosa region, the same comparison presents 2.68% vs. 9.9% (Qr40-80/150 kV), 8.3% vs. 12.1% (Qr40-90/150 kV), and 6.1% vs. 5.4% (I41s-80/130 kV). These results show that the implemented post-reconstruction DEQCT method presents deficiencies

to correct for beam hardening effects (*12*). This observation was documented by Liu et al. (*22*), who reported that the accuracy of the HU is affected by beam hardening, scatter, and partial volume effects.

The inversely proportional relationship between relative error and hydroxyapatite volume fraction (Figure 14F) shows that the DEQCT method is inaccurate in the range of low hydroxyapatite volume fraction (below 0.033 VF_{HA} or 100 mg/cm^3 HA). This result might be related to the range for which the constants C and K were calculated (200 mg/cm^3 to 1250 mg/cm^3 of hydroxyapatite). Therefore, a way to improve the DEQCT method might be to calculate the values of C and K for samples with an HA concentration lower than 200 mg/cm^3, and to include material with an chemical element composition equivalent to human soft tissue.

The range of expected hydroxyapatite volume fraction based on Thomsen et al. (*9*) stayed between 0.08 (or 240 mg/cm^3 HA) and 0.15 (or 450 mg/cm^3 HA) for males, and between 0.07 (or 210 mg/cm^3 HA) and 0.15 (or 450 mg/cm^3 HA) for females (*12*). Therefore, by using SPECT/CT, the maximum expected error should be in the order of 5.44%, which corresponds to the 0.067 VF_{HA} (200 mg/cm^3 HA) spongiosa region of the ESP (*12*). However, patients with malignant bone disease might present lower bone mineral densities (or hydroxyapatite volume fractions) due to bone destruction (osteolytic lesions) or a buildup of new, weaker bone (osteoblastic lesions) (*12,157*). Future studies, with a vertebra geometry and a hydroxyapatite volume fraction in the order of 0.15, should be performed to validate the DEQCT method in the range of expected hydroxyapatite volume fraction values for adults (*12*).

The differences between SPECT/CT (I41s-80/130 kV) and the DSCT (Br59-80/150 kV, Qr40-80/150 kV, Br59-90/150 kV, Qr40-90/150 kV) based-quantification might be related with the (un-)available information of the detector sensitivity function. In this study for both CT systems, the same detector response function was assumed, which was extracted from the publication by Liu *et al.* (*22*). Liu *et al.* used a second-generation DSCT equipped with a Siemens Stellar detector (third detector generation) (*158*). The DSCT used in this work was a third-generation DSCT equipped with a Siemens Stellar-infinity detector (the newest detector generation) (*12,158*). Also, the SPECT/CT is equipped with an ultra-fast ceramics detector (second detector generation) (*12,158*).

2.4. Quantification of the Mineral Bone (Hydroxyapatite) Volume Fraction and the Bone Volume Fraction in a Patient Dataset

In the first step, the bone mineral contents measured by DEXA and DSCT were compared. The relative errors were 7.6% and −8.4% for lumbar vertebrae 1 and 2, respectively (*12*). A source of error not associated with the DEQCT method corresponded to the patient positioning. For the DEXA examination, a plain patient bed was used in conjunction with a

padded box under the patient's legs, which helped to correct the lumbar curvature. As a result, the lumbar vertebrae are positioned parallel to the patient bed. In case of a thorax examination by using the DSCT, no specific positioning is typically used (*12*). Therefore in the segmentation of the CT images, it was difficult to reproduce the same vertebral position as in the DEXA study (*12*).

The main objective of this section was to quantify the mineral bone volume fraction and the bone volume fraction in a patient dataset by using the following two approaches: i) by using a reference ratio of mineral bone mass fraction to total bone mass fractions ($R_{HA/B}$), and ii) by changing hydroxyapatite to cortical bone, which implies the use of cortical bone, soft tissue, and adipose tissue as material composition (*12*) based on the chemical element composition documented by the ICRU Report 44 (*34*). Table 7 tabulates the bone mass fraction and bone volume fraction by the two previously described approaches (*12*).

The first approach is based on the use of a reference ratio of the mineral bone to total bone ($R_{HA/B}$). The bone volume fraction is obtained by applying equation 38. The weakness of this approach lies in the lack of reference values for many bone sites (*12*). Based on the revised literature, only Quelch et al. (*148*) provides information about the percentage of mineral bone by weight in the bone of the midshaft of the femur, vertebra, and rib. Also, these values corresponded to dry samples. Therefore, the lack of information related to the water content might introduce an error in the calculation of the bone volume fraction (*12*).

The second approach (based on a change in the element description of mineral bone to cortical bone) provides a better patient-specific assessment. However, it has a limitation in that it is based on the reference chemical element composition of bone proposed by the ICRU in Report 44 (*34*). Therefore, the grade of agreement between ICRU report 44 (*34*) and the chemical element composition of the bone in an individual patient is unknown (*12*).

In Table 7, it can be observed that the values of the bone volume fraction in the whole vertebra (without transversal processes) for both methodologies are similar 0.124 (approach 1) vs. 0.148 (approach 2) in lumbar vertebra 1 and 0.132 (approach 1) vs. 0.157 (approach 2) in lumbar vertebra 2. In case of the bone volume fraction in the spongiosa a similar tendency was found: 0.093 (approach 1) vs. 0.110 (approach 2) in lumbar vertebra 1, and 0.095 (approach 1) vs. 0.113 (approach 2) in lumbar vertebra 2. The result of higher values of bone volume fraction with approach 2 than that obtained with approach 1 (*12*), might be related with the non-consideration of water content in the quantification of mineral bone and organic material by Quelch et al. (*148*). If water is taken into account, the ratio of mineral bone to total bone ($R_{HA/B}$) should be lower than 0.663 (Quelch et al. (*148*)). For example, Goodsitt *et al.* (*20,21*) in the preparation of a set of calibration standards for estimating the fat and mineral content of vertebrae using DEQCT assumed for cortical bone a water content of 12.2%, a

protein content of 24.6%, a mineral bone content of 58% and 5.2% of others contents (e.g., monosaccharide) (*12*).

Also, Table 7 shows that all the whole vertebra values are slightly smaller than for the spongiosa. This result can be related to the spatial distribution of bone in the vertebrae (*12*). The whole vertebra considers cortical bone (high concentration of bone) plus spongiosa (low concentration of bone) (*12*).

A remarkable observation is that the values of the mass fraction of mineral bone are, in all measurements, smaller than the bone mass fraction (*12*). This result is expected due to the material composition of bone (mineral bone plus organic material) (*12*). Furthermore, the ratio of mineral bone mass fraction and total bone mass fraction ($R_{HA/B}$) lie all in the range of 0.554 to 0.558 (*12*). These values are smaller than the 0.663 values by Quelch et al. (*148*). This result might be related to the not considering the water content in the quantification of mineral bone and organic material by Quelch et al. (*148*).

2.5. Implications of the Quantification of the Bone Volume Fraction in the Calculation of the Bone Marrow Absorbed Dose in Molecular Radiotherapies

The quantification of the fat volume fraction and the bone volume fraction in the spongiosa (for classification: in the literature, the latter is often referred to as *trabecular bone volume fraction*) permits to achieve a full spatial characterization of the spongiosa tissue. This information plays a main role in the calculation of specific S values based on 3-dimensional radiation transport models (*19,35,110,111*). These models used 3-dimensional trabecular bone microstructures obtained from a specific skeletal site of a human cadaver. Therefore, they are not representative for all patients undergoing molecular radiotherapy. Geyer *et al.* (*19*) highlight the need to develop a parameterized computational model of bone and bone marrow that permits the calculation of S values in the range of patient measurements of marrow cellularity (obtained by MRI) and bone mineral density (obtained by DEQCT). As an example, Geyer *et al.* (*19*) used O'Reilly's model of the reference adult female (*110*) to apply changes in the order of ±5%, ±10%, and ±15%, to the trabecular bone volume fraction of the 3-dimensional trabecular bone microstructure of three different bone sites (ribs, lumbar vertebra 3, and parietal bone). They calculated the $S(AM \leftarrow TBV)$ values (irradiation of active marrow by the trabecular bone volume) for six radionuclides (^{45}Ca, ^{153}Sm, ^{90}Y, ^{223}Ra, ^{219}Rn, and ^{215}Po). They found, for ribs, and lumbar vertebra 3, differences to the reference S value (obtained from no change of the trabecular bone volume fraction of the sample) larger than 10% for ^{45}Ca, ^{223}Ra, ^{219}Rn, and ^{215}Po. In case of ^{153}Sm and ^{90}Y, the changes were below 10%. These changes lie in the order of the relative errors of the quantification of the mineral bone volume fraction obtained with the DEQCT method (5.4% for SPECT/CT and 10% for DSCT) for a bone

mineral (hydroxyapatite) density ≥200 g/cm^3 in the spongiosa (*12*). Therefore, it is expected that the impact of the quantification of the trabecular bone volume fraction will be significant for radionuclides such as ^{45}Ca, ^{223}Ra, ^{219}Rn, and ^{215}Po, which show an important correlation with changes in trabecular bone microstructure (*12*). In the case of radionuclides such as ^{153}Sm and ^{90}Y, future studies should be performed to increase the accuracy of the DEQCT method and, thus, to have a substantial effect on the selection of the S value (*12*). For ^{177}Lu, there is no information regarding the influence of the change in the trabecular bone volume fraction. Hence, futures studies should be performed to determine the impact of the trabecular bone volume fraction in the selection of the $S(AM \leftarrow TBV)$ value for ^{177}Lu (*12*).

Furthermore, Geyer *et al.* (*19*) used, for lumbar vertebra, a bone microstructure with a bone volume fraction equal to 0.13. The bone sample was extracted from a 45-year-old female cadaver and imaged with a micro-CT (*110*). Therefore, the bone volume fractions simulated by Geyer *et al.* are in the range of 0.11 and 0.15. Thomsen et al. (*9*), using micro-CT images, reported bone volume fraction in the range of 0.08 to 0.15 for females and 0.07 to 0.15 for males. Consequently, Geyer's study does not reflect the whole range of bone volume fraction values for the lumbar vertebrae. A study that considers lower bone volume fractions is necessary to complete the evaluation of the impact of the quantification of the bone volume fraction on vertebrae for radiation dosimetry in adults.

Lastly, Geyer et al. (*19*) found for $S(AM \leftarrow TBV)$ changes larger than ±10% for all radionuclides in the parietal bone. They concluded that there is more variability in the values of $S(AM \leftarrow TBV)$ in bones with a high proportion of trabecular bone. Consequently, a study that explores the quantification of the bone volume fraction on other anatomical regions is required.

2.6. Study Limitations

This study was limited to vertebral geometries. Therefore, futures studies should be performed to evaluate the DEQCT method in other bone sites such as parietal bone, femoral heads, hips, and humeral heads. Also, the dimensions of the European spine phantom are not representative for variety of patient's sizes. Consequently, futures studies with other phantom sizes are recommended (*12*).

The segmentation of all the quantified VOI's was performed by the same person (MSR) with the same software and technique. While this approach reduced the inter-observer variability, intra-observer variability cannot be excluded (*12*).

The lack of information regarding detector sensitivity function and X-ray spectra might limit the accuracy of the DEQCT method. Furthermore, the lack of calculated values of the constants C and K in the range of low hydroxyapatite concentration and human soft tissues

(e.g., muscle, liver, and adipose tissue) might have an important impact in the accuracy of the DEQCT method in the quantification of materials composed of low concentrations of hydroxyapatite.

Chapter VI
Conclusion

This dissertation had two objectives: i) to apply magnetic resonance imaging (MRI) for quantification of the fat volume fraction in lumbar vertebrae, and ii) to validate a method based on dual-energy quantitative computed tomography (DEQCT) for quantification of trabecular bone volume fraction.

With regard to the first objective, the results obtained in this study provide enough evidence to validate the use of the two-point Dixon sequence as a non-invasive method for the quantification of the fat volume fraction in bone marrow in a clinical setting. This quantification technique overestimates the fat volume fraction for low values, while it underestimates for high values (*8*). However, the two-point Dixon sequence provides sufficient accuracy, especially when considering the high dependency of the value of $S(AM \leftarrow AM)$ on changes in the cellularity volume fraction (*19*). Furthermore, this MRI technique allows acquiring high-resolution images by a fast acquisition (the entire abdomen in a single breath-hold), which permits to take into account internal inhomogeneities of the fat tissue (or cellularity) of bone marrow. Lastly, the two-point Dixon sequence allows the acquisition of images over a large anatomical region, which in turn permits the analysis of multiple bone sites in one acquisition (*8*).

This study also provides evidence about the differences in marrow conversion between females and males (*8*). Moreover, a high variability of the cellularity volume fraction in adults was observed (*8*). Besides, it was found that the linear models are unable to predict the fat volume fraction with regard to gender and age (*8*). In conclusion, the cellularity volume fraction of the ICRP reference man is not representative for all the patients analyzed in this study. Instead, the cellularity volume fraction should be considered as patient-specific in the assignment of radionuclide S values for bone marrow absorbed dose calculation (*8*).

To address the second objective, a non-invasive DEQCT method was implemented and validated. This method allows the quantification of the bone volume fraction in the spongiosa in a clinical setting with sufficient accuracy, mainly for alpha-emitting radionuclides, which show an important dependency of the value of $S(AM \leftarrow TBV)$ on changes of the trabecular bone volume fraction (*19*). The DEQCT method presented and overestimation of the hydroxyapatite volume fraction in all quantified VOI's (*12*). This result might be related to insufficient information about the X-ray spectra and the detector sensitivity function (*12*), or due to the already documented limitation of the method to correct for beam hardening (*22,94*). Furthermore, the lack of calculated values of the constants C and K in the range of low

hydroxyapatite concentration and human soft tissues (e.g., muscle, liver, and adipose tissue) might be related to the observed overestimation. Despite these limitations, this method makes it possible to quantify the bone volume fraction (mineral bone plus organic material) by using the chemical element composition of bone (ICRU report 44 (*34*) and achieve a better patient-specific assessment (*12*).

The methods developed in this study are a significant starting point for future studies. Furthermore, they provide relevant evidence about the feasibility of measuring the fat volume fraction and the bone volume fraction in the spongiosa in a clinical setting. However, further studies that investigate improvements in the MRI technique and the DEQCT method are necessary. In case of the DEQCT method, it is necessary to validate the method in other bone sites (e.g., parietal bone, femoral heads, hips, and humeral heads). Additionally, for the DEQCT method, it is essential to evaluate the feasibility of quantifying the bone volume fraction on spongiosa by using low dose CT images (typically used for SPECT attenuation correction). Lastly, for the DEQCT, further studies that investigate the impact of the estimation of the constants C and K, in the range of low hydroxyapatite concentration and human soft tissue equivalent material, in the quantification of the bone volume fraction. In case of MRI, a future objective is to evaluate the potential use of ultra-fast echo MRI techniques for quantifying the bone volume fraction or the development of a clinical 3-point Dixon sequence for more accurate fat-water separation.

Appendix 1: Fat Volume Fraction – Additional Tables and Figures

Table 8. Linear Fit Parameters of Retrospective Quantification of the Fat Volume Fraction in 46 Sequentially Scanned Patients Using MRI

Lumbar Vertebra	Slope (VF_{F_Y}/VF_{F_X})	Slope Standard Error (VF_{F_Y}/VF_{F_X})	Intercept (VF_{F_Y})	Intercept Standard Error (VF_{F_Y})	Correlation Coefficient (r)	p-value
Female						
L5	0.005	0.001	0.161	0.069	0.60 *	0.001
L4	0.006	0.001	0.010	0.072	0.74 †	0.000
L3	0.005	0.001	0.135	0.071	0.69 †	0.001
L2	0.006	0.001	0.101	0.069	0.72 †	0.000
L1	0.005	0.001	0.125	0.080	0.60 †	0.004
Average	0.005	0.001	0.125	0.064	0.74†	0.001
Male						
L5	0.003	0.001	0.205	0.078	0.52 *	0.013
L4	0.003	0.001	0.223	0.072	0.50 *	0.015
L3	0.003	0.001	0.226	0.066	0.53 *	0.010
L2	0.003	0.001	0.193	0.067	0.60 *	0.003
L1	0.003	0.001	0.187	0.073	0.54 *	0.009
Average	0.003	0.001	0.216	0.069	0.53*	0.011

* Spearman's rank correlation test
† Pearson's product-moment correlation test
X and Y are the data sources (MRI, MRS or nominal values) of the respective data pair
Table modified from (*8*).

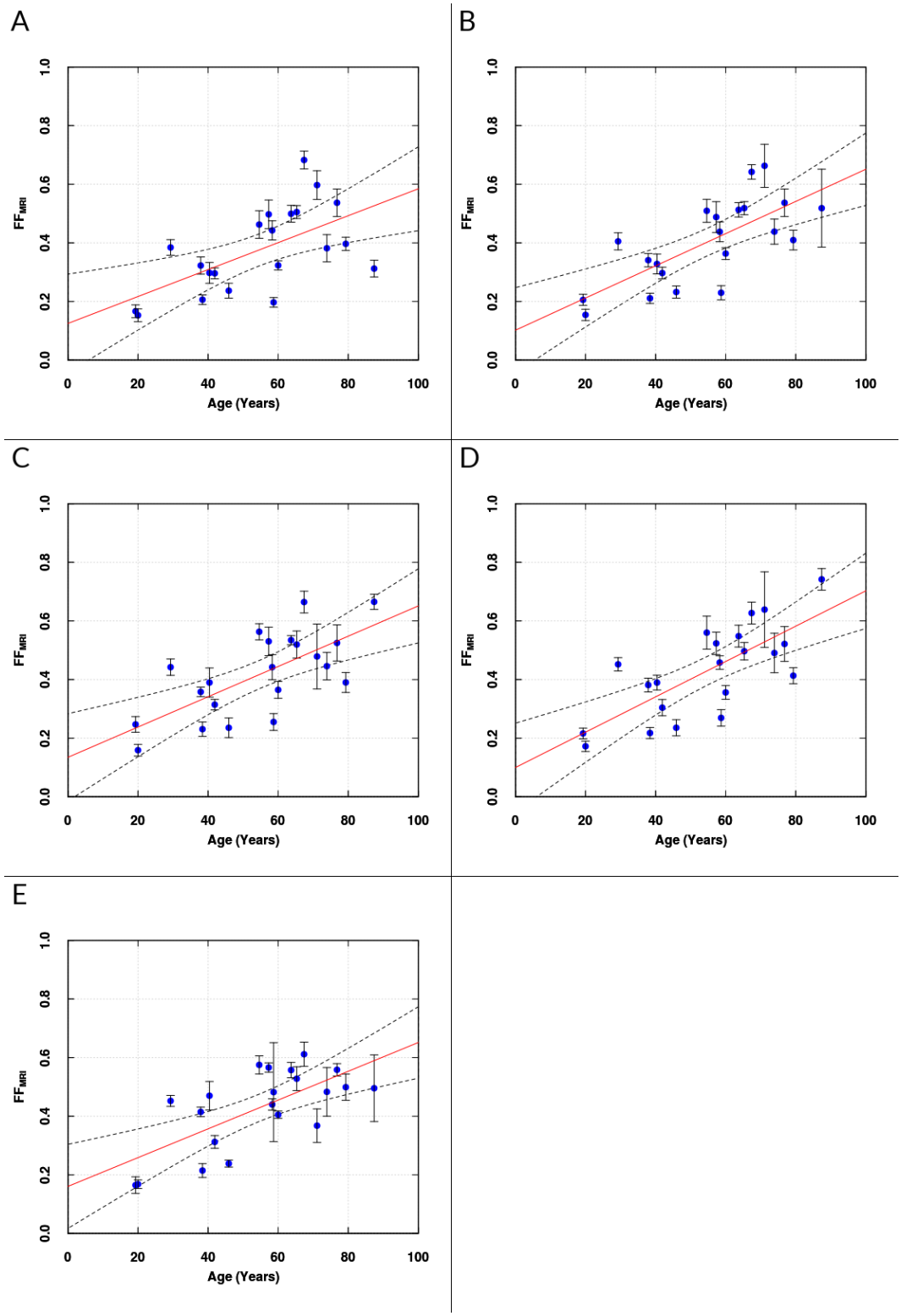

Figure 15. Age-dependency of the fat fraction in lumbar vertebrae in females. A: Lumbar Vertebra 1. B: Lumbar Vertebra 2. C: Lumbar Vertebra 3. D: Lumbar Vertebra 4. E: Lumbar Vertebra 5. Center line (solid red) corresponds to the linear fit. Top and bottom lines (black dashes) correspond to the 95% confidence interval. © Institute of Physics and Engineering in Medicine. Reproduced with permission. All rights reserved. Figure taken from (*8*).

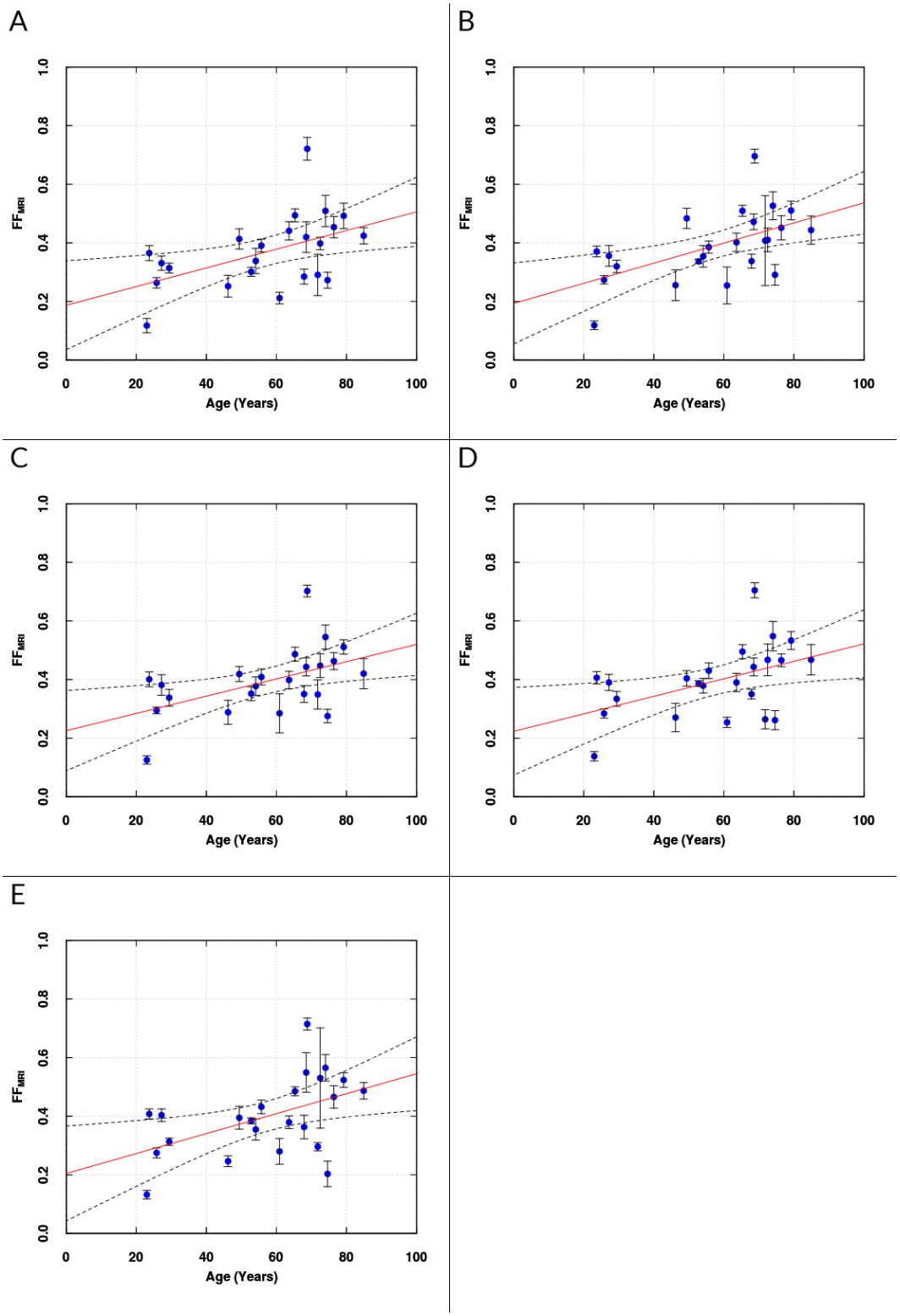

Figure 16. Age-dependency of the fat fraction in lumbar vertebrae in males.
A: Lumbar Vertebra 1. B: Lumbar Vertebra 2. C: Lumbar Vertebra 3. D: Lumbar Vertebra 4. E: Lumbar Vertebra 5. Center line (solid red) corresponds to the linear fit. Top and bottom lines (black dashes) correspond to the 95% confidence interval. © Institute of Physics and Engineering in Medicine. Reproduced with permission. All rights reserved. Figure taken from *(8)*.

Appendix 2: Bone Volume Fraction – Additional Tables and Figures

Table 9. Chemical Element Composition of Calibration Samples.

Material	Element composition				
	H	C	O	P	Ca
Water	0.112	--	0.888	--	--
HA	0.002	--	0.414	0.185	0.399

Table taken from (*12*).

Table 10. Z_{eff} and ρ_{eff} values of Validation Phantom and CIRS model 062.

Reconstruction Kernel and Energies	Parameter	Validation Phantom Sample (mg/cm^3)			CIRS model 062 Sample (mg/cm^3)		
		100	200	300	200	800	1250
Nominal Values	Z_{eff}	8.7	9.9	10.8	10.2	13.5	14.5
	$\rho_{eff}(g/cm^3)$	1.1	1.2	1.3	1.2	1.5	1.8
DSCT							
Br59-80/150 kV	Z_{eff}	8.3	9.0	9.5	9.0	10.8	11.4
	$\rho_{eff}(g/cm^3)$	1.2	1.2	1.3	1.2	1.5	1.8
Qr40-80/150 kV	Z_{eff}	8.3	9.1	9.7	9.2	11.3	12.1
	$\rho_{eff}(g/cm^3)$	1.2	1.3	1.3	1.2	1.5	1.8
Br59-90/150 kV	Z_{eff}	8.2	8.9	9.4	8.9	10.5	11.1
	$\rho_{eff}(g/cm^3)$	1.2	1.2	1.3	1.2	1.5	1.8
Qr40-90/150 kV	Z_{eff}	8.3	9.0	9.5	9.0	10.9	11.7
	$\rho_{eff}(g/cm^3)$	1.1	1.2	1.3	1.1	1.5	1.8
SPECT/CT							
I41s-80/130 kV	Z_{eff}	8.6	9.6	10.4	9.6	12.6	13.2
	$\rho_{eff}(g/cm^3)$	1.2	1.2	1.3	1.1	1.5	1.8

Note: nominal values of Z_{eff} were calculated using the equation $Z_{eff}^3 = \frac{\sum_i Z_i^3 \rho_i}{\sum_i \rho_i} = w_i \sum_i Z_i^3$ where w_i correspond to the fraction by weight of the i-*th* atomic constituent. Fractions by weight were calculated by the chemical formulation of the samples and in the case of CIRS phantom from a certificate of calibration.
Table modified from (*12*)

Table 11. Z_{eff} and ρ_{eff} Values of European Spine Phantom.

Reconstruction Kernel and Energies	Parameter	Whole Vertebra*			Spongiosa		
		V1	V2	V3	V1	V2	V3
DSCT							
Br59-80/150 kV	Z_{eff}	8.8	9.4	9.8	8.0	8.5	9.3
	$\rho_{eff}(g/cm^3)$	1.1	1.2	1.2	1.0	1.1	1.2
Qr40-80/150 kV	Z_{eff}	8.8	9.4	9.3	8.1	8.6	9.3
	$\rho_{eff}(g/cm^3)$	1.1	1.2	1.2	1.0	1.1	1.2
Br59-90/150 kV	Z_{eff}	8.7	9.3	9.7	8.0	8.4	9.1
	$\rho_{eff}(g/cm^3)$	1.1	1.2	1.2	1.0	1.1	1.2
Qr40-90/150 kV	Z_{eff}	8.7	9.3	9.7	8.1	8.4	9.2
	$\rho_{eff}(g/cm^3)$	1.1	1.2	1.2	1.0	1.1	1.2
SPECT/CT							
I41s-80/130 kV	Z_{eff}	9.1	10.0	10.7	8.2	8.9	9.7
	$\rho_{eff}(g/cm^3)$	1.1	1.2	1.3	1.0	1.1	1.2

*without transverse processes
Table modified from (*12*)

Appendix 3: Bone Volume Fraction – Calculation of Empirical Correction Factors

This section describes the determination of the correction factors (C and K) to estimate the effective density of the quantified material (this information is taken and modified from (*12*); image Br59-80/150 kV is used as an example).

To calculate material mass fractions, it was necessary to apply a double empirical correction factor (C and K) for obtaining the effective density and for resolving the equation system (equations 41, equation 34, and equation 35). Both corrections are dependent on the Z_{eff} value. Liu *et al*. (*22*) documented the use of one empirically determined correction factor (C) to calculate the effective density for materials with a Z_{eff} ≥10. In our case, both corrections were applied in the whole range of Z_{eff} values; this difference comes from the lack of specific information related to the detector response function. 200 mg/cm^3 of hydroxyapatite (HA), 800 mg/cm^3 of HA, and 1,250 mg/cm^3 of HA bone reference samples from the phantom CIRS model 062 were used to find both correction factors.

The measured effective density (ρ_{eff}) and effective atomic number (Z_{eff}) of bone samples of the CIRS model 062 phantom are listed in Table 10 (Appendix 2: Bone Volume Fraction – Additional Tables and Figures).

In a first step, the mass fraction method was applied to the 200 mg/cm^3 HA effective density $\rho_{eff} = 1.15 g/cm^3$, hydroxyapatite mass fraction ($MF_{HA} = 0.17$), 800 mg/cm^3 HA ($\rho_{eff} = 1.52 g/cm^3$, $MF_{HA} = 0.53$) and 1250 mg/cm^3 HA ($\rho_{eff} = 1.82 g/cm^3$, $MF_{HA} = 0.69$) samples from the phantom CIRS model 062, adjusting the value of $\rho_{eff}C$ in the equation system (equations 42, equation 34 and equation 35) that permits to obtain the right hydroxyapatite mass fraction (MF_{HA}) of each sample.

200 mg/cm^3 HA:

$$\rho_{eff,200}C_{200} = 0.65 g/cm^3$$

800 mg/cm^3 HA:

$$\rho_{eff,800}C_{800} = 0.72 g/cm^3$$

1250 mg/cm^3 HA:

$$\rho_{eff,1250}C_{1250} = 0.83 g/cm^3$$

Values of $C_{200}(Z_{eff} = 9.02)$, $C_{800}(Z_{eff} = 10.76)$ and $C_{1250}(Z_{eff} = 11.42)$ are obtained by the division for the effective density of each sample:

200 mg/cm^3 HA:

$$C(Z_{eff} = 9.02) = \frac{0.65g/cm^3}{\rho_{eff,200}} = \frac{0.65g/cm^3}{1.15g/cm^3} = 0.57$$

800 mg/cm^3 HA:

$$C(Z_{eff} = 10.76) = \frac{0.72g/cm^3}{\rho_{eff,800}} = \frac{0.72g/cm^3}{1.52g/cm^3} = 0.48$$

1250 mg/cm^3 HA:

$$C(Z_{eff} = 11.42) = \frac{0.83g/cm^3}{\rho_{eff,1250}} = \frac{0.83g/cm^3}{1.82g/cm^3} = 0.46$$

Parameter of a linear fit between 200 mg/cm^3 HA and 800 mg/cm^3 HA samples and between 800 mg/cm^3 HA and 1250 mg/cm^3 HA samples:

200 mg/cm^3 HA to 800 mg/cm^3 HA ($1 < Z_{eff} < 11$)

$$C = -0.05 \times Z_{eff} + 1.05 \qquad A3.1$$

800 mg/cm^3 HA to 1250 mg/cm^3 HA ($Z_{eff} \geq 11$)

$$C = -0.03 \times Z_{eff} + 0.76 \qquad A3.2$$

The mass fraction method requires the construction of a lookup table for the first 30 element of the periodic table to calculate the effective atomic number and the effective density. The effective density is calculated by the following equation:

$$\rho_{eff,lookup-table} = \frac{\mu_{eff,E_1}}{f_{E_1}(Z_{eff})} = \frac{\rho_{eff}}{C \times K} \qquad A3.3$$

Here, $f_{E_1}(Z_{eff}) = \int_{E=0\,keV}^{E=E_1} w_{E_1}(E)\mu_m(E, Z_{eff})dE$, and $\mu_m(E, Z_{eff})$ corresponds to the attenuation coefficient of elements with atomic number between 1 and 30. More details are provided by Liu *et al.* (*22*) and Heismann *et al.* (*94*).

From equation A3.3 is possible to obtain an expression for the effective density in the volume-of-interest:

$$\rho_{eff} = C \times K \times \rho_{eff,lookup-table} \qquad A3.4$$

Lastly, K can be calculated as:

$$K = \frac{C \times \rho_{eff,lookup-table}}{\rho_{eff}} \qquad A3.5$$

The values of $\rho_{eff,lookup\ table}$ from the lookup table and *K* from equation *A3.5* are:

200 mg/cm^3 HA:

$$\rho_{eff,lookup-table,200} = 1.30 g/cm^3$$

$$K(Z_{eff} = 9.02) = 1.55$$

800 mg/cm^3 HA:

$$\rho_{eff,lookup-table,800} = 1.72 g/cm^3$$

$$K(Z_{eff} = 10.76) = 1.86$$

1250 mg/cm^3 HA:

$$\rho_{eff,lookup-table,1250} = 2.01 g/cm^3$$

$$K(Z_{eff} = 11.42) = 1.97$$

Parameter of a linear fit between 200 mg/cm^3 HA and 800 mg/cm^3 HA samples and between 800 mg/cm^3 HA and 1250 mg/cm^3 HA samples:

200 mg/cm^3 HA - 800 mg/cm^3 HA

$$K = 0.18 \times Z_{eff} - 0.05\ for\ 1 < Z_{eff} < 11$$

800 mg/cm^3 HA - 1250 mg/cm^3 HA

$$K = 0.17 \times Z_{eff} + 0.01\ for\ 11 \leq Z_{eff}$$

Bibliography

1. International Commission on Radiological Protection. Basic anatomical and physiological data for use in radiological protection: the skeleton. A report of a Task Group of Committee 2 of the International Commission on Radiological Protection. *Ann ICRP.* 1995;25:1-80.

2. International Commission on Radiological Protection. Basic anatomical and physiological data for use in radiological protection: reference values. A report of age- and gender-related differences in the anatomical and physiological characteristics of reference individuals. ICRP Publication 89. *Ann ICRP.* 2002;32:5-265.

3. Glatting G, Bardies M, Lassmann M. Treatment planning in molecular radiotherapy. *Z Med Phys.* 2013;23:262-269.

4. Bolch WE, Eckerman KF, Sgouros G, Thomas SR. MIRD pamphlet No. 21: a generalized schema for radiopharmaceutical dosimetry--standardization of nomenclature. *J Nucl Med.* 2009;50:477-484.

5. Siantar CH, Vetter K, DeNardo GL, DeNardo SJ. Treatment planning for molecular targeted radionuclide therapy. *Cancer Biother Radiopharm.* 2002;17:267-280.

6. Hindorf C, Glatting G, Chiesa C, Linden O, Flux G. EANM Dosimetry Committee guidelines for bone marrow and whole-body dosimetry. *Eur J Nucl Med Mol Imaging.* 2010;37:1238-1250.

7. Lassmann M, Hänscheid H, Chiesa C, Hindorf C, Flux G, Luster M. EANM Dosimetry Committee series on standard operational procedures for pre-therapeutic dosimetry I: blood and bone marrow dosimetry in differentiated thyroid cancer therapy. *Eur J Nucl Med Mol Imaging.* 2008;35:1405-1412.

8. Salas-Ramirez M, Tran-Gia J, Kesenheimer C, et al. Quantification of fat fraction in lumbar vertebrae: correlation with age and implications for bone marrow dosimetry in molecular radiotherapy. *Phys Med Biol.* 2018;63:025029.

9. Thomsen JS, Jensen MV, Niklassen AS, Ebbesen EN, Bruel A. Age-related changes in vertebral and iliac crest 3D bone microstructure--differences and similarities. *Osteoporos Int.* 2015;26:219-228.

10. Cristy M. Active bone marrow distribution as a funtion of age in human. *Phys Med Biol.* 1981;26:389-400.

11. Bolch WE, Patton PW, Rajon DA, Shah AP, Jokisch DW, Inglis BA. Considerations of marrow cellularity in 3-dimensional dosimetric models of the trabecular skeleton. *J Nucl Med.* 2002;43:97-108.

12. Salas-Ramirez M, Tran-Gia J, Gbureck U, Kosmala A, Lassmann M. Quantification of the trabecular bone volume fraction for bone marrow dosimetry in molecular radiotherapy by using a dual-energy (SPECT/)CT. *Phys Med Biol.* 2019;64.

13. Bernard CP, Liney GP, Manton DJ, Turnbull LW, Langton CM. Comparison of fat quantification methods: a phantom study at 3.0T. *J Magn Reson Imaging.* 2008;27:192-197.

14. Bydder M, Yokoo T, Hamilton G, et al. Relaxation effects in the quantification of fat using gradient echo imaging. *Magn Reson Imaging.* 2008;26:347-359.

15. Berglund J, Ahlstrom H, Kullberg J. Model-based mapping of fat unsaturation and chain length by chemical shift imaging--phantom validation and in vivo feasibility. *Magn Reson Med.* 2012;68:1815-1827.

16. Wilderman SJ, Roberson PL, Bolch WE, Dewaraja YK. Investigation of effect of variations in bone fraction and red marrow cellularity on bone marrow dosimetry in radio-immunotherapy. *Phys Med Biol.* 2013;58:4717-4731.

17. Takasu M, Tamura T, Kaichi Y, et al. Magnetic resonance evaluation of multiple myeloma at 3.0 Tesla: how do bone marrow plasma cell percentage and selection of protocols affect lesion conspicuity? *PLoS One.* 2014;9:e85931.

18. Pichardo JC, Milner RJ, Bolch WE. MRI measurement of bone marrow cellularity for radiation dosimetry. *J Nucl Med.* 2011;52:1482-1489.

19. Geyer AM, Schwarz BC, Hobbs RF, Sgouros G, Bolch WE. Quantitative impact of changes in marrow cellularity, skeletal size, and bone mineral density on active marrow dosimetry based upon a reference model. *Med Phys.* 2017;44:272-283.

20. Goodsitt MM, Shenoy A, Shen J, et al. Evaluation of dual energy quantitative CT for determining the spatial distributions of red marrow and bone for dosimetry in internal emitter radiation therapy. *Med Phys.* 2014;41:051901.

21. Goodsitt MM, Johnson RH, Chesnut CH, 3rd. A new set of calibration standards for estimating the fat and mineral content of vertebrae via dual energy QCT. *Bone Miner.* 1991;13:217-233.

22. Liu X, Yu L, Primak AN, McCollough CH. Quantitative imaging of element composition and mass fraction using dual-energy CT: three-material decomposition. *Med Phys.* 2009;36:1602-1609.

23. Clarke B. Normal bone anatomy and physiology. *Clin J Am Soc Nephrol.* 2008;3 Suppl 3:S131-139.

24. Goodsitt MM, Kilcoyne RF, Gutcheck RA, Richardson ML, Rosenthal DI. Effect of collagen on bone mineral analysis with CT. *Radiology.* 1988;167:787-791.

25. *Therapeutic Applications of Monte Carlo Calculations in Nuclear Medicine*. London, UK: Institute of Physics Publishing; 2003.

26. Travlos GS. Normal structure, function, and histology of the bone marrow. *Toxicol Pathol.* 2006;34:548-565.

27. Rozman C, Feliu E, Berga L, Reverter JC, Climent C, Ferran MJ. Age-related variations of fat tissue fraction in normal human bone marrow depend both on size and number of adipocytes: a stereological study. *Exp Hematol.* 1989;17:34-37.

28. Brandi ML. Microarchitecture, the key to bone quality. *Rheumatology.* 2009;48:iv3-iv8.

29. Walsh JS. Normal bone physiology, remodelling and its hormonal regulation. *Surgery (Oxford).* 2015;33:1-6.

30. Chen H, Zhou X, Shoumura S, Emura S, Bunai Y. Age- and gender-dependent changes in three-dimensional microstructure of cortical and trabecular bone at the human femoral neck. *Osteoporos Int.* 2010;21:627-636.

31. Chen H, Shoumura S, Emura S, Bunai Y. Regional variations of vertebral trabecular bone microstructure with age and gender. *Osteoporos Int.* 2008;19:1473-1483.

32. Gong JK, Arnold JS, Cohn SH. Composition of trabecular and cortical bone. *Anat Rec.* 1964;149:325-331.

33. Oftadeh R, Perez-Viloria M, Villa-Camacho JC, Vaziri A, Nazarian A. Biomechanics and mechanobiology of trabecular bone: a review. *J Biomech Eng.* 2015;137.

34. International Commission on Radiation Units and Measurements. Report 44: Tissue substitutes in radiation dosimetry and measurement. *J ICRU.* 1989:vii, 189 p.

35. Shah AP, Bolch WE, Rajon DA, Patton PW, Jokisch DW. A paired-image radiation transport model for skeletal dosimetry. *J Nucl Med.* 2005;46:344-353.

36. Watchman CJ, Jokisch DW, Patton PW, Rajon DA, Sgouros G, Bolch WE. Absorbed fractions for alpha-particles in tissues of trabecular bone: Considerations of marrow cellularity within the ICRP reference male. *Journal of Nuclear Medicine.* 2005;46:1171-1185.

37. Chappard D, Basle MF, Legrand E, Audran M. Trabecular bone microarchitecture: a review. *Morphologie.* 2008;92:162-170.

38. Malempati S, Joshi S, Lai S, Braner DA, Tegtmeyer K. Videos in clinical medicine. Bone marrow aspiration and biopsy. *N Engl J Med.* 2009;361:e28.

39. Moulopoulos LA, Dimopoulos MA. Magnetic resonance imaging of the bone marrow in hematologic malignancies. *Blood.* 1997;90:2127-2147.

40. Nobauer I, Uffmann M. Differential diagnosis of focal and diffuse neoplastic diseases of bone marrow in MRI. *Eur J Radiol.* 2005;55:2-32.

41. Ruschke S, Diefenbach M, Franz D, Baum T, Karampinos DC. Molecular In Vivo Imaging of Bone Marrow Adipose Tissue. *Current Molecular Biology Reports.* 2018;4:25-33.

42. Ballon D, Jakubowski AA, Graham MC, Schneider E, Koutcher JA. Spatial mapping of the percentage cellularity in human bone marrow using magnetic resonance imaging. *Med Phys.* 1996;23:243-250.

43. Mills AF, Sakai O, Anderson SW, Jara H. Principles of quantitative MR imaging with illustrated review of applicable modular pulse diagrams. *Radiographics.* 2017;37:2083-2105.

44. Grover VP, Tognarelli JM, Crossey MM, Cox IJ, Taylor-Robinson SD, McPhail MJ. Magnetic resonance imaging: Principles and techniques: Lessons for Clinicians. *J Clin Exp Hepatol.* 2015;5:246-255.

45. Bushberg JT, Seibert JA, Leidholdt EM, Boone JM. *The essential physics of medical imaging*: Wolters Kluwer Health; 2011.

46. Qayyum A. MR spectroscopy of the liver: principles and clinical applications. *Radiographics.* 2009;29:1653-1664.

47. Stanisz GJ, Odrobina EE, Pun J, et al. T1, T2 relaxation and magnetization transfer in tissue at 3T. *Magn Reson Med.* 2005;54:507-512.

48. Krebs HA. Chemical composition of blood plasma and serum. *Annu Rev Biochem.* 1950;19:409-430.

49. Trefts E, Gannon M, Wasserman DH. The liver. *Curr Biol.* 2017;27:R1147-R1151.

50. Tognarelli JM, Dawood M, Shariff MI, et al. Magnetic resonance spectroscopy: Principles and techniques: Lessons for clinicians. *J Clin Exp Hepatol.* 2015;5:320-328.

51. van der Graaf M. In vivo magnetic resonance spectroscopy: basic methodology and clinical applications. *Eur Biophys J.* 2010;39:527-540.

52. Harris RK, Becker ED, Cabral de Menezes SM, Goodfellow R, Granger P. NMR nomenclature: Nuclear spin properties and conventions for chemical shifts. IUPAC recommendations 2001. *Solid State Nucl Magn Reson.* 2002;22:458-483.

53. Hamilton G, Yokoo T, Bydder M, et al. In vivo characterization of the liver fat (1)H MR spectrum. *NMR Biomed.* 2011;24:784-790.

54. ACR. Glossary of MRI Terms 5th edition:https://www.acr.org/-/media/ACR/Files/Radiology-Safety/MR-Safety/MRGlossary.pdf?la=en. Accessed 21.05.2019.

55. Faghihi R, Zeinali-Rafsanjani B, Mosleh-Shirazi MA, et al. Magnetic resonance spectroscopy and its clinical applications: A review. *J Med Imaging Radiat Sci.* 2017;48:233-253.

56. Ballon D, Jakubowski A, Gabrilove J, et al. In vivo measurements of bone marrow cellularity using volume-localized proton NMR spectroscopy. *Magn Reson Med.* 1991;19:85-95.

57. Schick F, Bongers H, Jung W-I, Skalej M, Lutz O, Claussen CD. Volume-selective proton MRS in vertebral bodies. *Magn Reson Med.* 1992;26:207-217.

58. Pansini VM, Monnet A, Salleron J, Penel G, Migaud H, Cotten A. Reproducibility of 1H MR spectroscopy of hip bone marrow at 3 Tesla. *J Magn Reson Imaging.* 2012;36:1445-1449.

59. Pansini V, Monnet A, Salleron J, Hardouin P, Cortet B, Cotten A. 3 Tesla (1) H MR spectroscopy of hip bone marrow in a healthy population, assessment of normal fat content values and influence of age and sex. *J Magn Reson Imaging.* 2014;39:369-376.

60. Li X, Kuo D, Schafer AL, et al. Quantification of vertebral bone marrow fat content using 3 Tesla MR spectroscopy: reproducibility, vertebral variation, and applications in osteoporosis. *J Magn Reson Imaging.* 2011;33:974-979.

61. Schellinger D, Lin CS, Hatipoglu HG, Fertikh D. Potential value of vertebral proton MR spectroscopy in determining bone weakness. *AJNR Am J Neuroradiol.* 2001;22:1620-1627.

62. Ren J, Dimitrov I, Sherry AD, Malloy CR. Composition of adipose tissue and marrow fat in humans by 1H NMR at 7 Tesla. *J Lipid Res.* 2008;49:2055-2062.

63. Bottomley PA, Griffiths JR. *Handbook of magnetic resonance spectroscopy in vivo: MRS theory, practice and applications*. New York, UNITED KINGDOM: John Wiley & Sons, Incorporated; 2016.

64. Del Grande F, Santini F, Herzka DA, et al. Fat-suppression techniques for 3-T MR imaging of the musculoskeletal system. *Radiographics.* 2014;34:217-233.

65. Dixon WT. Simple proton spectroscopic imaging. *Radiology.* 1984;153:189-194.

66. Grimm A, Meyer H, Nickel MD, et al. Evaluation of 2-point, 3-point, and 6-point Dixon magnetic resonance imaging with flexible echo timing for muscle fat quantification. *Eur J Radiol.* 2018;103:57-64.

67. Ma J. Dixon techniques for water and fat imaging. *J Magn Reson Imaging.* 2008;28:543-558.

68. Michaely HJ, Morelli JN, Budjan J, et al. CAIPIRINHA-Dixon-TWIST (CDT)-volume-interpolated breath-hold examination (VIBE): a new technique for fast time-resolved dynamic 3-dimensional imaging of the abdomen with high spatial resolution. *Invest Radiol.* 2013;48:590-597.

69. Kim YS, Mun CW, Cho ZH. Chemical-shift imaging with large magnetic field inhomogeneity. *Magn Reson Med.* 1987;4:452-460.

70. Lodes CC, Felmlee JP, Ehman RL, et al. Proton MR chemical shift imaging using double and triple phase contrast acquisition methods. *J Comput Assist Tomogr.* 1989;13:855-861.

71. Glover GH, Schneider E. Three-point Dixon technique for true water/fat decomposition with B0 inhomogeneity correction. *Magn Reson Med.* 1991;18:371-383.

72. Glover GH. Multipoint Dixon technique for water and fat proton and susceptibility imaging. *J Magn Reson Imaging.* 1991;1:521-530.

73. Le Ster C, Gambarota G, Lasbleiz J, Guillin R, Decaux O, Saint-Jalmes H. Breath-hold MR measurements of fat fraction, T1 , and T2 * of water and fat in vertebral bone marrow. *J Magn Reson Imaging.* 2016;44:549-555.

74. Kijowski R, Woods MA, Lee KS, et al. Improved fat suppression using multipeak reconstruction for IDEAL chemical shift fat-water separation: application with fast spin echo imaging. *J Magn Reson Imaging.* 2009;29:436-442.

75. Reeder SB, Robson PM, Yu H, et al. Quantification of hepatic steatosis with MRI: the effects of accurate fat spectral modeling. *J Magn Reson Imaging.* 2009;29:1332-1339.

76. Reeder SB, Pineda AR, Wen Z, et al. Iterative decomposition of water and fat with echo asymmetry and least-squares estimation (IDEAL): Application with fast spin-echo imaging. *Magn Reson Med.* 2005;54:636-644.

77. Reeder SB, Cruite I, Hamilton G, Sirlin CB. Quantitative assessment of liver fat with magnetic resonance imaging and spectroscopy. *J Magn Reson Imaging.* 2011;34:729-749.

78. Satkunasingham J, Besa C, Bane O, et al. Liver fat quantification: Comparison of dual-echo and triple-echo chemical shift MRI to MR spectroscopy. *Eur J Radiol.* 2015;84:1452-1458.

79. Ballon D, Jakubowski AA, Tulipano PK, et al. Quantitative assessment of bone marrow hematopoiesis using parametric magnetic resonance imaging. *Magn Reson Med.* 1998;39:789-800.

80. Reeder SB, Sirlin CB. Quantification of liver fat with magnetic resonance imaging. *Magn Reson Imaging Clin N Am.* 2010;18:337-357, ix.

81. Longo R, Pollesello P, Ricci C, et al. Proton MR spectroscopy in quantitative in vivo determination of fat content in human liver steatosis. *J Magn Reson Imaging.* 1995;5:281-285.

82. Thomsen C, Becker U, Winkler K, Christoffersen P, Jensen M, Henriksen O. Quantification of liver fat using magnetic resonance spectroscopy. *Magn Reson Imaging.* 1994;12:487-495.

83. Szczepaniak LS, Babcock EE, Schick F, et al. Measurement of intracellular triglyceride stores by H spectroscopy: validation in vivo. *Am J Physiol.* 1999;276:E977-989.

84. Li G, Xu Z, Gu H, et al. Comparison of chemical shift-encoded water-fat MRI and MR spectroscopy in quantification of marrow fat in postmenopausal females. *J Magn Reson Imaging.* 2017;45:66-73.

85. Baum T, Yap SP, Dieckmeyer M, et al. Assessment of whole spine vertebral bone marrow fat using chemical shift-encoding based water-fat MRI. *J Magn Reson Imaging.* 2015;42:1018-1023.

86. Karampinos DC, Ruschke S, Dieckmeyer M, et al. Modeling of T2* decay in vertebral bone marrow fat quantification. *NMR Biomed.* 2015;28:1535-1542.

87. Ginat DT, Gupta R. Advances in computed tomography imaging technology. *Annu Rev Biomed Eng.* 2014;16:431-453.

88. McCollough CH, Leng S, Yu L, Fletcher JG. Dual- and multi-energy CT: Principles, technical approaches, and clinical applications. *Radiology.* 2015;276:637-653.

89. van Hamersvelt RW, Schilham AMR, Engelke K, et al. Accuracy of bone mineral density quantification using dual-layer spectral detector CT: a phantom study. *Eur Radiol.* 2017;27:4351-4359.

90. Mahesh M. Search for isotropic resolution in CT from conventional through multiple-row detector. *Radiographics.* 2002;22:949-962.

91. International Commission on Radiation Units and Measurements. Report 87: Radiation dose and image-quality assessment in computed tomography. *J ICRU.* 2012;12:1-149.

92. Raman SP, Mahesh M, Blasko RV, Fishman EK. CT scan parameters and radiation dose: practical advice for radiologists. *J Am Coll Radiol.* 2013;10:840-846.

93. Marin D, Boll DT, Mileto A, Nelson RC. State of the art: dual-energy CT of the abdomen. *Radiology.* 2014;271:327-342.

94. Heismann BJ, Leppert J, Stierstorfer K. Density and atomic number measurements with spectral x-ray attenuation method. *Journal of Applied Physics.* 2003;94:2073-2079.

95. Attix FH. *Introduction to Radiological Physics and Radiation Dosimetry*. Germany: Wiley-VCH; 2004.

96. Alvarez RE, Macovski A. Energy-selective reconstructions in x-ray computerized tomography. *Phys Med Biol.* 1976;21:733-744.

97. Lehmann LA, Alvarez RE, Macovski A, et al. Generalized image combinations in dual KVP digital radiography. *Med Phys.* 1981;8:659-667.

98. Kalender WA, Perman WH, Vetter JR, Klotz E. Evaluation of a prototype dual-energy computed tomographic apparatus. I. Phantom studies. *Med Phys.* 1986;13:334-339.

99. International Commission on Radiation Units and Measurements. Report 85: Fundamental quantities and units for ionizing radiation. *J ICRU.* 2011;11:1-31.

100. Shah AP, Patton PW, Rajon DA, Bolch WE. Adipocyte spatial distributions in bone marrow: implications for skeletal dosimetry models. *J Nucl Med.* 2003;44:774-783.

101. Beddoe AH, Darley PJ, Spiers FW. Measurements of trabecular bone structure in man. *Phys Med Biol.* 1976;21:589-607.

102. Whitwell JR, Spiers FW. Calculated beta-ray dose factors for trabecular bone. *Phys Med Biol.* 1976;21:16-38.

103. Spiers FW, Beddoe AH. 'Radial' scanning of trabecular bone: consideration of the probability distributions of path lengths through cavities and trabeculae. *Phys Med Biol.* 1977;22:670-680.

104. Beddoe AH. Measurements of the microscopic structure of cortical bone. *Phys Med Biol.* 1977;22:298-308.

105. Spiers FW, Whitwell JR, Beddoe AH. Calculated dose factors for the radiosensitive tissues in bone irradiated by surface-deposited radionuclides. *Phys Med Biol.* 1978;23:481-494.

106. Geant4 AST. Physics Reference Manual. *Release 10.5* [http://geant4-userdoc.web.cern.ch/geant4-userdoc/UsersGuides/PhysicsReferenceManual/fo/PhysicsReferenceManual.pdf. Accessed 08/07/2019, 2019.

107. Ljungberg M, Strand SE, King MA. *Monte carlo calculations in nuclear medicine: Applications in diagnostic imaging*: Taylor & Francis; 1998.

108. Zankl M, Becker J, Lee C, Bolch WE, Yeom YS, Kim CH. Computational phantoms, ICRP/ICRU, and further developments. *Annals of the ICRP.* 2018;47:35-44.

109. Segars WP, Sturgeon G, Mendonca S, Grimes J, Tsui BM. 4D XCAT phantom for multimodality imaging research. *Med Phys.* 2010;37:4902-4915.

110. O'Reilly SE, DeWeese LS, Maynard MR, et al. An image-based skeletal dosimetry model for the ICRP reference adult female-internal electron sources. *Phys Med Biol.* 2016;61:8794-8824.

111. Hough M, Johnson P, Rajon D, Jokisch D, Lee C, Bolch W. An image-based skeletal dosimetry model for the ICRP reference adult male--internal electron sources. *Phys Med Biol.* 2011;56:2309-2346.

112. Rajon DA, Shah AP, Watchman CJ, Brindle JM, Bolch WE. A hyperboliod representation of the bone-marrow interface within 3D NMR images of trabecular bone: applications to skeletal dosimetry. *Phys Med Biol.* 2003;48:1721-1740.

113. Harrison RL. Introduction to monte carlo simulation. *AIP Conf Proc.* 2010;1204:17-21.

114. Snyder WS, Ford MR, Warner GG, Watson SB. MIRD pamphlet No. 11: "S", absorbed dose per unit cumulated activity for selected radionuclides and organs. In: Medicine SoN, ed. New York; 1975.

115. International Commission on Radiological Protection. Limits for Intakes of Radionuclides by Workers, Part 1. *Ann ICRP.* 1979;2:i-iv.

116. Eckerman KF. Aspects of the dosimetry of radionuclides within the skeleton with particular emphasis on the active marrow. *Radiopharmaceutical dosimetry symposium, Oak Ridge, TN, USA, 5 Nov 1985*. United States; 1985.

117. Eckerman KF, Stabin MG. Electron absorbed fractions and dose conversion factors for marrow and bone by skeletal regions. *Health Phys.* 2000;78:199-214.

118. Bouchet LG, Jokisch DW, Bolch WE. A three-dimensional transport model for determining absorbed fractions of energy for electrons within trabecular bone. *J Nucl Med.* 1999;40:1947-1966.

119. Bouchet LG, Bolch WE. A three-dimensional transport model for determining absorbed fractions of energy for electrons within cortical bone. *J Nucl Med.* 1999;40:2115-2124.

120. Jokisch DW, Patton PW, Inglis BA, et al. NMR microscopy of trabecular bone and its role in skeletal dosimetry. *Health Phys.* 1998;75:584-596.

121. Jokisch DW, Bouchet LG, Patton PW, Rajon DA, Bolch WE. Beta-particle dosimetry of the trabecular skeleton using Monte Carlo transport within 3D digital images. *Med Phys.* 2001;28:1505-1518.

122. Menzel HG, Clement C, DeLuca P. ICRP Publication 110. Realistic reference phantoms: an ICRP/ICRU joint effort. A report of adult reference computational phantoms. *Ann ICRP.* 2009;39:1-164.

123. Patton PW, Rajon DA, Shah AP, Jokisch DW, Inglis BA, Bolch WE. Site-specific variability in trabecular bone dosimetry: considerations of energy loss to cortical bone. *Med Phys.* 2002;29:6-14.

124. Patton PW, Jokisch DW, Rajon DA, et al. Skeletal dosimetry via NMR microscopy: investigations of sample reproducibility and signal source. *Health Phys.* 2002;82:316-326.

125. Rajon DA, Bolch WE. Marching cube algorithm: review and trilinear interpolation adaptation for image-based dosimetric models. *Computerized Medical Imaging and Graphics.* 2003;27:411-435.

126. Rajon DA, Pichardo JC, Brindle JM, et al. Image segmentation of trabecular spongiosa by visual inspection of the gradient magnitude. *Phys Med Biol.* 2006;51:4447-4467.

127. Pichardo JC, Trindade AA, Brindle JM, Bolch WE. Method for estimating skeletal spongiosa volume and active marrow mass in the adult male and adult female. *J Nucl Med.* 2007;48:1880-1888.

128. Lee C, Lodwick D, Hurtado J, Pafundi D, Williams JL, Bolch WE. The UF family of reference hybrid phantoms for computational radiation dosimetry. *Phys Med Biol.* 2010;55:339-363.

129. Shah A. *Reference skeletal dosimetry model for an adult male radionuclide therapy patient based on 3D imaging and paired-image radiation transport* [Doctoral Thesis]. Gainesville, FL, USA: Department of Biomedical Engineering, University of Florida; 2004.

130. Pafundi D, Rajon D, Jokisch D, Lee C, Bolch W. An image-based skeletal dosimetry model for the ICRP reference newborn--internal electron sources. *Phys Med Biol.* 2010;55:1785-1814.

131. Kawrakow I, Mainegra-Hing E, Rogers DWO, Tessier F, Walters BRB. *NRCC Report PIRS-701: The EGSnrc Code System: Monte Carlo Simulation of Electron and Photon Transport.* Ottawa, Canada: National Research Council Canada; 2000.

132. Werner CJ, Bull JS, Solomon CJ, et al. *MCNP6.2 Release Notes.* New Mexico: Los Alamos National Laboratory; 2018.

133. Hurtado JL, Lee C, Lodwick D, Goede T, Williams JL, Bolch WE. Hybrid computational phantoms representing the reference adult male and adult female: construction and applications for retrospective dosimetry. *Health Phys.* 2012;102:292-304.

134. Schindelin J, Arganda-Carreras I, Frise E, et al. Fiji: an open-source platform for biological-image analysis. *Nat Methods.* 2012;9:676-682.

135. Schneider CA, Rasband WS, Eliceiri KW. NIH Image to ImageJ: 25 years of image analysis. *Nat Methods.* 2012;9:671-675.

136. Naressia A, Couturierb C, Castangb I, de Beerb R, Graveron-Demillyc D. Java-based graphical user interface for MRUI, a software package for quantitation of in vivo/medical magnetic resonance spectroscopy signals. *Computers in Biology and Medicine.* 2001;31:269-286.

137. Stefan D, Di Cesare F, Andrasescu A, et al. Quantitation of magnetic resonance spectroscopy signals: the jMRUI software package. *Measurement Science and Technology.* 2009;20.

138. *R: A language and environment for statistical computing* [computer program]. Version 3.3.2 and 3.6.1. Vienna, Austria; 2008.

139. Hines CD, Yu H, Shimakawa A, McKenzie CA, Brittain JH, Reeder SB. T1 independent, T2* corrected MRI with accurate spectral modeling for quantification of fat: validation in a fat-water-SPIO phantom. *J Magn Reson Imaging.* 2009;30:1215-1222.

140. Yu H, Shimakawa A, McKenzie CA, Brodsky E, Brittain JH, Reeder SB. Multiecho water-fat separation and simultaneous R2* estimation with multifrequency fat spectrum modeling. *Magn Reson Med.* 2008;60:1122-1134.

141. Fedorov A, Beichel R, Kalpathy-Cramer J, et al. 3D Slicer as an image computing platform for the quantitative imaging network. *Magn Reson Imaging.* 2012;30:1323-1341.

142. Kikinis R, Pieper SD, Vosburgh KG. 3D Slicer: A Platform for Subject-Specific Image Analysis, Visualization, and Clinical Support. In: Jolesz F. (eds) Intraoperative Imaging and Image-Guided Therapy. In: Springer, ed; 2014.

143. Kalender WA. A phantom for standarization and quality control in spinal bone mineral measurements by QCT and DXA: Design considerations and specifications. *Med Phys.* 1992;19:583-586.

144. Siemens. Simulation of x-ray spectra. Online tool for the simulation of x-ray spectra. https://www.oem-xray-components.siemens.com/x-ray-spectra-simulation. Accessed 12.12.2018.

145. *XMuDat: Photon attenuation data on PC* [computer program]. Version 1.0.1. Vienna: Institut f. Biomed. Technik und Physik; 1998.

146. Azevedo SG, Martz HE, Aufderheide MB, et al. System-independent characterization of materials using dual-energy computed tomography. *Ieee Transactions on Nuclear Science.* 2016;63:341-350.

147. Christel T, Kuhlmann M, Vorndran E, Groll J, Gbureck U. Dual setting alpha-tricalcium phosphate cements. *J Mater Sci Mater Med.* 2013;24:573-581.

148. Quelch KJ, Melick RA, Bingham PJ, Mercuri SM. Chemical composition of human bone. *Arch Oral Biol.* 1983;28:665-674.

149. Woodard HQ, White DR. Bone models for use in radiotherapy dosimetry. *The British Journal of Radiology.* 1982;55:277-282.

150. Salas-Ramirez M, Tran-Gia J, Gbureck U, Kosmala A, Lassmann M. Corrigendum: Quantification of the trabecular bone volume fraction for bone marrow dosimetry in molecular radiotherapy by using a dual-energy (SPECT/)CT (2019 Phys. Med. Biol. 64 205014). *Phys Med Biol.* 2020;65:029501.

151. Majumdar S. Magnetic resonance imaging of trabecular bone structure. *Top Magn Reson Imaging.* 2002;13:323-334.

152. Schellinger D, Lin CS, Fertikh D, et al. Normal lumbar vertebrae: anatomic, age, and sex variance in subjects at proton mr spectroscopy-initial experience. *Radiology.* 2000;215:910-916.

153. Chen WT, Shih TT. Correlation between the bone marrow blood perfusion and lipid water content on the lumbar spine in female subjects. *J Magn Reson Imaging.* 2006;24:176-181.

154. Hartsock RJ, Smith EB, Petty CS. Normal variations with aging of the amount of hematopoietic tissue in bone marrow from the anterior iliac crest. A study made from 177 cases of sudden death examined by necropsy. *Am J Clin Pathol.* 1965;43:326-331.

155. Custer RP, Hayhoe FGJ. *An atlas of the blood and bone marrow*. Philadelphia: Saunders; 1974.

156. Ishijima H, Ishizaka H, Horikoshi H, Sakurai M. Water Fraction of Lumbar Vertebral Bone Marrow Estimated from Chemical Shift Misregistration on MR Imaging. *Am J Roentgenol.* 1996:355-358.

157. Lipton A, Uzzo R, Amato RJ, et al. The science and practice of bone health in oncology: managing bone loss and metastasis in patients with solid tumors. *J Natl Compr Canc Netw.* 2009;7 Suppl 7:S1-29; quiz S30.

158. Ulzheimer S, Freund J. The Stellar Detector. *White Paper, Siemens*.

Eidesstattliche Erklärung /Affidavit

Eidesstattliche Erklärung

Hiermit erkläre ich an Eides statt, die Dissertation *Methoden zur Verbesserung der Knochenmarkdosimetrie in der molekularen Strahlentherapie* eigenständig, d.h. insbesondere selbstständig und ohne Hilfe eines kommerziellen Promotionsberaters, angefertigt und keine anderen als die von mir angegebenen Quellen und Hilfsmittel verwendet zu haben.

Ich erkläre außerdem, dass die Dissertation weder in gleicher noch in ähnlicher Form bereits in einem anderen Prüfungsverfahren vorgelegen hat.

Würzburg, 01. März 2020 _____

Maikol Salas Ramírez

Affidavit

I hereby confirm that my thesis entitled *Methods to Improve Bone Marrow Dosimetry in Molecular Radiotherapy* is the result of my own work. I did not receive any help or support from commercial consultants. All sources and / or materials applied are listed and specified in the thesis.

Furthermore, I confirm that this thesis has not yet been submitted as part of another examination process neither in identical nor in similar form.

Würzburg, 01. March 2020 _____

Maikol Salas Ramírez

Curriculum Vitae

Personal Information

Place of Birth	Quesada, Alajuela, Costa Rica
Nationality	Costa Rican
Place of Residence	Würzburg, Germany

Education

10/2015 - Present	Graduate School of Life Sciences University of Würzburg, Germany *Degree:* Dr. rer. nat. *Estimated Completion*: 07/2020
09/2007 – 08/2009	University of Valencia, Spain *Degree:* Master in Medical Physics
03/2002 – 12/2006	University of Costa Rica, Costa Rica *Degree:* Bachelor in Physics

Professional Experience

10/2015 – Present	Department of Nuclear Medicine University Hospital of Würzburg, Germany *Position:* Doctoral Researcher
09/2009 – 09/2015	Department of Nuclear Medicine Hospital Mexico, Costa Rica *Position:* Medical Physicist
2010 – 2015	Department of Physics University of Costa Rica, Costa Rica *Position:* interim teacher

Languages

Mother Tongue:	Spanish				
Other language(s):	Understanding		Speaking		Writing
	Listening	Reading	Spoken interaction	Spoken production	
English	C1	C1	C1	C1	C1
German	DSH-2	DSH-2	DSH-2	DSH-2	DSH-2

DSH: Deutsche Sprachprüfung für den Hochschulzugang

Publications

Original Research (Publications)

J. Tran-Gia, M. Salas-Ramirez, M. Lassmann. What You See Is Not What You Get - On the Accuracy of Voxel-Based Dosimetry in Molecular Radiotherapy [published online ahead of print December 20, 2019]. J Nucl Med. DOI: 10.2967/jnumed.119.231480

M. Salas-Ramirez, J. Tran-Gia, U. Gbureck, A. Kosmala, M. Lassmann. Quantification of the trabecular bone volume fraction for bone marrow dosimetry in molecular radiotherapy by using a dual-energy (SPECT/)CT. Phys. Med. Biol. 64 (2019) 205014 (15pp). DOI: https://doi.org/10.1088/1361-6560/ab4476

M. Salas-Ramirez, J. Tran-Gia, C. Kesenheimer, A. M. Weng, A. Kosmala, A. Heidemeier, H. Köstler, M. Lassmann. Quantification of fat fraction in lumbar vertebrae: correlation with age and implications for bone marrow dosimetry in molecular radiotherapy. Phys. Med. Biol. 63 (2018) 025029 (10pp). DOI: https://doi.org/10.1088/1361-6560/aa9a28

Conference Contributions

European Association of Nuclear Medicine (EANM), Barcelona, 2019:
M. Salas Ramírez, J. Tran-Gia, U. Gbureck, A. Kosmala, M. Lassmann. Quantification of the Trabecular Bone Volume Fraction with Dual Energy Quantitative CT to Calculate Patient-Specific Radionuclide S Values for Bone Marrow Dosimetry. Eur J Nucl Med Mol Imaging (2019) 46 (Suppl 1): S1–S952

57. Jahrestagung der Deutschen Gesellschaft für Nuklearmedizin, Bremen, 2019:
M. Salas-Ramirez, B. van Rietbergen, M. Chauvin, M. Lassmann. Radiation Transport Model for Bone Marrow Dosimetry using GATE.

Third Geant4 International User Conference, Bordeaux, 2018:
M. Salas-Ramirez, B. van Rietbergen, M. Chauvin, M. Lassmann. Radiation Transport Model for Bone Marrow Dosimetry based on Tessellated Volumes using GATE.

European Association of Nuclear Medicine (EANM), Düsseldorf, 2018:
M. Salas-Ramirez, B. van Rietberg, M. Lassmann. Prototype for a Mesh-based Radiation Transport Model for Bone Marrow Dosimetry using GATE. Eur J Nucl Med Mol Imaging (2018) 45 (Suppl 1): S181.

European Association of Nuclear Medicine (EANM), Vienna, 2017
M. Salas-Ramirez, J. Tran-Gia, A. M. Weng, H. Köstler, M. Lassmann. The Influence of Age and Gender on Bone Marrow Fat Fraction. Eur. J. Nucl. Med. Mol. Imaging (2017) 44 (Suppl 2):S290. EANM

European Association of Nuclear Medicine (EANM), Vienna, 2017:
M. Salas-Ramirez, J. Tran-Gia, C. Kesenheimer, A. M. Weng, H. Köstler, M. Lassmann. Quantification of the Fat Fraction in Bone Marrow using Fat-Water Magnetic Resonance Imaging. Eur. J. Nucl. Med. Mol. Imaging (2017) 44 (Suppl 2):S805. DOI: https://doi.org/10.1007/s00259-017-3822-1

European Association of Nuclear Medicine (EANM), Barcelona, 2016:

M. Salas-Ramirez, S. Schlögl, J. Tran-Gia, C. Kesenheimer, H. Hänscheid, M. Lassmann. Simulation of radioactive sources in a bone cavity to evaluated the activity quantification in bone marrow dosimetry. Eur J Nucl Med Mol Imaging (2016) 43 (Suppl 1):S412.

European Association of Nuclear Medicine (EANM), Hamburg, 2015:

M. Salas-Ramirez, E. Mora-Ramirez, Theoretical model for release of patients with benign thyroid disease based on parameters obtained from EANM Standard Operational Procedures for Pre-Therapeutic Dosimetry II. EANM congress, Hamburg – 2015.

Acknowledgments

I am deeply grateful to the Deutscher Akademischer Austauschdienst (DAAD) and the Department of Nuclear Medicine of the University Hospital of Würzburg, for allowing me to develop this project in an open and creative environment. I would also like to thank the Graduate School of Life Sciences (GSLS) for providing the ideal framework for carrying out doctoral studies.

I want to express my deepest grateful to my PhD-tutor, Prof. Dr. Michael Laßmann, for believing in me and for allowing me to be part of his research team. I want to thank him for the provided help and guidance, from the preparation of the DAAD project draft, through my adaptation to a new workplace and culture, to the completion of this doctoral thesis.

I extend my sincere thanks to Prof. Dr. Andreas Buck, director of the Department of Nuclear Medicine of the University Hospital of Würzburg, for allowing me to be part of the work and research group of this medical center, for believing in the importance of the research conducted by medical physicists, as well as for the time and orientation as part of my doctoral committee.

I am also very grateful to Prof. Dr. Gerhard Glatting at the University Hospital of Ulm, for being part of my doctoral committee, for the provided guidance and time in each of the doctoral committee meetings, and especially for believing in the ideas that were developed within this doctoral project.

I want to sincerely thank Dr. Johannes Tran-Gia, who helped me in all the stages of this doctoral project, from the preparation of the carried out experiments to the development of the publications and this document. I also want to thank his advice and patience with all the questions related to life in Germany.

I give special thanks to Dr. Seval Beykan, who was my office mate during all this time, for the small talks that always helped to cope with the tedium of the days when things did not go well or the joys of the days when a good working day was achieved. This, as well, applies to Dr. Tran-Gia.

I am very grateful to my colleague Dr. Jessica Soares Machado (Jess), who was always my connection with Latin America. I also want to sincerely thank my colleagues, Dr. Uta Eberlein and Sarah Schumann, for all the provided help, from day-to-day topics related to life in Germany to the more detailed corrections of my presentations at conferences. I want to thank Dr. Eberlein for helping me in the revision of this document.

I want to extend my sincere thanks to my colleagues in the medical physics group, Susanne Schlögl, Andreas Hinsch, Dr. Heribert Hänscheid, Harald Schlotter and Tobias May, for the help provided in the elaboration of the experiments carried out in this project.

I want to thank the co-authors of the two publications achieved within this project: Dr. Tran-Gia, Dr. Kesenheimer, Dr. Weng, Dr. Kosmala, Dr. Heidemeier, Prof. Dr. Köstler, Prof. Dr. Gbureck, and Prof. Dr. Lassmann. Without your help, I could not achieve this point.

I want to thank immensely my parents Ana Isabel Ramírez Solis and Carlos Manuel Salas González, for letting me be who I am. Above all, always believing in me and reminding me that the traveled road was sufficient and that the rest I should enjoy. A profound thanks to my sister Yanna Salas Ramírez for helping me to keep alive the utopias that make us move. To Carlos Salas Ramírez and Jasson Salas Ramírez, my two brothers and old friends, and Yanna again, a big thank you for all the great trips, which finally made me get here.

Finally, I want to thank Gabriela Lobo Calderon, my companion for 15 years, with all my heart, for all the support, patience, and understanding throughout these years in Germany. For always having the right word and for reminding me that this is not everything. Gaby, I am deeply grateful to you for having made this trip with me and for making it also your journey.